VILNIUS UNIVERSITY

CENTER FOR PHYSICAL SCIENCES AND TECHNOLOGY

Domantas Peckus

ULTRAFAST EXCITON AND CHARGE CARRIER DYNAMICS IN NANOSTRUCTURED MOLECULAR LAYERS

Doctoral thesis

Physical sciences, physics (02 P)

Vilnius, 2013

Thesis was prepared at the Center for Physical Sciences and Technology 2009-2013

Scientific supervisor:

prof. habil. dr. Vidmantas Gulbinas (Center for Physical Sciences and Technology, physical scienes, physics – 02P)

VILNIAUS UNIVERSITETAS

FIZINIŲ IR TECHNOLOGIJOS MOKSLŲ CENTRAS

Domantas Peckus

ULTRASPARTI EKSITONŲ IR KRŪVININKŲ DINAMIKA NANOSTRUKTŪRIZUOTUOSE MOLEKULIŲ SLUOKSNIUOSE

Daktaro disertacija

Fiziniai mokslai, fizika (02 P)

Vilnius, 2013

Disertacija rengta 2009 – 2013 metais Fizinių ir technologijos mokslų centre.

Mokslinis vadovas:
prof. habil. dr. Vidmantas Gulbinas (Fizinių ir technologijos mokslų centras, fiziniai mokslai, fizika – 02P)

Table of contents

List of abbreviations

AEE – aggregation-enhanced emission

CT – charge transfer exciton

F8BT – poly-fluorene-co-benzotiadiazole

FSG – fluorene spiroconjugated group

ICT – internal charge transfer exciton

LED – light emitting diodes

OFET – organic field-effect transistors

OLED – organic light emiting diodes

OLEFET – organic light emitting field effect transistors

OSC – organic solar cells

PCBM – [6,6]-phenyl-C_{61}-butyric acid methyl ester

PDHS – poly-di-n-heksilsilane

PL – photoluminescence

PSF-BT – poly-spiro-bifluorene-co-benzothiadiazole

SH – second harmonic

TOF – time of flight

TREFISH - time-resolved electric field-induced second harmonic generation

Introduction

Organic electronics is currently one of the most rapidly developing research areas. Conjugated polymers and small molecule semiconductors attract considerable attention as active materials for optoelectronic applications. In many areas organic semiconductors can compete with inorganic semiconductors, even having some advantages in comparison with inorganic semiconductors, in application areas such as plastic ("soft") electronics, light emitting diodes [1] and photovoltaics [2]. In order to make organic semiconductors more competitive, their physical properties have to be explored in more detail. One of the most interesting physical properties of organic semiconductors is exciton and charge carrier dynamics, especially ultrafast dynamics that was not explored in detail yet. The importance of semiconducting properties of organic molecules shows the Noble Prize in Chemistry in 2000 to Alan J. Heeger, Alan G. MacDiarmid and Hideki Shirakawa for the discovery of conductivity of polymer polyacetylene [3].
During the following years, a lot of systematic research was done on the exciton and charge generation and transport properties of organic conjugated molecules [4].

At the moment, organic semiconductors have many applications that are being improved continuously. They are applied in organic light emiting diodes (OLEDs), field-effect transistors (OFETs) [5, 6], lasers [7] and solar cells [8] (OSCs). Despite high perspectives of organic semiconductors they are still upstaged by their inorganic counterparts. Series of scientific and technological studies were done recently in order to increase the competitiveness of organic semiconductors.

While at a moment it is quite a challenge for organic semiconductors to compete with their inorganic counterparts, the processing techniques for organic semiconductors are much simpler and cheaper. The main techniques are vacuum deposition and solution processing [9]. Epitaxial growth

commonly used for processing of inorganic semiconductors is much more complicated [10].

The efficiency of OLEDs is still chasing the one of inorganic LEDs, but OLEDs have some additional properties that LEDs do not possess. OLEDs could be made much smaller that LEDs enabling the use of OLEDs in monitors that can compete with common LCD technology and probably overrun it in future. At the moment, OLED's are already common in mobile phone displays [11]. In order to increase the efficiency of OLEDs, the charge injection, charges/excitons recombination efficiency, mobility of charge carriers should be optimized.

High-mobility OFETs are the basic units for a variety of high-performance electronic applications. Their development paves the way towards plastic electronics that is expected to complement silicon-based electronics. Further interest in organic optoelectronics has been generated by the realization of organic light emitting field effect transistors (OLEFETs) [12, 13]. OLEFETs are multifunctional devices that combine the current modulating function of a transistor with light emission. OLEFETs are based on organic semiconductors where it is possible to achieve the supramolecular organization leading to both, charge carrier transport and electroluminescence. They are attractive for both, fundamental studies and technological applications [6].

Since the first demonstration of laser oscillation, applications using lasers have spread to many areas, e.g. research, medicine, technology, and telecommunications. The variety of available laser sources is large and covers a wide span in terms of attainable wavelengths, output power, and pulse durations. Despite that, organic lasers could find their unique applications because of their potentially much lower physical dimensions. Organic lasers may be used for chemical sensing, lab-on-a-chip sensors for biophotonics, microspectroscopy labs [14].

Organic solar cells (OSCs) is one of the main fields where organic conjugated molecules are used [15]. OSCs do not achieve the efficiencies of their inorganic counterparts but their production techniques are much simpler

and cheaper. The main task of researches at the moment is to improve the efficiency and lifetime of organic photovoltaics. Their efficiency is not high enough to compete with inorganic counterparts, yet several processes should be optimized in order to increase power conversion efficiency of OSC. Main processes that determine the organic solar cell efficiency are light absorption, exciton diffusion, charge separation and charge collection. Charge carrier mobility is one of the crucial parameters that determine applicability of organic semiconductors for OSC. The main energy loses came from exciton and charge transfer exciton recombination, geminate and nongeminate recombination of charge carriers. Optical and electronic methods are employed for the investigation of these processes.

The main goal of this thesis is a detailed investigation of ultrafast exciton and charge carrier processes in pure organic semiconductors, their nanostructured composites and in their blends with fullerene derivatives. The point of interest of this thesis are the processes that happen in active layers of organic optoelectronic devices: light absorption, exciton diffusion, annihilation, formation of charge transfer excitons, exciton and charge transfer exciton recombination, charge pair and free charge carrier generation, geminate and nongeminate charge carrier recombination, charge carrier extraction from organic semiconductor. The influence of preparation techniques, concentration of fullerene derivatives, structure of nanocomposites to the mentioned processes was explored.

While π conjugation in carbon atoms is thoroughly explored, σ conjugation in bonds of silicon or germanium is still interesting. For better understanding of interaction of polysilanes with various nanostructures, thermochromic PDHS polymer incorporated in various nanocomposites was investigated.

All investigations can be grouped by explored materials, each of them has a separate chapter in this thesis. The research of each matter had a bit different purpose. The materials analyzed were molecules chains of poly-di-n-hexylsilane (PDHS) incorporated in various nanostructures; solutions and neat

films of poly-fluorene-co-benzotiadiazole (F8BT), poly-spiro-bifluorene-co-benzothiadiazol (PSF-BT) polymers, and PSF-BT blends with [6,6]-phenyl-C_{61}-butyric acid methyl ester (PCBM); solutions, neat films, and blends with fullerene derivatives of merocyanine MD376 small molecules.

The aims of investigation of PDHS molecules chains incorporated in various nanostructures.

- Influence of various nanostructures on PDHS polymer conformations and fluorescence properties.
- Comparison of nanocomposite and neat film fluorescence properties.

The points of exploration of F8BT, PSF-BT solvents, neat films, and PSF-BT blends with PCBM.

- Comparison of exciton diffusion and annihilation processes in F8BT and PSF-BT polymers.
- The influence of PCBM additives on exciton and charge carrier dynamics in PSF-BT films.

The goals of analysis of merocyanine MD376 solutions, neat films, and blends with fullerene derivatives.

- Detailed investigation of exciton and charger transfer exciton dynamics in MD376 neat films and their blends with fullerene derivatives.
- Exploration of generation of charge carriers, recombination and extraction processes in MD376 blends with fullerene derivatives, and evaluation of influence of fullerene concentration and film preparation techniques on the abovementioned processes.

Novelty and importance

Influence of morphology and orientation of the inorganic matrix on the conformational structure of incorporated polymer chains and emission properties of nanocomposites was explored. It was estimated that

nanocomposite films are promising technologically and a convenient approach for preparation of polymer films with improved fluorescence properties.

Internal charge transfer state formation in PSF-BT films was explored in detail, as well as the role of PCBM additives on the charge carrier generation and drift in PSF-BT polymer. Charge transfer scheme of the formation of long-lived charge pair state in PSF-BT/PCBM blend has been discovered. Copolymers incorporating electron donating and accepting groups are currently the "state of the art" materials for various organic optoelectronic devices, which requires deeper knowledge of the electronic processes in these complex materials.

Ultrafast exciton and charge carrier dynamics in merocyanine materials has been experimentally explored in detail for the first time. These findings provide knowledge about the formation and dissociation of charge transfer excitons and charge pairs and generation of free charge carriers. Influence of sample fabrication techniques on the exciton and charge carrier dynamics was also studied. These materials are particularly promising for the organic solar cell fabrication, and the investigated properties are closely related to their operation efficiency.

Layout of the thesis

Chapter 1 overviews π and σ- conjugated polymers and small molecules. It also overviews the practical application of conjugated molecules, especially π – conjugated polymers and small molecules for organic solar cells. Properties of investigated polymers (F8BT, PSF-BT and PDHS) and small molecules (MD376) are discussed. OSC other organic electronic devices structure and operation principles are briefly reviewed. Energy loses in OSC that lead to lower efficiency are also mentioned.

Chapter 2. The investigation techniques are introduced. Steady-state absorption, steady-state and dynamic fluorescence, transient absorption, photocurrent measurements, especially the TREFISH method are discussed.

Chapter 3 is dedicated to the investigation of PDHS in various nanocomposites. Dependence of fluorescence spectra on temperatures and nanocomposites is explored.

In Chapter 4, exciton diffusion, annihilation and their role in the charge carrier generation in fluorene based copolymers F8BT and PSF-BT are discussed. The investigations have been performed by means of femtosecond transient absorption combined with photoluminescence and photoconductivity measurements. Optical generation of charge carriers and their transport in blends of the spirobifluorene-co-benzothiadiazole copolymer (PSF-BT) and the electron acceptor phenyl-C61-butyric acid methyl ester (PCBM) have been investigated by means of time-resolved fluorescence, transient absorption as well as by integral mode time-of-flight method and its ultrafast all-optical analogue based on electric field-induced second harmonic generation.

In Chapter 5 the results of merocyanine MD376 investigations are presented. The investigations are directed towards better understanding of ultrafast electronic processes in organic solar cells based on merocianine/fullerene blends. The performed optical and optoelectrical investigations cover wide range of dynamic processes giving information on the charge carrier dynamics starting from their generation till extraction from the sample.

The author contribution

Most of the obtained experimental results presented within the thesis have been carried out by the author under the guidance of prof. V. Gulbinas.

Polysilanes were prepared by prof. Nina Ostapenko from the Institute of physics, Kyiv, Ukraine. Polyfluorene derivatives and merocyanines were prepared by dr. Dirk Hertel from the Department of chemistry, Physical Chemistry, University of Cologne, Cologne, Germany.

The author contributed to the data analysis and preparation of publication manuscripts and conference presentations.

Acknowledgements

There is not enough space to thank everybody, therefore if I did not mention you please don't think that you were forgotten.

First I would like to thank my supervisor prof. Vidmantas Gulbinas for great confidence, endless support and inexhaustible ideas.

Dr. Andrius Devižis, thank you for your useful experimental advice, discussions and help with the setup development.

I would also like to express my gratitude dr. Dirk Hertel and prof. Nina Ostapenko for providing samples, cooperation and discussions.

Dr. Ramūnas Augulis and dr. Marius Franckevičius for discussions, reading my thesis manuscript and giving valuable criticism.

Dr. Renata Karpicz for scientific advices and discussions.

My present co-workers dr. Danielis Rutkauskas and dr. Andrei Dementjev.

I'm also thankful to the whole Center for Physical Sciences and Technology and especially to Department of Molecular Compound Physics.

My present co-workers: Egidijus Songaila, Vytenis Pranciulis and past co-workers: Skomantas Puzinas, Jūris Kiškis, Kęstutis Budzinauskas, I wish you success in your PhD studies.

Students: Paulius Naujalis, Aušra Gustainytė, Simona Streckaitė, Aivaras Kazakevičius, Milda Petkelytė, Rasa Valentinavičienė and all the others.

Thanks to all my friends.

Finally, I wish to thank my parents and my brother for their great support during the long period of studies.

Main statements

1. Incorporation of PDHS polymer in nanostructured inorganic films causes exciton localization and suppression of their nonradiative exciton decay.

2. Ultrafast intramolecular charge transfer in PSF-BT polymer causes formation of weakly mobile excitons and suppresses nonlinear exciton-exciton annihilation.

3. PCBM additives play unusual role in photoconductivity of PSF-BT polymer. Contrarily to common they decrease the initial photoconductivity. Which is related to two processes: exciton quenching and trapping of generated electrons. Both of them reduce the number of mobile charge carriers.

4. The charge pairs in merocyanine solar cells are generated by two processes: a) field-independent generation because of nonrelaxed exciton disociation and b) dissociation of CT states during their entire lifetime. High electron mobility and diffusion coefficient in fullerene domains is mainly responsible for the efficient charge pair generation in merocyanine/fullerene blends.

Approbation

List of publications related to the thesis:

1. N. I. Ostapenko, N. V. Kozlova, E. K. Frolova, Yu. V. Ostapenko, D. Peckus, V. Gulbinas, A. M. Eremenko, N. P. Smirnova, N. I. Surovtseva, S. Suto, and A. Watanabe, Spectral properties of organosilicon polymer/ SiO_2 porous film nanocomposite films, Journal of Applied Spectroscopy, **78**, 75 (2011).
2. N. Ostapenko, P. Vodolazkyy, D. Peckus, V. Gulbinas, V. Moiseenko, N. Surovtseva, S. Suto, A. Watanabe, Spectroscopy of Nano-Sized Polysilanes Confined by Different Structures of Silica, Mol. Cryst. Liq. Cryst., **536**, 41 (2011).

3. D. Peckus, A. Devižis, D. Hertel, K. Meerholz, V. Gulbinas, Exciton diffusion, annihilation and their role in the charge carrier generation in fluorene based copolymers, Chem. Phys., **404**, 42 (2012).
4. D. Peckus, A. Devižis, D. Hertel, V. Gulbinas, Ultrafast excitonic processes in merocyanine solutions, films and its blends with fullerenes, Proceeding of 4rd international conference radiation interaction with material and its use in technologies (2012).
5. D. Peckus, A. Devižis, D. Hertel, V. Gulbinas, Excited state relaxation in vacium deposited and solution processed films of merocyanine/fulerene blends, Proc. NAP **1**, 04NEA10-1 (2012).
6. D. Peckus, A. Devižis, R. Augulis, S. Graf, D. Hertel, K. Meerholz, V. Gulbinas, Charge transfer states in merocyanine neat films and its blends with [6,6]-phenyl-C_{61}-butyric acid methyl ester, J. Phys. Chem. C, **117**, 6039 (2013).
7. A. Devižis, D. Peckus, D. Hertel, K. Meerholz, V. Gulbinas, Charge carrier generation and transport in a polyfluorene copolymer with electron donating side groups doped with PCBM, J. Phys. Chem. C, **117,** 15871 (2013).
8. N. Ostapenko, Yu. Ostapenko, O.Kerita, D. Peckus, V. Gulbinas, A. Eremenko, N. Smirnova, N. Surovtseva, Luminescence features of nanocomposites of silicon-organic polymer/porous SiO2 and TiO2 films, Synthetic metals, submitted.
9. V. Gulbinas, A. Devižis, D. Peckus, D. Hertel, Ultrafast optical probing of carrier motion in conjugated polymers and blends for solar cells, Proceedings of ICMAT 2013, accepted.
10. D. Peckus, A. Devižis, R. Augulis, S. Graf, D. Hertel, K. Meerholz, V. Gulbinas, Charge carrier generation in merocyanine/fullerene blends investigated by the fluorescence quenching and ultrafast time resolved photocurrent, manuscript under preparation.

List of conference theses:

1. D. Peckus, A. Devižis, V. Gulbinas „Exciton-exciton annihilation and charge carrrier generation in fluorene based conjugated polymers“, Developments in optics and comunications 2010, 23-25 April 2010, Ryga, Latvia.
2. N. Ostapenko, P. Vodolazkyy, D.Peckus, V. Gulbinas, V. Moiseenko, S.Suto, A. Watanabe, „ Sectroscopy of nanosize polysilanes confined by different structures of silica“, ICEPOM-8, 17-22 May 2010 Ivano-Frankivs‘k region, Ukraine.
3. D. Peckus, A. Devižis, V. Gulbinas, D. Hertel „Charge carrier generation via exciton-exction annihilation in fluorine based conjugated polymers“ , Advanced materials and technologies, 27-31 August 2010, Palanga, Lithuania.
4. A. Devižis, D. Peckus, V. Gulbinas „Exciton dynamics and charge carrier generation in multifunctional fluorene-based conjugated polymers“, Baltic polymer symposium, 8-11 September 2010, Palanga, Lithuania.
5. N. Ostapenko, P. Vodolazkyy, D.Peckus, V. Gulbinas, V. Moiseenko, N. Surovtseva „Fluorescence properties of polysilanes confined in different silica nanostructures“ Baltic polymer symposium, 8-11 September 2010, Palanga, Lithuania.
6. D. Peckus, A. Devižis, V. Gulbinas, D. Hertel „Exciton-exciton annihilation and charge carrrier generation in fluorene based conjugated polymers“, Optics and High Technology Material Science SPO 2010, 21-24 October, Kyiv, Ukraine.
7. D. Peckus; N. Ostapenko; P. Vodolazkyy.; V. Moiseenko.;S. Suto; A. Watanabe and V. Gulbinas, Fluorescence spectroscopy analysis of polysilanes confined in different SiO_2 and TiO_2 nanostructures, Developments in optics and communications 2011, 28-30 April 2011, Riga, Latvia.

8. D. Peckus, N. Ostapenko, P. Vodolazkyy, V. Moiseenko, S. Suto, A. Watanabe and V. Gulbinas, “Spectroscopic analysis of polysilanes confined in different SiO_2 and TiO_2 nanostructures”, ERPOS-12, 11-13 July 2011, Vilnius, Lithuania.
9. D. Peckus; A. Devižis; V. Gulbinas and D. Hertel, Exciton diffusion, annihilation and nonlinear charge carrier generation in polyfluorene based conjugated polymers, Advanced materials and technologines 2011, 27-31 August 2011 ,Palanga, Lithuania.
10. N. Ostapenko, Yu. Ostapenko, D. Peckus, V. Gulbinas, S. Suto, A. Watanabe, Specific optical properties of nanocomposite films based on polysilanes restricted by porous silica and titanium, XX international school-seminar of Galyna Puchkovska spectroscopy of molecules and crystals, 20-27 September 2011, Beregove, Crimea, Ukraine.
11. D. Peckus, A. Devižis, D. Hertel ir V. Gulbinas, Krūvininkų generacija, eksitonų difuzija ir anihiliacija iš polifluorenų sudarytuose organiniuose polimeruose, 39-oji Lietuvos nacionalinė fizikos konferencija, spalio 6-8 d. 2011, Vilnius, Lietuva.
12. D. Peckus, A. Devižis, D. Hetel and V. Gulbinas, Ultrafast proceses in excited merocyanine MD376 films, Developments in optics and comunications 2012, 12-14 April 2012, Ryga, Latvia.
13. D. Peckus, A. Devižis, D. Hetel and V. Gulbinas, Ultrafast excitonic processes in merocyanine solutions, films and its blends with fullerenes, 4rd International conference Radation interaction with material and it suse in technologines 2012, 14-17 May 2012 Kaunas, Lithuania.
14. D. Peckus, A. Devižis, D. Hertel and V. Gulbinas, Excited state dynamics in merocyanine films and their blends with fullerene derivatines, 5th International symposium on flexible organic Electronics, 2-5 July 2012, Thessaloniki, Greece.
15. A. Devižis, D. Peckus, D. Hertel and V. Gulbinas, Charge Cartier generation and transport in films of neat conjugated polymers and blends

with fullerene derivatines, 5th International symposium on flexible organic Electronics, 2-5 July 2012, Thessaloniki, Greece.

16. D. Peckus, A. Devižis, D. Hertel and V. Gulbinas, Exciton dynamics in films of pure merocyanines and its blends with fullerenes, 14th International conference-school advanced materials and technologines, 27-31 August 2012, Palanga, Lithuania.
17. V. Gulbinas, A. Devižis, D. Peckus, V. Abramavičius, Ultrafast Cartier motion in organic blend-based solar cells, 2nd International conference nanomaterials: applications and properties-2012, 17-22 September 2012, Alushta, the Crimea, Ukraine.
18. D. Peckus, A. Devižis, D. Hertel and V. Gulbinas, Excited state relaxation in vacuum deposited and solution processed films of merocyanine/fullerene blends, 2nd International conference nanomaterials: applications and properties-2012, 17-22 September 2012, Alushta, the Crimea, Ukraine.
19. D. Peckus, A. Devižis, D. Hertel, and V. Gulbinas, Ultrafast exciton and charge carrier dynamics in pure merocyanine films and its blends with fullerene, 6th international meeting on molecular electronics, 3-7 December 2012, Grenoble, France.
20. D. Peckus, A. Devižis, D. Hetel and V. Gulbinas, Charge carrier generation in merocyanine blends with fullerene derivatives, Developments in optics and comunications 2012, 10-12 April 2013, Ryga, Latvia.
21. D. Peckus, A. Devižis, D. Hetel and V. Gulbinas, Exciton and charge carrier dynamics in merocyanine films and its blends with fullerene, Electronic processes in organic materials 9-th international conference, 20-24 May, Lviv, Ukraine.
22. D. Peckus, A. Devižis, D. Hetel ir V. Gulbinas, Ultrasparti laisvųjų krūvininkų generacija merocianino mišiniuose su fulereno dariniais, 40-oji Lietuvos nacionalinė fizikos konferencija, birželio 10-13 d. 2013, Vilnius, Lietuva.

23. V. Gulbinas, D. Peckus, A. Devižis, D. Hertel and K. Meerholtz, Charge carrier generation and transport in merocyanine: fullerene blends for solar cells, 7th international conference on materials for advanced technologies, 30 June – 5 July, Suntec Singapure.

Student and PhD student conferences

1. D. Peckus, A. Devižis, V. Gulbinas, D. Hertel „Eksitonų-eksitonų anihiliacija ir krūvinikų dinamika fluoreno organiniuose polimeruose“, FizTeCh 2010, 18-19 lapkričio, Vilnius, Lietuva.
2. D. Peckus, N. Ostapenko, P. Vodolazkyy, V.Moiseenko, S. Suto, A. Watanabe ir V. Gulbinas Polisilanų įterptų į skirtingas SiO_2 ir TiO_2 nanostruktūras fluorescencinė spektroskopija, I -oji Jaunųjų mokslininkų konferencija Fizinių ir technologijos mokslų tarpdalykiniai tyrimai 2011, 8 vasario, Vilnius, Lietuva.
3. D. Peckus, A. Devižis, D. Hertel, K. Meerholz ir V. Gulbinas, Eksitonų dinamika merocianino molekulėse, bei jų mišiniuose su fulerenu, FizTeCh 2011, 24-25 lapkričio, Vilnius, Lietuva.
4. D. Peckus, A. Devižis, D. Hertel, K. Meerholz ir V. Gulbinas, Eksitonų dinamika merocianino molekulėse, bei jų mišiniuose su fulerenu, II -oji Jaunųjų mokslinkų konferencija Fizinių ir technologijos mokslų tarpdalykiniai tyrimai 2012, 14 vasario Vilnius, Lietuva.
5. D. Peckus, A. Devižis, D. Hertel ir V. Gulbinas, Ultrasparti krūvininkų dinamika merocianino mišiniuose su fulerenu, FizTeCh 2012, 25-26 rugsėjo, Vilnius, Lietuva.

List of author's publications not included into the thesis:

1. A. Devižis, A. Serbenta, D. Peckus, A. Thiessen, R. Alle, K. Meerholz, D. Hertel, and V. Gulbinas, Electric field assisted charge carrier photogeneration in poly(spirobifluorene-co-benzothiadiazole), J. Chem. Phys., 133, 164904 (2010).

1 Organic materials for optoelectrical applications and devices

1.1 π and σ conjugation

Organic molecules are large class of molecules containing carbon atoms except of few molecules, which have carbon, but are called inorganic. π bonds are responsible for delocalization of electron density in π conjugated molecules. The carbon atoms in these bonds are sp^2 hybridized, which leaves one orbital (p_z) unhybridized, perpendicular to the chemical bond direction. Electrons in these alternately overlapping orbitals form a π-electron cloud, delocalized over the conjugation length of the molecule (Fig. 1.1). Because of conductivity properties these materials they are called organic semiconductors.

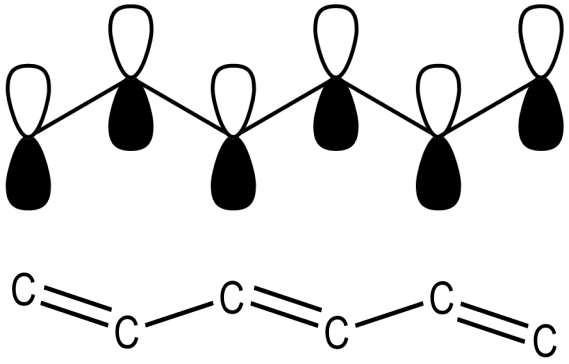

Fig. 1.1. Schematic representation of p_z orbitals overlap in a conjugated segment of a polymer.

Organic semiconductors can be made from conjugated molecules, with filled bonding π-orbital and nonocupied antibonding π^*-orbital, also-called highest occupied molecular orbital (HOMO) and lowest unoccupied molecular orbital (LUMO), respectively. HOMO and LUMO are separated by a bandgap, typically of the order of one to three electronvolts, making such an organic compound a semiconductor. $\pi \rightarrow \pi^*$ transition between these two levels can be excited by UV, visible or near IR light. Semiconducting and light absorbing

properties make conjugated organic compounds very perspective choice for various applications like photovoltaics, transistors and others.

Organic semiconductors can have a structure of polymer or small molecules. A polymer is a molecule which structure is composed of multiple repeating units from which originates high relative molecular mass and attendant properties. While small molecules are composed of one or few repeating units (oligomers) with relatively low molecular mass.

Conjugated polymers are promising candidates for their applications in many kinds of organic optoelectronic devices. Not only the mechanical properties, but also the electronic properties of polymers, can be tailored by sophisticated synthetic methods.

Despite well known and properly explored π conjugation of carbon atoms, σ conjugation in polymers formed by silicon or germanium atoms also exists. $\sigma \rightarrow \sigma^*$ bond excitation is typical for sp^3 hybridized carbon, silicon and germanium based molecules. Excitation of C – C bonds of organic molecules requires much high energy photons ($\lambda < 150$ nm). Excitation of silicon and germanium based polymers need much lower energy photons than for carbon based polymers (290-410 nm). That is interesting, because absorbed energy by silicon and germanium should be quite similar to sp^2 hybridized carbon based polymers. This difference is explained by σ conjugation in bonds of silicon and germanium atoms. Orbitals of these bonds overlap forming σ conjugation (Fig. 1.2).

Fig. 1.2. σ conjugation of Si atoms

In most cases, σ conjugation consists of 10 – 20 silicon or germanium atoms. In contrast to π conjugation, σ conjugation is not explored in so much detail. π – σ conjugation is other interesting type of conjugation. Currently many experiments are done in order to investigated interaction between π and σ conjugations[16] but this kind of research is not done in these thesis.

Absorptions regions of π and σ conjugated molecules are different. Absorption of π conjugated molecules range from ultraviolet to near infrared. While the bandgap of σ conjugation between HOMO and LUMO in most cases is higher than in π conjugated compounds, typically from three to four electron volts (290 <λ < 410 nm). Nevertheless, fluorescence quantum yield of σ conjugated molecules in most cases is higher than that of π conjugated molecules. This shows prospects for LED fabrication.

Investigation of the properties of these polymers attracts attention of scientists because of their possible use as photodiodes, photoresistors, and materials for nonlinear optics [17–19]. σ conjugation molecules (polysilanes) have also a serious disadvantage over π conjugation molecules: photooxidation under UV light exposure (Fig. 1.3). This problem has been tried to solve by incorporating polysilanes into various nanopores like SBA-15 (Santa Barba amorphous (hexagonal mesoporous silicon type with diameter of 4.6-30 nm)), MCM-41 (Mobil Crystalline Materials (hexagonal mesoporous silicon type with diameter of 1.8-10 nm)) and other SiO_2 and TiO_2 nanopores (See 1.3.1 chapter below). Nanopores protect polysilanes from degradation by stabilizing their chains.

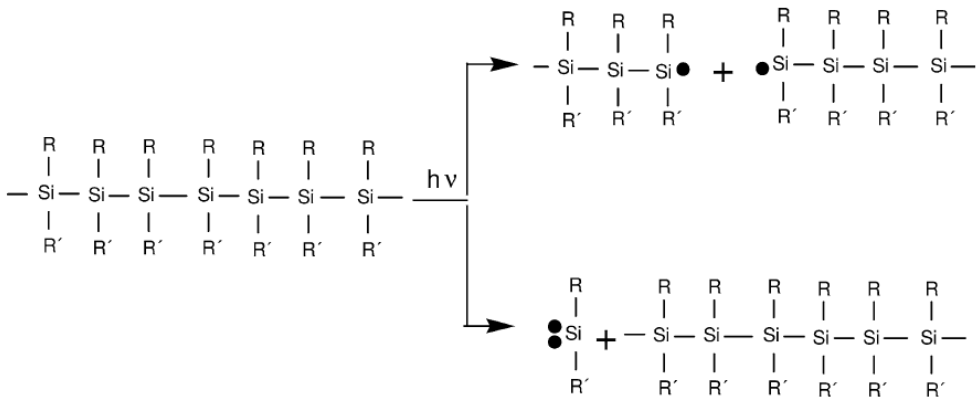

Fig. 1.3. Degradation of polysilanes in ultraviolet light.

Below (1.3 chapter) we shortly discuss the main classes of molecules investigated in this work.

1.2 Devices of organic materials

Organic semiconductors can be used in many applications like organic light emitting devices (OLED), organic displays based on OLED, organic field-effect transistors (OFET), photocopying, optically and electrically pumped organic lasers, and organic solar cells. The main points of interest of this thesis are ultrafast processes taking place in active layers of these devices under their optical excitation. All applications will be discussed later in more detail.

1.2.1 Organic light emitting devices

Efficient lectroliuminescence of conjugated organic polymers was discovered in 1990 [20]. The research and development in the use of organic molecules as active semiconductors in light emitting devices have advanced very rapidly. Recently, organic polymer or small molecule based organic light emitting devices reached features required for widespread application in electronic devices. OLEDs are seen very promising due to efficient light generation, mechanical flexibility, and easy, low-cost manufacture using solution processing.

It is well setablished that there are three main proceses governing OLED performance: charge injection, charge transport, charge/exciton recombination. Charges are injected from electrodes into the polymer layer under forward bias voltage. Holes and electrons are transported towards each other in the applied field. Then electrons face holes and excitons are formed because of Coulomb attraction. Light is emitted upon exciton recombination. Langevin theory is commonly used for explanation of exciton recombination in OLEDs. The photophysics of neutral excited state in organic molecules is important for the device performance and their further improvement.

1.2.2 Organic field-effect transistors

In 1987, H. Koezuka and co-workers reported the first organic field-effect transistor based on a polymer of thiophene molecules. High-mobility OFETs are the basic units for a variety of high-performance electronic applications. Their development paves the way towards plastic electronics, that is expected to complement silicon electronics. Further interest in organic optoelectronics has been generated by the realization of organic light emitting field effect transistors (OLEFETs) [12, 13]. OLEFETs are based on organic semiconductors where it is possible to achieve the supramolecular organization leading to both, charge carrier transport and electroluminescence. OLEFETs are multifunctional devices that combine the current modulation function of a transistor with light emission.

An OFET is a three electrode device. The organic active layer is in contact with source (S) and drain (D) electrodes whereas it is isolated from the gate (G) electrode by the gate dielectric. The region of organic active layer delimited by the S and D electrodes defines the transistor channel whose geometry is characterized by the interelectrode distance (L) and the electrode width (W). On application of an appropriate gate electrode bias, holes and electrons are injected from the S and D electrodes into the transistor channel, where they move under the action of a drain-source bias. The magnitude of the current flowing between the S and D electrodes is modulated by the gate bias, which is also used to turn the device from the off to the on state. If the organic semiconductor is electroluminescent, holes and electrons form excitons that recombine radiatively to generate light in the transistor channel. It is supposed that OLEFETs light emission efficiency may overrun OLEDs [5, 6].

1.2.3 Optically and electrically pumped organic lasers

Since the first demonstration of a laser, laser applications have been spread to many areas, such as scientific research, medicine, telecommunications, and technology. The variety of available laser sources is large in terms of wavelengths, output powers and pulse durations. Although they can be implemented in many different ways, lasers are always composed of tree essential building elements: a gain medium, a pump source, and a resonator. The gain medium in which amplification of light occurs by stimulated emission of radiation can be in a gaseous, a liquid, or a solid form.
Despite various kinds of laser materials, π-conjugated small molecules or polymers may be of interest for fabrication of the family of organic lasers. Electrically pumped organic lasers remains a field that inspires scientific community. Much scientific research has been contributed to better understanding of the bottlenecks caused by the supplementary losses brought by electrical excitation. Till now, no electrically pumped organic laser was created, nevertheless organic lasers can be pumped optically and may be used in practice [21–26].

Organic lasers are broadly tunable coherent sources, potentially compact, convenient and manufactured at low cost. The simplicity of their fabrication process makes organic sources attractive for integration into miniature spectroscopic systems. In a similar way, organic lasers are potentially useful for chemical sensing, lab-on-a-chip sensors for biophotonics, coupled to microfluidic devices; organic lasers may also find a place in data communications.

1.2.4 Organic solar cells

Solar cells are clean and renewable energy source. The availability of solar energy by far exceeds any potential future energy demands. In fact, the

amount of sun energy that reaches earth per hour (1.4×10^{30} J) is larger that of the energy needed by mankind per year [2, 27].

In 1839, Alexander Edmond Becquerel observed the emerge of a photocurrent when platinum electrodes covered with silver halide were illuminated in aqueous solution for the first time; this observation has ever since been known as the photovoltaic effect [28]. At this moment there are many kinds of solar cells: crystalline and thin-films silicon solar cells, cadmium telluride solar cell, Gallium arsenide multijunction solar cells, organic solar cells, dye-sensitized solar cells and hybrid technologies [29]. The most common at the moment are silicon solar cells. The efficiency of silicon solar cells depends on technology of fabrication and ranges from 13 to 25 %. The most efficient are gallium arsenide multijunction solar cells with the efficiency of reaching about 44% [30, 31]. The highest efficiency of organic solar cells is 12 % which recently was recorded by Heliatek [32, 33]. Despite large difference in efficiency, organic solar cells would become useful and competitive for certain applications if their efficiency could consistently exceed 10%. The efficiency is not the only important parameter: low fabrication cost, light-weight, flexibility, simple fabrication, and ability to create complex structures makes organic solar cells very interesting and useful for future energy sources. Theoretically, the efficiency of organic solar cells can reach over 15 % [2], that would make their efficiency compatible to silicon solar cells, but more recent, more fundamental descriptions suggest limits of 20–24% to be reachable [34].

In the race for efficient OSCs, two processing techniques were established: 1) dry processing (thermal evaporation) for planar-heterojunction and bulk-heterojunction solar cells and 2) solution processing (spin-coating, inkjet printing, dip-coating, spraying techniques) for bulk-heterojunction solar cells [9].

The efficiency difference between organic and inorganic solar cells appears from different physical properties of their excitons (electron-hole pairs). When the active layer in inorganic solar cells is excited, free charge

pairs (weakly bond type Wannier-Mott excitons) appear. While in organic solar cells, excitons have to be dissociated into charge pairs (see below). The difference between organic semiconductors and inorganic semiconductors is the presence of tightly bonded excitons resulting from their low dielectric constant ($\varepsilon_r \approx 2\text{-}4$). The excitons in organic semiconductors are called Frenkel or molecular excitons, their binding energy is in the range of 0.3-1 eV [34]. Such large binding energy prevents exciton dissociation by an electric field and temperature. Therefore, the organic solar cells with one type of molecules have very low power-conversion efficiency (PCEs) far below 1% for solar spectrum. The introduction of second organic layer was a big leap in terms of PCEs. Tang [35] introduced the donor-acceptor bilayer planar heterojungtion for the OSCs in 1979, and achieved PCEs of around 1%. The energy difference between the LUMO of the donor and HOMO of the acceptor provides the driving force for the dissociation of Frenkel excitons [2]. The difference between the electron energy on the donor and the corresponding acceptor level has to be larger than the exciton binding energy in order to initiate charge transfer from donor to acceptor material [36]. If the exciton reaches heterointeface by diffusion, it is energetically favorable for the electron to be transferred to the acceptor molecule. This charge transfer is reported to take less than 100 fs [34].

One of the major breakthroughs in OSC technology was the adoption C_{60} fullerene and its derivatives (such as [6,6]-phenyl-C_{61}-butyric acid methyl ester, PCBM) to replace the electron acceptor type molecules in OSC devices. Due to their strong electronegativity and high electron mobility, C_{60} and C_{70} derivatives have become standard electron acceptor molecules in OSC devices. Basic structure principle of organic solar cells is shown in fig. 1.4. In an organic donor-acceptor solar cell, light is usually absorbed mostly in the donor material: conjugated small molecule or polymer.

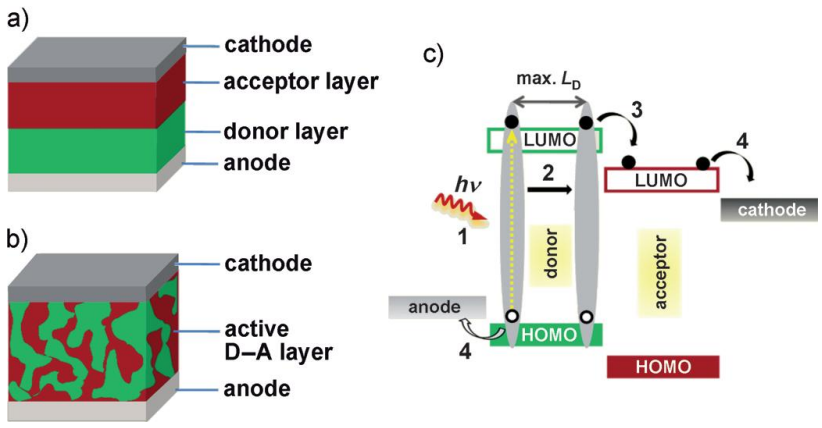

Fig. 1.4.Typical OSC devices based on donor-acceptor heterojunction architectures [27]. a) Planar heterojunction configuration. b) Bulk heterojunction configuration. c) Fundamental steps occurring in donor-acceptor heterojunction solar cells.

Fundamental steps occurring in donor-acceptor heterojunction solar cells fig. 1.4c:

1) Photoexitation of the donor to generate an exciton (electron–hole pair bound by Coulomb interactions).

2) Exciton diffusion to the D–A interface. Excitons that do not reach the interface recombine and do not contribute to the photocurrent (longer diffusion length, LD).

3) Dissociation of bound excitons at the D–A interface to form a geminate electron–hole pair (increased interfacial charge separation requires optimal energy offset between HOMO-LUMO of the donor and HOMO-LUMO of the acceptor material).

4) Free charge carrier transport and collection at the external electrodes [27].

Organic semiconductors exhibit very high absorption coefficients above 10^7 m^{-1}. Consequently, very low thickness between 100-300 nm are sufficient for a good absorption yield in organic photovoltaic devices. In contrast, for crystalline silicon solar cells more than 100 microns of active layer is needed. Thus, lower amounts of materials are needed for organic solar cells.

Basic structure of planar junction concept shown in fig. 1.4a. Planar heterojunction solar cell basically consist of two electrodes cathode and anode and two planar layers of molecules which have electron donating and accepting properties [27].

The mentioned planar junction concept has certain limitations, including small surface area between the donor-acceptor interface and the requirement of long exciton lifetime to ensure that the excitons reach heterojunction. This problem can be addressed by introducing a bulk heterojunction, which involves mixing donor-acceptor materials in the bulk body of the OSC device. The first efficient bulk heterojuntion OSC were independently realized in 1995 by groups of Heeger and Friend in polymer-fullerene and polymer-polymer blends [37]. Recently, researchers discovered that morphology (the donor-acceptor phase separation) also plays a critical role in achieving high efficiency solar cells [2].

Essential parameters determining the cell performance are open-circuit voltage (V_{oc}), short-circuit current density (J_{sc}), fill factor (FF). In order to increase the OSC efficiency all of these parameters have to be increased. V_{oc} represents the maximum photovoltage measured in a solar cell, which is found to depend mainly on the organic material and the energetic level of their frontier orbitals, that is the energy difference of the HOMO level of donor and LUMO level of the acceptor. However, V_{oc} can also be influenced by charge recombination processes, which cannot be completely avoided, resulting in a lower maximum V_{oc}.

J_{sc} represents the maximum photocurrent that could be obtained in a solar cell. This photocurrent depends on the number of absorbed photons that can be exploited by the solar cell as long as no saturation effects occur. J_{sc} also depends on the surface area of photoactive layer, the device thickness, and optimization of the absorption spectra to harvest more photons over solar spectrum. Charge transport properties of organic semiconductors also play an important role to obtain a high J_{sc}.

The FF describes the quality of the solar cell and is determined by the photogenerated charge carriers and the fraction of charge carriers that reaches the electrodes. FF depends on the competition between charge carrier recombination and transport processes. It is quite a complicated task to increase all these parameters at once.

Power conversion efficiency (η) is determined by the ratio of power that device produces (P_{out}) and the power of the incident light (P_{in}).

$$\eta = \frac{P_{out}}{P_{in}} = \frac{V_{oc} J_{sc} FF}{P_{in}} \tag{1.1}$$

The external quantum efficiency (EQE) is defined by the number of photogenerated charge carriers over the number of incident monochromatic photons as a function of wavelength (λ), ultimately being the product of four efficiences (η): light absorption (A), exciton diffusion (ED), charge separation (CS) and charge collection (CC), giving $EQE = \eta_A(\lambda) \times \eta_{ED}(\lambda) \times \eta_{CS}(\lambda) \times \eta_{CC}(\lambda)$. Fig. 1.5.

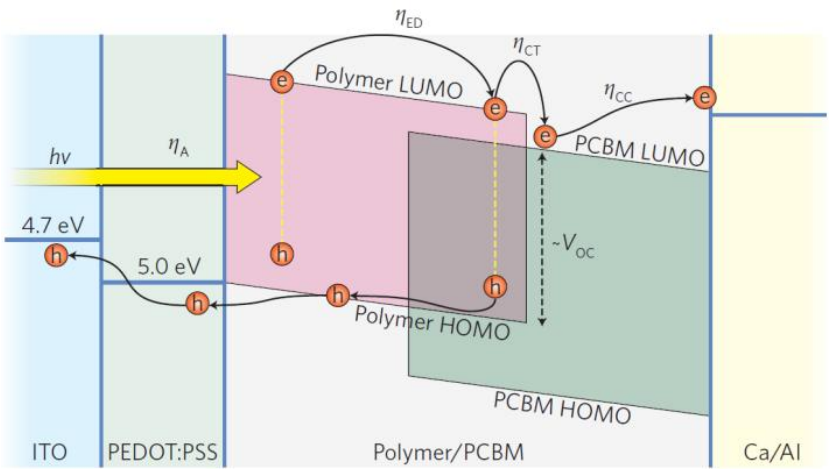

Fig. 1.5. The operating mechanism of organic solar cells. The processes that influences EQE of OSC [2].

OSCs are divided into two different categories according to whether small molecular mass molecules or polymers are employed as active layers. These two classes of materials are rather different in terms of their synthesis,

purification, and device fabrication processes. Polymer solar cells are processed from solution in organic solvents, whereas small-molecule solar cells are processed mainly using thermal evaporation deposition in a high-vacuum environment [9].

1.2.2 Challenges of improving organic solar cells efficiency

Shockley and Queisser (SQ) made the first calculation of the limiting power conversion efficiency of a photovoltaic device in the case when all the avoidable losses could be switched off. According to this model, the efficiency peaks at a value of around 33% at E_g = 1.3–1.4 eV [34]. Organic solar cells operate at higher energies, therefore the efficiency peak is lower. While SQ limit shows the highest possible efficiency of organic solar cells, there are a lot processes that decrease it even more.

Energy conversion in organic solar cells relies on several steps: light absorption, exciton transport, exciton dissociation, polaron pair dissociation, charge transport and recombination, charge extraction. Regrettably, not all of these processes have a high efficiency (fig. 1.5) [2, 38]. The increasing efficiency of these processes is a huge scientific challenge at the moment.
All the processes in organic solar cells will be discussed more detail below.

Absorption. First, singlet excitons are generated by incident photons and, if excitons are not directly situated next to a donor-acceptor interface, exciton diffusion within the donor toward the acceptor material occurs.

Exciton transport. As excitons have only limited lifetime of typically less than 1 ns, they can move only over a diffusion length of 3-30 nm for small molecules and 3-15 nm for polymers before they recombine [34]. Organic single crystals can have exciton diffusion lengths in excess of 100 nm, which have the potential as electron donor of efficient bilayer solar cells, but have not been exploited yet. In a well-optimized organic solar cell, most excitons are dissociated by charge transfer to the acceptor, which is a very efficient process

and occurs on the femtosecond time scale. The absorption length is around 100 nm, while commonly diffusion length are on the order of few nanometers. The distance from any point within the donor phase to the donor-acceptor interface including the charge transfer should ideally never exceed the excitation diffusion length. At the moment, not much research has been done in order to increase the diffusion length. Much more investigation is directed towards creating effective solar cells with diffusion lengths that readily exist [4, 34].
The diffusion length (L) depends on the lifetime of singlet excitons (τ) and exciton diffusivity (D) $L = \sqrt{D\tau}$.

Forster resonance energy transfer (FRET) theory plays crucial role in exciton transfer. Exciton diffusion is often modeled using FRET. Since energy must be conserved, the acceptor molecule must have energy states available such that gain in energy of the acceptor is equal to the loss in energy of the donor molecule. The available energy states can be determined experimentally by measuring the absorption spectrum and fluorescence spectrum of the acceptor and donor species.

Exciton recombination. The exciton recombination loss mechanism in OSCs will be discussed. Singlet excitons that are not generated sufficiently close to the donor-acceptor interface to either dissociate directly or, after diffusion, can undergo recombination to the ground state or via intersystem crossing into the triplet state. Such recombination events are monomolecular, as it describes the decay of a single excitation. Therefore, the intrinsic exciton lifetimes do not depend on the concentration of the species, and thus, are independend of the light intensity. Within this definition, monomolecular recombination is always a first-order decay.

Intersystem crossing of a singlet to a triplet exciton is a process typically on the nanosecond to microsecond timescale. Despite actually being parity forbidden, it occurs in many organic semiconductors due to heavier atoms within the molecules. This process competes, for instance, with decay by photoluminescence or in a blend, charge transfer. After triplet formation energy is lost, unless materials with direct triplet photogeneration are

considered but most donor-acceptor systems are not designed to favor the dissociation of triplet excitons.

Another recombination mechanism, especially at high fluences found in most pulsed laser experiments, is exciton-charge annihilation, also called exciton-polaron quenching. Also, singlet-singlet and singlet-triplet recombination, both nongeminate processes showing a second-order decay can occur at high light intensities, but seem not to be relevant for the working regime of OSCs.

Recombination of charge transfer excitons. Another loss mechanism on OSCs is recombination of charge transfer (CT) excitons. Recombination of CT complexes to the ground state is a geminate process and thus, shows a first-order decay with lifetimes observed for radiative losses on the order of nanoseconds. Consequently, the recombination is independent of the concentration of species and thus of the light intensity.

The CT states are populated by dissociation of the photogenerated singlet exciton and is therefore also a singlet state. However, a change to a triplet state can also occur. Usually, triplet excitons cannot be harvested; they decay in part by slow phosphorescence, and, thus, are lost in terms of photocurrent generation.

Marcus theory predicts that low bandgap polymers would be inherently more prone to geminate (and bimolecular) charge recombination. Moderate band gap polymers have been more successful than low band gap polymers due to reduced charge recombination in these devices.

Charge carrier recombination. The photogenerated free charge carriers finally need to be transported from their site of generation to their respective electrodes. Hopping transport model is used to explain charge transfer in disordered organic semiconductors. This is in contrast to organic crystals, in which band transport also occurs.

Geminate recombination of a freshly generated charge pair (polaron pair) at the heterointerface is monomolecular because two constituents originate from the same precursor state (first order process). In contrast, if two

mobile and independent charges are involved, the bimolecular recombination rate describes this nongeminate electron-hole recombination. It is a second order process.

Nongeminate recombination is a loss mechanism dominates during the drift of free charge carrier to the electrodes. In contrast with geminate recombination, it depends on the light intensity. The recombination partners could either be injected into the organic semiconductor or originate from different successfully dissociated polaron pairs. The classical model to describe bimolecular charge carrier recombination in low-mobility solids is the Langevin recombination. It states that the recombination rate R is determined not by the microscopic recombination mechanism but by slower finding of two oppositely charged carriers, thus mutually attracting one another given they are close enough that the Coulomb energy exceeds the thermal energy [34].

In bulk heterojunction solar cells, recombination of free charges always occurs with the polaron pair as an intermediate state. Thus, free charges do not recombine directly upon meeting one another, but build a bound polaron pair first, which has a finite chance of dissociating again [39].

For free charges in low mobility materials, a nongeminate recombination of the second order (bimolecular) – following Langevin's theory – is usually expected. The Langevin recombination rate is given as

$$R = \gamma(np - n_i^2)\,. \tag{1.2}$$

Here, n is electron concentration, p – hole concentration, n_i – the intrinsic carrier concentration, γ – Langevin recombination prefactor. The recombination process is shown in fig. 1.6.

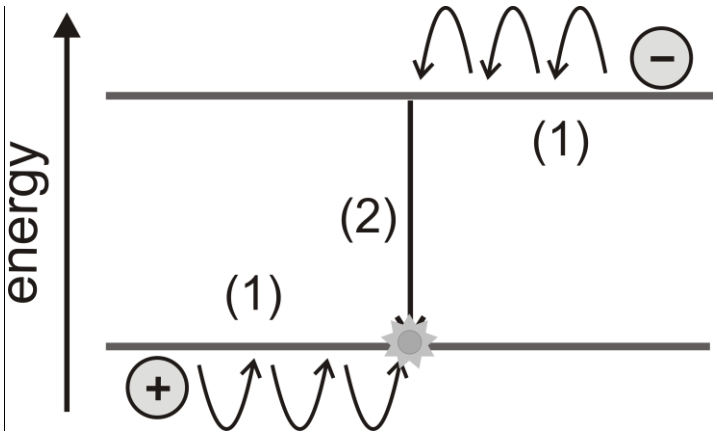

Fig. 1.6. The bimolecular Langevin recombination of electrons and holes [34].

It is assumed that the rate limiting factor for recombination is the finding of the respective recombination partners (1), and not the actual recombination rate (2). Neglecting process (2) as it is faster than (1), the finding of electron and hole depends on the sum of their diffusivities or, considering the Einstein relation, their mobilities [34].

$$\gamma = \frac{q}{\varepsilon_r \varepsilon_0}(\mu_e + \mu_h) \tag{1.3}$$

Where q is the elementary charge, $\varepsilon_r \varepsilon_0$ the effective dielectric constant of the ambipolar semiconductor, μ_e and μ_h the electron and hole mobilities.

In bilayer solar cells, which do not contain a mixed donor-acceptor layer, the occurrence of nongeminate, particularly bimolecular recombination is fortunately unexpected. Once the bound electron-hole pairs have been separated, escaping the chance to recombine geminately, they usually do not meet again due to the device configuration of two separate layers, one electron, one hole conducting, with a planar heterointerface in between. Despite that, bulk heterointerface shows more advantages than planar heterointerface.

Charge carrier exctraction. Free photogenerated charges that do not recombine can finally be extracted from the device in order to yield a photocurrent. The charge extraction process depends strongly on the device

architecture, which determines the steady state carrier concentrations. Another important aspect is surface recombination at the metal-organic interface, which influences the carrier concentration at the interface, and thus the charge extraction.

Several mechanisms are counter-productive towards extracting photocurrent at the electrode interface, they are

- extraction of charges at the opposite polarity electrode (reverse diffusive recombination)
- recombination of charges through defects or impurity states
- formation of an energy barrier due to energy level mismatch of HOMO/LUMO and anode/cathode
- formation of energy barrier due to electrode corrosion or other degradation effects
- exciton quenching

Metal often have poor charge selectivity, allowing both holes and electrons to be extracted at the same electrode, which evidently lowers photocurrent. Interface layers can be added to improve charge selectively and decrease this effect. In fact, all undesired processes at the organic/metal interface may be overcome by using appropriate interface materials.

1.3 Materials used for measurements

1.3.1 Polydihexylsilanes

Polysilanes belong to silicon–organic polymers, which consist of σ-conjugated Si backbone and of organic side groups. The σ–bonding electrons of sp^3 orbitals are considered to be delocalized along the chain axis. Polysilanes show remarkable photoluminescence (PL) in the UV region. Apart from high PL quantum efficiency, high mobility of holes is also noteworthy; thus, these polymers are promising in construction of emitting or transport

layers for electroluminescence devices. In this thesis poly(di-n-hexylsilane) PDHS (Fig. 1.7) was investigated in more detail. Photophysical properties of polysilanes are quite sensitive to the polymer conformation because the electronic states are strongly dominated by the σ-conjugated electrons overlapping along the Si – Si main chain. Absorption and fluorescence spectra of PDHS show thermochromism due to the order – disorder transition of the polymer backbone conformation. The conformation transition is illustrated schematically in Fig. 1.8. An all-*trans* (planar zigzag) conformation has been proposed as an ordered structure of PDHS in the solid state and all-*gauche* as disordered conformation, where hydrogen atoms are not displayed to highlight the conformation of Si-Si and C-C.

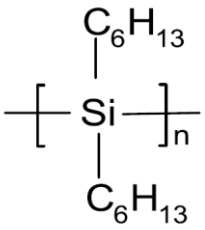

Fig. 1.7. Chemical structure of Poli(di-n-hexylsilane).

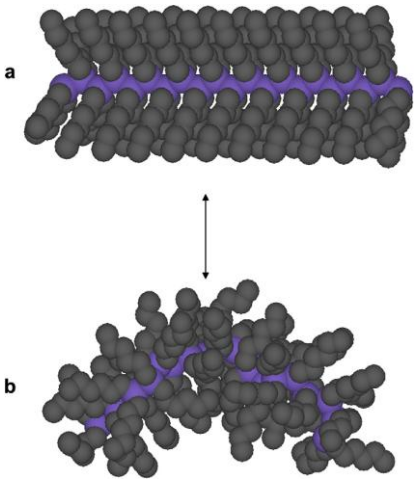

Fig. 1.8. Molecular models of (a) all-*trans* conformation and (b) random coil (all-*gauche*) conformation [40].

All-*trans* conformation has more conjugated bonds than all-*gauche* conformation. That affects fluorescence and absorption spectra of these conformations. The conformation of PDHS is sensitive to the environment. Incorporation of PDHS into nanoporous silica material as a host matrix

influences the fluorescence spectra. Recently, a possibility of the manipulation of properties of nano-sized polysilanes by incorporating them in mesoporous silica matrices such as MCM-41 and SBA-15 has been demonstrated [41, 42]. It should be mentioned that this approach also leads to an essential increase in the durability of a polymer in optoelectronic devices . It was shown that we can control the number of polymer chains entering a nanopore, their conformation and orientation, and their optical properties by changing the diameter of nanopores. The pore size and the chemical structure of the pore surface remarkably influence the fluorescence properties. It has been demonstrated that fluorescence properties of such composite materials are significantly different from the PDHS in solutions due to both polymer-polymer and polymer surface interactions in the nanopores. The polysilane chains near the pore boundaries and in the pore center evidently should have different properties, where the polymer – surface interaction leads to the *gauche* conformation. Polysilane are suitable probes to investigate the guest polymer – host matrix interaction because the photophysical properties of the polysilane remarkably depend on the conformation of the σ-conjugated Si – Si chain [41, 42].

1.1.2 Polyfluorenes

Polyfluorenes are conjugated polymeric materials. Fluorene, a principal segment of polymer structure in polyfluorene derivatives, was isolated from coal tar and discovered by Marcellin Berthelot prior to 1883 [43]. Fluorene, or 9H-fluorene, is a polycyclic aromatic hydrocarbon. Physical properties of the fluorene molecule were recognizably desirable for polymers; as early as in the 1970s researchers began incorporating this moiety into polymers. For instance, because of fluorene's rigid, planar shape a polymer containing fluorene was shown to exhibit enhanced thermo-mechanical stability [44]. However, more promising was to integrate the optoelectronic properties of fluorene into a polymer. This is the only family of conjugated polymers that emit colors

spanning the entire visible range with high efficiency. Other unusual optical and electrical properties, such as thermochromism, are made possible with polyfluorene derivatives [44].

Over the past decade, studies on photophysics of polymers have mainly been focused on homo-polymers such as polyfluorene. Current state-of-the art materials, however, are often co-polymers with four or more chemically different subunits [44]. To increase the thermal and electrical stabilities of polyflourenes, introduction of a spiro linked fluorine has been proven to be successful. The conjugated spiro unit has a large influence on excited state dynamics of polyfluorenes.

In this thesis bibolar poly(spirobifluorene-co-benzothiazole) (PSF-BT) and well known poly(fluorine-co-benzothiadiazole) F8BT fig. 1.9 were explored. The electron rich benzothiadiazole unit gives rise to modified excited state properties with respect to homo-polymers.

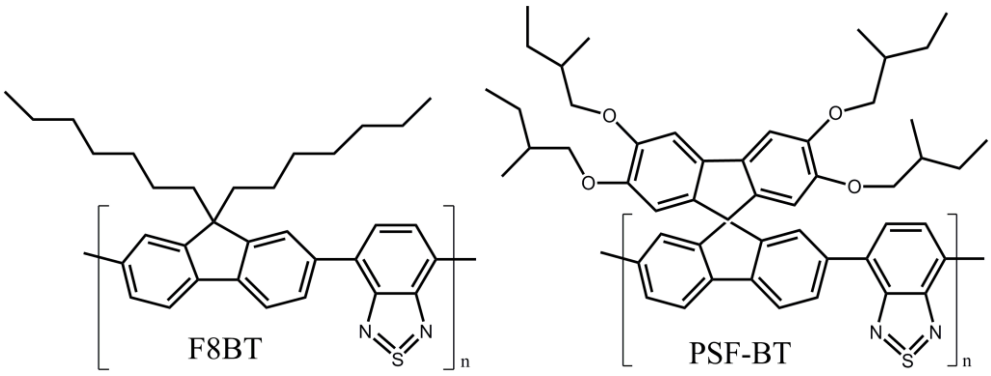

Fig 1.9. Poly(fluorine-co-benzothiadiazole) F8BT and poly(spirobifluorene-co-benzothiazole) PSF-BT.

1.1.3 Merocyanines

In 1860, C. G. Williams named the dye with a brilliant blue shade that he obtained by the reaction of quinoline with amyl iodide and subsequent base treatment as cyanine (cyanos = blue) [45]. However, it was only decades later that the structures of these dyes, including that of Williams cyanine, could be reliably clarified. It was then realized that all of these dyes have one feature in common. They consists of two heterocyclic units, which are connected by an odd number of methane groups $(CH)_n$ (fig. 1.10) The predominantly aromatic heterocyclic donor (D) and acceptor (A) groups are connected by polymethine chains of various lengths. Cyanines can be cationic, anionic or neutral also called merocyanines [46]. They have zviterionic character. The high oscillator strength makes them interesting as light absorbers. Recent investigation showed that they can be suitable as electron donors in bulk heterojunction solar cells. Many types of merocyanines are synthesized at the moment [9, 46–48]. One of them is MD376. MD376 was explored in this thesis because it is stable and easy to synthesize [9]. It was investigated pure or in blends with fullerene and its derivative PCBM (fig. 1.11).

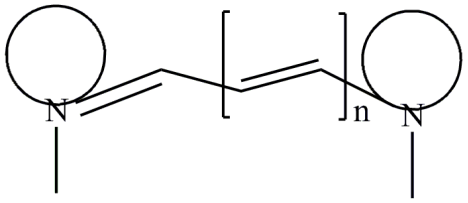

Fig 1.10. Basic structure of cyanines.

1.1.4 Fullerenes

Molecular excitons effectively dissociate into charge pairs in heterojunctions between electron donating and electron accepting compounds (see below). While lots of polymers, oligomers and small molecules can be used as light absorbers and electron donors, in most cases only fullerene or its

derivatives are used as electron acceptors. Owing to their strong electronegativity and high electron mobility, C_{60} derivatives have become standart n-type molecules in OSC devices. Many types of fullerene derivatives are currently synthesized like [6,6]-phenyl-C_{61}-butyric acid methyl ester (PCBM), 1′,1″,4′,4″-tetrahydro di [1,4] methanonaphthaleno [1,2 : 2′ ,3′, 56,60:2″,3″] fullerene-C_{60} (ICBM) and others [49]. Fullerene C_{60} or C_{70} can be used in blends. C_{70} absorbs light more efficiently but C_{60} has better morphology with most electron donors. Fullerene and its derivatives are almost irreplaceable as electron acceptor so far [2].

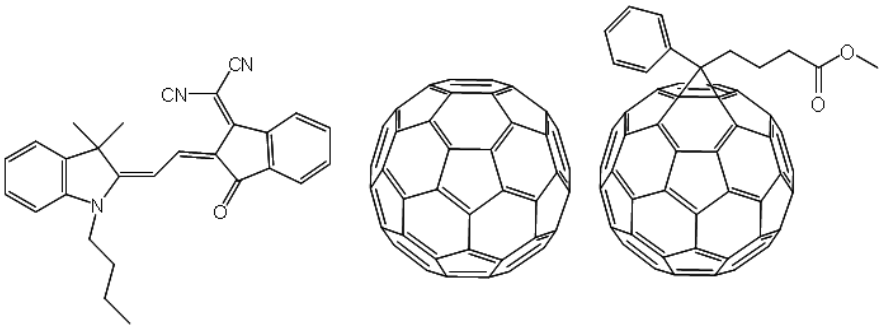

Fig 1.11. Merocyanine MD376 , fullerene and PCBM are shown in this figure.

2 Experimental methods and equipment

2.1 Steady state absorption and fluorescence

Steady-state absorption measurements were done using Spectrophotometer Jasco V-670. Fluorescence spectra of the samples were measured using Edinburgh Instruments Fluorescence spectrometer F900. Lasers EPL-375 and ELP-470 emitting 50 ps pulses at 375 nm and 470 nm and LED EPLED 280 emitting 750 ps pulses at 280 nm with a repetition rate of 20 MHz were used for excitation.

2.2 Time resolved fluorescence

Fluorescence decay kinetics were meassured using multi-dimentional time-correlated single photon counting (TCSPC) method with Edinburgh Instruments Fluorescence spectrometer F900. Initial part of the fluorescence decay dynamics was investigated employing picosecond fluorescence spectrometer based on Hamamatsu streak camera C5680. For the excitation, a femtosecond Yb:KGW oscillator (Pharos, Light Conversion Ltd.) was employed. The oscillator produced 80 fs 1030 nm light pulses at 76 MHz repetition rate, which were frequency tripled to 343 nm (HIRO harmonics generator, Light Conversion Ltd.), attenuated, and focused into ~ 100 μm spot on the sample resulting in about 1 mW/mm^2 average excitation power. The maximum time resolution of the whole system was about 3 ps.

A liquid helium cold finger cryostat (Janis CCS-100/204) has been used for steady state and time resolved fluorescence measurements at various temperatures.

2.3 Transient absorption

Transient absorption investigations were performed by means of conventional broadband femtosecond absorption pump-probe spectroscopy. It is likely the most widely used method of ultrafast spectroscopy. Two light pulses are used for this technique. An intensive pump pulses are used for the excitation of explored sample molecules while probe pulses verify the influence of the pump pulses on the samples absorption. The delay time between pump and probe pulses can be varied mechanically, that gives the ability to record differential absorption of samples at various delay times between pump and probe pulses. In other words, to measure transient absorption decay kinetics.

The used spectrometer was based on an amplified femtosecond Ti:sapphire laser (Quantronix *Integra-C*) generating pulses at 805 nm of approx. 130 fs duration at 1 kHz repetition rate. Pulses of optical parametric generator *TOPAS C* at 500 nm wavelength and second harmonic of laser fundamental wavelength 402,5 nm were used for the excitation of the sample as pump pulse. White light continuum for probing was generated in a 2 mm thick sapphire or CaF_2 plate and used as a probe pulse. The excitation beam was focused into a spot of about 500 μm in diameter, while the diameter of the probe spot was about 300 μm. During the actual transient spectrum measurement, the spectrometer recorded white light supercontinuum spectra with pump light blocked and unblocked. The differential absorption (ΔA) is defined as the negative logarithm of the ratio of transmitted light with and without optical excitation (pump), respectively.

$$\Delta OD(\lambda) = \lg \frac{I_{unpumped}\ (\lambda) - I_{dark\ ,unpumped}\ (\lambda)}{I_{pumped}\ (\lambda) - I_{dark\ ,pumped}\ (\lambda)} \tag{2.1}$$

Since the measured signals are usually of the order of 0.001, the signals in the software are multiplied by a factor of 1000, i.e. expressed in mOD.

Positive signals correspond to induced (excited state) absorption and negative signal are due to absorption bleaching and/or stimulated emission.

2.4 Integral mode photocurrent

In oder to measure photogenerated charge carriers dynamics the capacitor like sample was used. The device used in our investigation is a parallel plate capacitor that is charged by the applied ~100 μs duration voltage and excited by about 130 fs duration light pulses. Charged capacitor is discharged by charge carriers generated by photoexcitation with ultrashort pulses. Voltage dynamics in capacitor corresponds to the photocurrient dynamics.

Integral mode photocurrent measurements were performed by two methods: optical time-resolved electric field-induced second harmonic generation (TREFISH) method [50] on a 1 ps-3 ns time domains and electrically, by oscilloscope using time of flight (TOF) method on a 10 ns-100 μs time domain. These methods will be discussed more detaily.

Time of flight (TOF). TOF is the transient electrical measurement technique that is used to record the charge carrier motion between two electrodes in the sandwich-type device. One of the electrodes is transparent to light. Under applied electric field, a short light pulse illuminating the device is followed by drift of charge carriers towards another electrode. The dynamics of photo-generated charge carriers (photocurrent) can be electrically observed by an oscilloscope.

2.5 TREFISH

The initial part of the integral mode photocurrent was investigated by means of TREFISH method. This method enables measurement of the electric field kinetics with subpicosecond time resolution (Fig. 2.1).

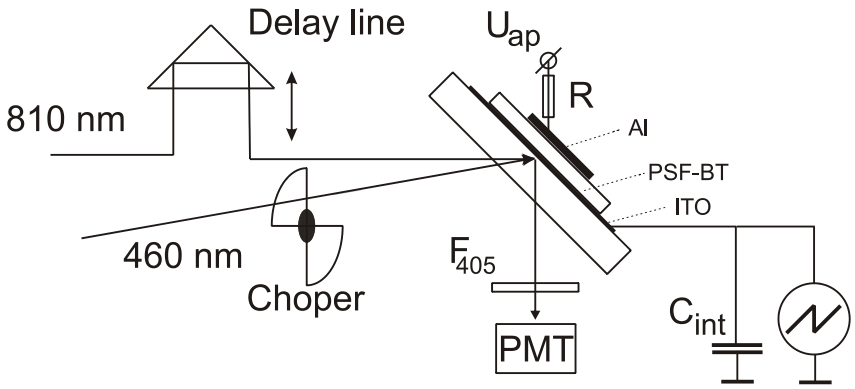

Fig. 2.1. Experimental setup for TREFISH and integral mode TOF measurements [51].

Details on TREFISH method can be found in [50–52]. Briefly, TREFISH method relies on generation of the second optical harmonic (SH) in a sample due to built-in or applied electric field, which breaks the centrosymmetry of the film material and enables generation of SH in amorphous films. Essentially, TREFISH is equivalent to the integral mode photocurrent measurement, which measures the integrated photocurrent not by measuring voltage kinetics on a sample, but by measuring dynamics of the electrical field inside the sample, which is related to the voltage on sample as $V=Ed$, where d is the thickness of the film. Fundamental laser radiation at 810 nm was used to probe electric field according to the intensity of second harmonic at 405 nm. Monitoring the second harmonics intensity in a pump-probe scheme reveals dynamics of the electric field related to the charge density redistribution and motion of the charge carriers.

Upon optical excitation the photocurrent partly discharges the capacitor, reducing the electric field responsible for SH. The time-resolved SH intensity (I_{SH}) caused by optical excitation at different applied voltages. SH is observed with p-polarized probe light only since unlike s-polarized light, it has a nonzero component of the electric field. It is known that I_{SH} is proportional to the square of the electric field and is independed of electric-field polarity in

agreement with expectations. Small electric-field variations ΔE can be estimated from

$$\Delta E = [(\frac{I_{SH}}{I_{SH}^{0}})^{\frac{1}{2}} - 1]E_0 \tag{2.2}$$

where E_0 is the applied field (corrected for the built-in potential caused by differences in work function of the two electrodes), I_{SH} and I^0_{SH} are the SH intensities with and without excitation, respectively.

Two components are responsible for the change of the electric field upon optical excitation: excitons ΔE_{exc} and charge carriers ΔE_{CC}. The electric field change may be expressed by the conductivity current related to charge carriers and displacement current related to excitons as [52]:

$$\Delta E(t) \approx \Delta E_{\mathrm{exc}}(t) + \Delta E_{CC}(t) \approx -n_{\mathrm{exc}}(t)(\Delta\alpha)E_0 / 2\varepsilon\varepsilon_0 - n_{\mathrm{cc}}(t)e\langle l(t)\rangle / \varepsilon\varepsilon_0 \tag{2.3}$$

where $\Delta\alpha$ is the difference between the material polarizabilities in the ground and in the excited states, e is the elementary charge, $n_{\mathrm{exc}}(t)$ and $n_{\mathrm{cc}}(t)$ are the exciton and charge carrier concentrations and $\langle l(t)\rangle$ is the average drift length of generated charge carriers along the electric field. From the electric field dynamics we obtain the charge extracted from the sample q, which is related to the electric field decrease ΔE and voltage decrease ΔV, as: $\Delta V = \Delta E d$, $q = \Delta V C_{sam}$.

More detailed descriptions of the experiment of photo current measurement will be discussed below. The device used in our investigation is a parallel plate capacitor that is charged by the applied 300 μs duration voltage. Sandwich-type sample consisting of the investigated film between two electrodes was equivalent to capacitor with capacitance C_{sam} ~ 3 nF that was slowly charged through load resistor by external voltage source and discharged due to photocurrent created by the excitation pulse. During these investigations, which were performed simultaneously, the samples were excited by about 130 fs duration pulses at 500 nm generated at 1 kHz repetition

rate by means of amplified femtosecond Ti:sapphire laser Quantronix *Integra-C* equipped with optical parametric generator *TOPAS C.* For electrical measurements electrical pulse generator Tektronix AFG3101 and oscilloscope Agilent DSO5054A were used. The sample was connected in serial with a 10 kΩ load resistance and connected to a generator with 50 Ω output resistance. The oscilloscope connected in parallel with the 10 kΩ load resistance measured voltage variations on the sample which were influenced by photocurrent created in sample by its excitation and sample capacitance. The sample capacitor C_{samp} of about 3 nF and the load resistance determined the current integration time, which was of about 30 μs. The measured integrated photocurrents were corrected for the limited integration time.

3 Spectroscopy of Nano-Sized Polysilanes Confined by Different Structures of Silica

σ-conjugated luminescing polymers are promising materials for various photonic applications, such as active layers of light-emitting diodes [20, 53, 54], luminescent sensors and bioprobes [55–57]. Photoluminescence (PL) quantum yield, which desirably should be close to 100%, is one of the major parameters determining their usage perspectives. Polymers usually have to be used in a solid state as thin films where macromolecules tend to form aggregates. It is known that aggregation of the organic polymers often leads to partial or even complete quenching of their PL. Simultaneously a decrease in duration of the PL lifetime is observed. This effect has limited the scope of technological applications of the polymers. Therefore substantial challenge is to discover and explore the mechanisms that form new functional properties of polymers when aggregation plays a constructive, rather than destructive role. Several conceptions have been proposed to produce polymers with aggregation-enhanced emission (AEE): conformational planarization, J-aggregate formation, twisted intramolecular charge transfer and restriction of the intramolecular rotation of the individual parts of the macromolecules [58–61]. Theoretical and experimental research of a number of authors [61, 62] showed that restriction of the intramolecular motion of macromolecules blocking the nonradiative path and activating the radiative decay is the most important mechanism of the AEE effect. As a result, polymers with AEE were synthesized by attaching propeller-like molecular structures of active hexaphenylsilanes or tetraphenylethenes to the polymer backbones [63, 64].

Temperature dependences of optical properties of four novel nanocomposite films based on poly(di-n-hexylsilane) (PDHS) incorporated into an inorganic matrix having different structure and neat PDHS film were explored in this chapter.

3.1 Experimental

Porous SiO_2 and TiO_2 films were obtained by sol-gel template synthesis [65]. Precursors of tetraethoxy silane (TEOS) or tetraisopropoxy titane (TIPT) were subjected to pre-hydrolysis in water - ethanol - 1M HCl solution at pH = 2. Solution of template agent triblock copolymer poly(ethylene oxide)–poly(propylene oxide) – poly(ethylene oxide) – $EO_{20}PO_{70}EO_{20}$ (Pluronic P123, Adrich) or cetyltrimethylammonium bromide (CTAB) in ethanol was added, and reaction mixture was stirred vigorously during 3 hours. Porous films were prepared from the precursor by "dip-coating" technique on glass or quartz substrates with the constant rate of 9 cm/min. Dry films were heat- treated in a muffle furnace with a programmable heating regime (at a rate of 1.5 °C/min up to 350 °C and 3 hours kept at 350 °C). The surface area of the films was calculated from the adsorption-desorption isotherms of hexane vapors and are 658 and 816 m^2/g for the films of SiO_2 and TiO_2 respectively. The average pore diameter was calculated from the spectra of small-angle X-ray scattering being of about 10 nm. According to the electron-microscopic measurements, the films had a hexagonal pore structure (Fig. 3.1).

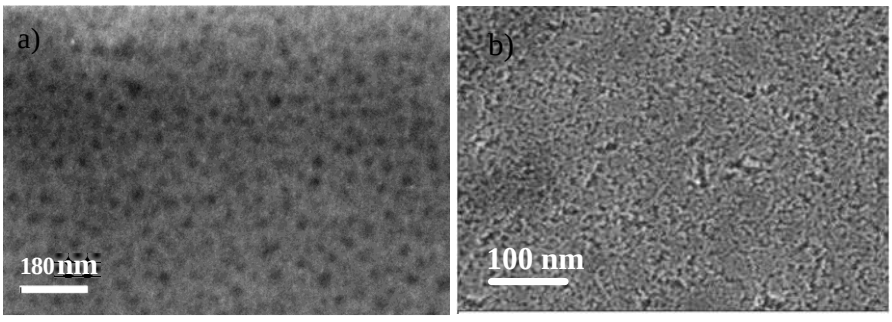

Fig. 3.1. Electron microscope image of the SiO_2 (a) and TiO_2 (b) sol-gel films after heat treatment at 623 K. The average pore diameter is of 10 nm.

To obtain PDHS/SiO_2 or PDHS/TiO_2 nanocomposites, porous SiO_2 or TiO_2 films previously annealed at 350 C were placed in toluene solutions (M_w = 53 600) with different PDHS concentrations (10^{-4}, 10^{-3} 10^{-2}, 4.3×10^{-2} mol/l) and were kept until reaching the adsorption equilibrium after which the absorption spectrum did not change. Then the samples were washed by toluene to remove the residual polymer from the surface and dried to remove the solvent. It should be noted, that the absorption bands of nanocomposites remained quite intense, even after washing of films in toluene up to 150 minutes [66]. It indicates that the bonding strength of the polymer chains with the matrix is strong enough to prevent desorption and allows us to suggest that polymer chains are dominantly located in the pores. A simple dispersion interaction may be sufficient to keep the polymer adsorption on the surface of the pores. This is also evidenced by the fact that the polymer film, which is located on the outer surface of the porous films, is washed with toluene within 15 minutes. However we cannot also exclude that fractions of long polymer chains remain outside of the pores. Availability of the polymer in the pores and the degree of the pore filling was determined from the absorption spectra of nanocomposites [66]. It should be noted, that the porous films of silicon and titanium dioxides are transparent in the region of absorption of the polymer film.

To get another kind of the samples, we will call them as PDHS/nanosized SiO_2 nanocomposites, the SiO_2 matrix consisting of disperse nanosized particles of about 2 nm in diameter was placed in the 10^{-3} mol/l polymer solution in toluene and slowly stirred in dark for several hours. Then this solution was deposited on the glass substrate by spin coating.

Pure polymer films were also prepared for comparison by applying PDHS solution in toluene with concentration of 4.3×10^{-2} mol/l on the surface of porous films or on the glass substrates and drying without further washing.

Photoluminescence (PL) spectra of the samples were measured using Edinburgh Instruments Fluorescence spectrometer F900. The sample excitation

was performed by 280 nm from light emitted diode (LED). Multi-dimentional time-correlated single photon counting (TCSPC) method was used for lifetime measurements. Pulse duration was 750 ps. Repetition rate of LED pulses was of 20 kHz. A liquid helium cold finger cryostat (Janis CCS-100/204) has been used for temperature dependent measurements in 15-300 K range in a slow cooling regime. Fluorescence relaxation lifetimes measured by TCSPC were found by approximation of emission kinetics with exponential functions together with the deconvolution of the apparatus function. Deconvolution procedure allowed us to determine shorter relaxation times than the excitation pulse duration and PMT response.

3.2 Absorption and fluorescence excitation spectra

The absorption spectrum of PDHS film on quartz that was prepared using a toluene solution (4.3×10^{-2} M) consists at room temperature of two bands with maxima at 313 and 365 nm (Fig. 3.2, curve 1). The band at 365 is much stronger than that at 313. The absorption spectrum of PDHS film formed on the surface of SiO_2 films (regardless of the film porosity) has practically the same spectrum as that on quartz. The absorption spectrum of PDHS in toluene ($c = 10^{-7}$ M) consists of one band with a maximum at 317 nm (Fig. 3.2, curve 2). The starting mesoporous SiO_2–CTAB and SiO_2–Pluronic films without PDHS have an absorption band edge in the short-wavelength region (<200 nm) and do not contribute to absorption in the studied range [67].

Optical spectra of the nanocomposite films were studied over a broad range of polymer concentrations in toluene solution (4.3×10^{-2}, 10^{-2}, 10^{-3}, and 10^{-4} M) and sample temperatures (15–310 K). The optimal adsorption time after which the absorption spectrum did not change was found for each concentration. Absorption spectra of the nanocomposites differed considerably from those of the polymer films. The long-wavelength band became stronger as the solution concentration of the polymer increased. The absorption

spectrum of the PDHS/SiO_2 Pluronic nanocomposite (c = 10^{-4} M) exhibited two strong bands with maxima at 317 and 367 nm (Fig. 3.2, curve 3). It can be seen that these bands had frequencies similar to those in spectra of PDHS CTAB nanocomposites (curve 4). However, the absorption spectra of the nanocomposites differed in that the short-wavelength band was stronger than the long-wavelength one. Treatment of this composite with toluene caused the spectrum to weaken, which was consistent with partial dissolution and removal of the excess of polymer from the surface.

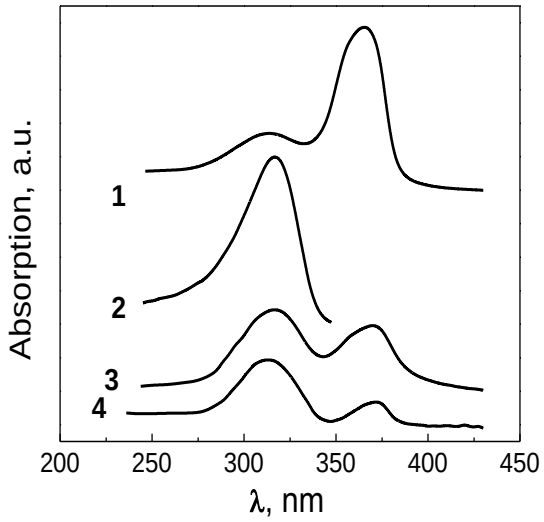

Fig. 3.2. Absorption spectra at room temperature: PDHS polymer film (1), toluene solution of PDHS polymer (10^{-7} M) (2); nanocomposite PDHS/SiO_2 Pluronic (3) and PDHS/SiO_2 CTAB (4) films.

The PL spectrum of this nanocomposite at room temperature contained a strong band with λ_{max} = 380 nm and a weak band with λ_{max} = 342 nm (Fig. 3.3, curve 1).

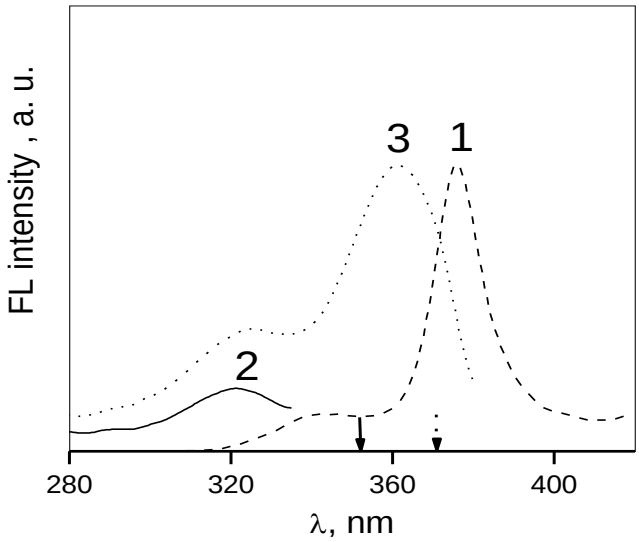

Fig. 3.3. Photoluminescence spectrum of PDHS/SiO_2 Pluronic nanocomposite at 15 K (10^{-4} M) (1) and photoluminescence excitation spectrum for λ_{rec} = 353 (2) and 369 nm (3).

The short-wavelength band appeared only if the solution concentration of the polymer was decreased. Fig. 3.3 also shows the excitation spectrum of this nanocomposite at room temperature. It can be seen that recording the excitation spectrum using the PL band at 345 nm gives a band with λ_{max} = 320 nm. Recording the spectrum using the PL band at 380 nm gave an additional long-wavelength band with λ_{max} = 360 nm. The absorption spectrum of the PDHS/SiO_2 CTAB nanocomposite (c = 10^{-4} M) exhibits a broad strong band with λ_{max} = 317 nm and a weaker band at 367 nm (Fig. 3.2, curve 4). The long-wavelength band becomes dominant with respect to intensity as the concentration increases. Fig. 3.4 shows the temperature dependence of the PDHS/SiO_2 CTAB composite absorption spectrum in the range 293–315 K. It can be seen that the long-wavelength band becomes

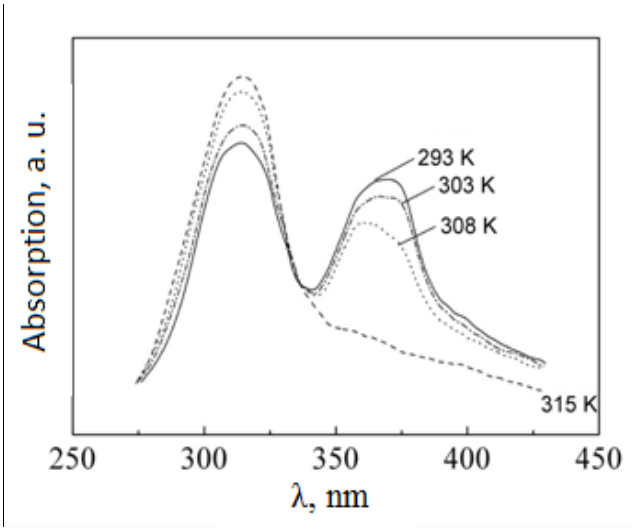

Fig. 3.4. Change of absorption spectrum of PDHS/SiO_2 CTAB composite with temperature increasing from 293 to 315 K.

weaker as the temperature increases whereas the short-wavelength band strengthens. Only the short-wavelength band remains at 315 K. The PL and PL excitation spectra of these nanocomposites are similar to the corresponding spectra of the PDHS/SiO_2 Pluronic nanocomposites (Fig. 3.4).

PDHS is known to be a thermochromic polymer. Its electronic transition depends considerably on the conformation of the polymer chain. The polymeric chains of this polymer at room temperature are found mainly in the aggregates, to which the strong absorption band with a maximum at 365 nm corresponds. At low temperature a small fraction of the polymeric chain segments are found in the *gauche*-conformation (more disordered conformation) (Fig. 3.2, curve 1). The weak broad band with a maximum at 313 nm corresponds to electronic transitions in the polymeric chain segments with the *gauche*-conformation. The polymer in toluene solution has chains in the *gauche*-conformation. This conformation corresponds to the band at 317 nm (Fig. 3.2, curve 2). The porous films are transparent in the region where the polymer films absorb. Fig. 3.2 shows that the ratio of intensities of the absorption spectral bands of PDHS/SiO_2 nanocomposites depends on the polymer concentration and differs from their ratio in the spectrum of the films.

These bands remain rather strong even if the films are stored in toluene for a long time. This indicates that the polymeric chains are located in the pores. The polymer film that is located on the outer surface of the porous SiO_2 film is rinsed away by toluene in 15 min. The temperature dependence of the nanocomposite PL confirms that the polymeric chains are located in the pores. Spectra of nanocomposite films were analyzed by comparing them with those of solutions, polymer films, and previously prepared composites of PDHS/SBA-15 (pore diameter 10 nm) as powders. The conformation of PDHS polymer chains in the limited pore volume of mesoporous SBA-15 silica is known to differ substantially from that of polymer films and solutions. It was proved that three spatially independent polymer centers that correspond to isolated polymeric chains in the *gauche*- and *trans*-conformations and their aggregates are present in this instance [42]. Bands at 320, 345, and 357 nm and at 337, 355, and 369 nm at T = 5 K in the PL excitation and PL spectra, respectively, correspond to these centers. Only two bands with λ_{max} = 345 and 375 nm that are characteristic of polymeric chains in the *gauche*-conformation and the aggregates are observed in the PL spectrum at room temperature as a result of a thermochromic transition. The present studies showed that the same bands and, therefore, the same conformations of the polymeric chains, appeared in the optical spectra of PDHS/SiO_2 nanocomposite films. However, the appearance of these conformations and their percent contribution changed (Fig. 3.3). Apparently the difference was due to the fact that, as shown earlier [65, 67], mesoporous SBA-15 silica (synthesized using the same template, Pluronic P123, but without depositing it onto a substrate) has a much higher degree of ordering. In other words, the porous structure of the thin films deposited onto the substrate was less ordered than the pure material because of the strong influence of the substrate that destroys the ordered structure during drying and heat-treatment of the films [65]. The fact that on one hand the pores of the silica film are closed by the substrate may create additional steric hindrance to penetration into the pore of the long PDHS polymer chain (polymer chain length ~50 nm, which is comparable with the pore depth). In

this instance the ends of the polymeric chains that are outside the pores can form aggregates. The interaction of separate polymeric chain segments can lead to their self-organization and orientation. Therefore, it can be assumed that the oriented segments forming aggregates have the *trans*-conformation and only a small fraction of the polymeric chain segments have the *gauche*-conformation. If our assumption is correct, then a thermochromic transition should be observed for the long-wavelength absorption band in the spectrum of PDHS/SiO_2 CTAB. This was confirmed experimentally as the sample temperature was increased from 293 to 315 K. In fact, the absorption band with a maximum at 365 nm became weaker whereas that at 317 became stronger as the temperature rose. Only the short-wavelength band was observed in the spectrum at 315 K (Fig. 3.4).

The fact that the pores of the film are closed on the one side by the substrate can create additional steric hindrance to penetrate of the long polymer chain into the pore (the length of the polymer chain of about 50 nm, which is comparable with the pores depth). In this case, the ends of the polymer chains leaving from the neighboring pores can form aggregates due to van der Waals interactions between them.

3.3 Fluorescence spectra

Temperature dependence of fluorescence spectra of nanocomposites. FL spectra (T=15 K, k_{ex}=280 nm) of the investigated nanocomposites on the base of PDHS incorporated in inorganic matrices with different nanoscale morphologies are presented in Fig. 3.5. The inset shows the PDHS structural formula and the FL spectrum of PDHS/SBA-15 composite (pore diameter of 10 nm). The FL spectrum of PDHS/SBA-15 composite at 10 K achieved by the

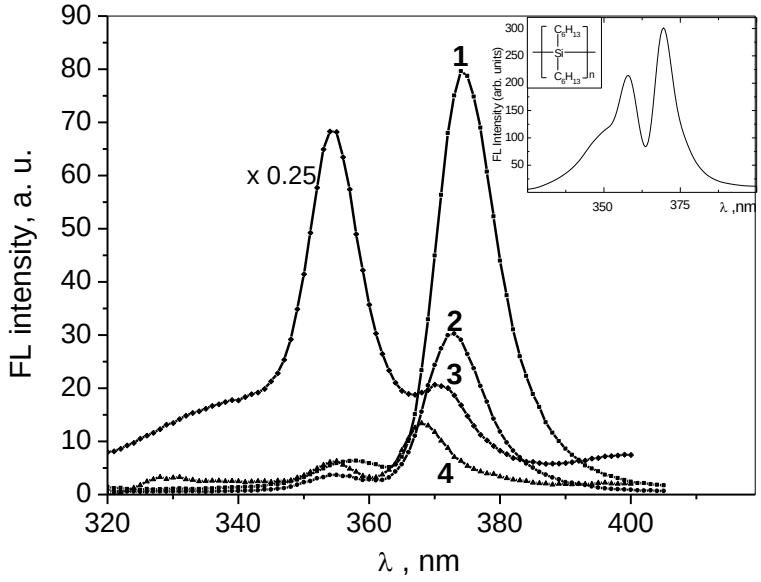

Fig. 3.5. Fluorescence spectra at 15 K of PDHS incorporated in: SiO_2 porous film (1), TiO2 porous film (2), photonic crystal (3), and silica gel (4). The inset shows the structural formula of PDHS and the FL spectrum of PDHS/CBA-15 composite at 10 K [42].

slow cooling consists of two bands at 355 and 369 nm attributed to the polymer chains in the trans-conformation and their aggregates, respectively [42]. A shoulder below 350 nm is related to the gauche-conformation. We also observe three bands in the FL spectra of novel composites which can be also attributed, by comparison with PDHS/SBA-15 spectra, to the trans- or gauche-conformation and aggregate states. The relative intensities of the FL bands of new composites and their maxima positions are significantly redistributed. The four new samples have approximately the same polymer concentration, but their FL intensities are clearly different due to different influences of different inorganic matrices on PDHS conformations. The trans-conformation band has the highest relative intensity in the PDHS/Phot.Cryst spectrum. Despite the fact that the pore dimensions in the photonic crystal are relatively large (of about 70 nm), the polymer chains localized in these pores have basically the trans-conformation. This is evidently related to the strong orientation of the polymer

chains along the pore walls formed by the photonic crystal. PDHS/SiO_2 and PDHS/TiO_2 films reveal the highest relative intensity of the aggregate band. It is also worth noting that the FL spectrum of a PDHS/SiO_2 film is much more intense than that of a PDHS/TiO_2 film. According to our estimation, the length of the pores in SiO_2 and TiO_2 films are of about 100 nm. It can be assumed that, in this case, the polymer chain tags, which remain out of the pores, could form aggregates. The FL spectrum of the PDHS/Phot.Cryst is more intense than that of other nanocomposites. The different structures of photonic crystal and other porous films evidently have a strong influence on the formation of different polymer chain conformations. The fact that the FL spectrum of PDHS incorporated in SiO_2 gel is similar to that of a PDHS/ SiO_2 porous film allows us to conclude that polymer chains are located between long chains formed by the association of nano-sized SiO_2 particles [68]. The PDHS polymer chains in a neat film have, in general, the trans-conformation at low temperatures and the gauche-conformation at room temperature [69]. It is known that the FL spectrum of PDHS/SBA-15 composite at 290K contains two bands at 343 nm and 380 nm attributed to polymer chains in the gauche-conformation and aggregates, respectively [42].

Fig. 3.6 shows the temperature dependence of the fluorescence spectra of the PDHS nanocomposites in the temperature range (15–330) K. The most dramatic modifications of spectra are observed in the interval 200–290 K. As the temperature increases, the trans-conformation bands are replaced by the gauche-conformation ones, while the temperature dependences of the intensities of aggregate bands are very different for different samples. The trans-conformation and aggregate FL bands shift clearly to the long-wave side, as the temperature increases. The temperature-induced spectral modifications below 290K are reversible. The samples can be cooled down and heated up several times, and the spectra remain almost the same at any given temperature. The thermochromic trans-gauche transition for a confined isolated polymer chain takes place at 265 K. It is essentially higher (by 42 K) than the transition temperature of the PDHS polymer in solutions [70]. The FL spectra

of composites were analyzed by approximating them by several Gaussian bands. Three parameters were obtained for each band: the wave number, width, and amplitude. Fig. 3.7 shows the temperature dependence of the integral intensities of different FL bands. As it was already mentioned, the intensity of the

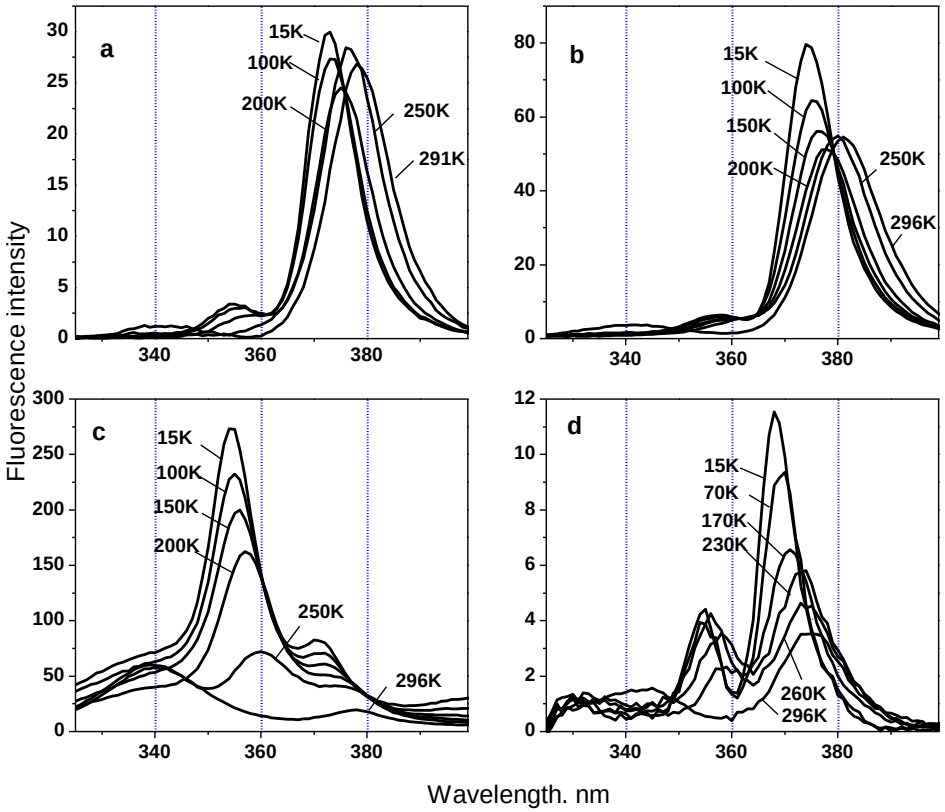

Fig. 3.6. Temperature dependence of fluorescence spectra of PDHS incorporated in: porous TiO_2 (a) and SiO_2 (b) films, photonic crystal (c), and SiO_2 gel (d).

trans-conformation FL band in all samples monotonically decreases with increase in the temperature. The gauche-conformation band intensities in a photonic crystal and SiO_2 gel slightly decrease, as the temperature increases from 15 to 250 K, and then strongly increases, when the trans-gauche transformation takes place. The gauche-conformation bands in porous SiO_2 and TiO_2 films appear only above the trans-gauche transformation temperature. The presence of the gauche fluorescence band in the photonic crystal and SiO_2

gel at low temperatures is the indication that polymer chains in these matrices have a less freedom of conformational motions and cannot form the more ordered trans-conformation. This is in contrast to polymers in porous films, where the gauche FL band is completely absent at low temperatures. The aggregate FL intensities in the photonic crystal and silica gel gradually decrease with increase in the temperature, whereas the temperature dependences are more complex in porous films: the FL intensity gradually decreases with increase in the temperature below the trans-gauche transition, while, at higher temperatures, it increases up to 310 K, when the aggregates are thermally destroyed. The increase in FL is evidently caused by the formation of trans-conformation chains which are more ordered and tend to form aggregate states. This is not the case in the photonic crystal and SiO_2 gel, where the formation of trans-conformation chains does not lead to an increase in the aggregate FL. This observation is in line with the conclusion that polymer chains in these matrices have a less freedom of conformational motions: trans-conformation polymer chains cannot rearrange and form aggregate states. The analysis of the FL spectra of composites shows that the intensity and the width of the FL bands of these composites have a weak temperature dependence in the range 15–200 K, which is opposite to a strong broadening, shift, and drastic decrease of the intensity of the FL band observed for the PDHS film [71].

Relative intensities of the PDHS/SiO_2 and PDHS/TiO_2 composite fluorescence deserve additional discussion. Although we cannot accurately compare them because of possibly slightly different polymer concentrations, however three times difference allows us to conclude that fluorescence of PDHS/TiO_2 sample is most probably lower, but not very significantly. TiO_2 is

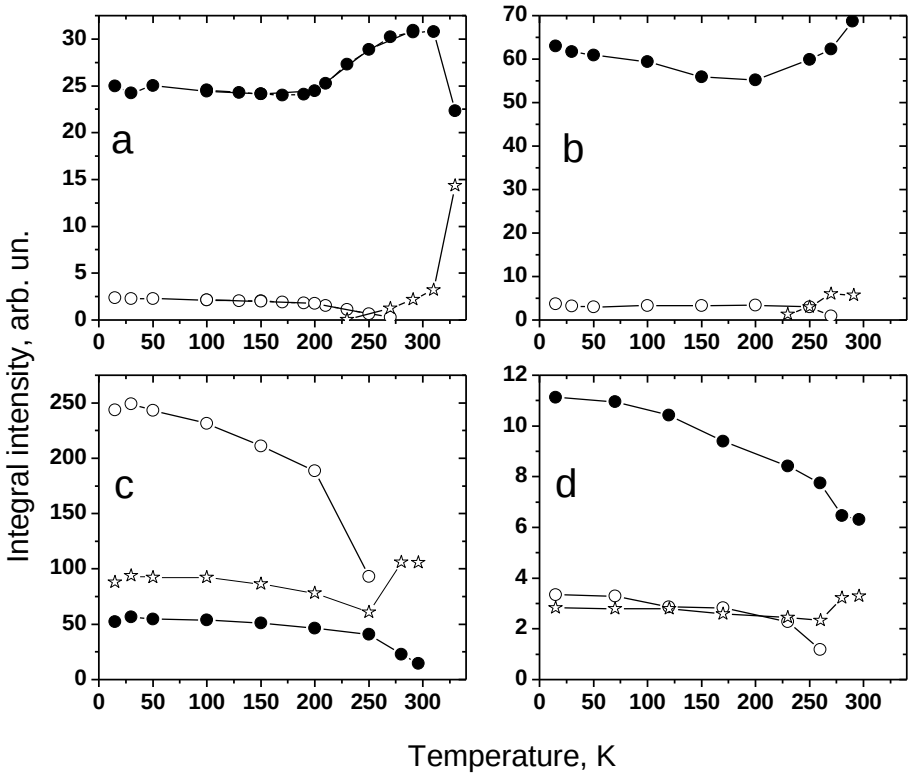

Fig. 3.7. Integrated intensities of the trans-conformation (open circles), gauche-conformation (open stars), and aggregates (solid circles) fluorescence bands of PDHS in TiO_2 porous film (a), SiO_2 porous film (b), photonic crystal (c), and SiO_2 gel (d).

a electron acceptor, and is expected to strongly quench polymer fluorescence by electron transfer from photo-excited polymer macromolecules to the electron-acceptor centers, namely coordinative unsaturated titanium ions and oxygen vacancies [72, 73]. Therefore relatively weak fluorescence quenching remains not completely clear. One of the possible explanations is that the polymer chains touch walls of the pores only by their long hexyl substitutients, keeping relatively large distances between polymer backbone and TiO_2, and thus preventing fast electron transfer. Another possibility is that the ends of the polymer chains sticking out of the pores are responsible for the PDHS/TiO_2 composite fluorescence. The later explanation is less likely, because fluorescence spectra of PDHS/TiO_2 and PDHS/SiO_2 composites are very similar. While polymer chains inside and outside pores are expected to have

different spectra. Therefore composite spectra are also expected to be different if only polymers chain segments located outside pores are responsible for the PDHS/TiO_2 film fluorescence, while fluorescence of PDHS/SiO_2 film originates both from segments inside and outside pores.

The temperature dependences for the PDHS/SiO_2 and PDHS/TiO_2 films are significantly different from those for the PDHS/nanosized SiO_2 composite and for the pure polymer film: intensity of the aggregate band of the PDHS/SiO_2 and PDHS/TiO_2 films increases with temperature, while PL intensity drops down twice at room temperature in the case of PDHS/nanosized SiO_2 composite and pure PDHS film.

Similar temperature independent fluorescence relaxation has been determined for PDHS/SBA-15 composite powder [41] and attributed to the weak exciton diffusion. The same conclusion is evidently also valid for the composite films. Polymer chains located in different film pores are separated from each other, preventing exciton transfer between them. Even if the composite film fluorescence partly originates from the polymer chains sticking out of the pores, the density of such chains is apparently too low to create sufficiently dense network for efficient exciton migration. In contrast, polymer chains in pure PDHS film and in PDHS/nanosized SiO_2 composite are closely packed, enabling efficient and temperature dependent exciton migration and consequently quenching by some impurities, defects or other quenching centers present in the polymer.

The photoluminescence decay kinetics of the investigated PDHS samples are in good agreement with the above described temperature dependences of the fluorescence intensity. Fig. 3.8 shows an example of the fluorescence relaxation traces measured for the PDHS/SiO_2 film at 30 K and at room temperature.

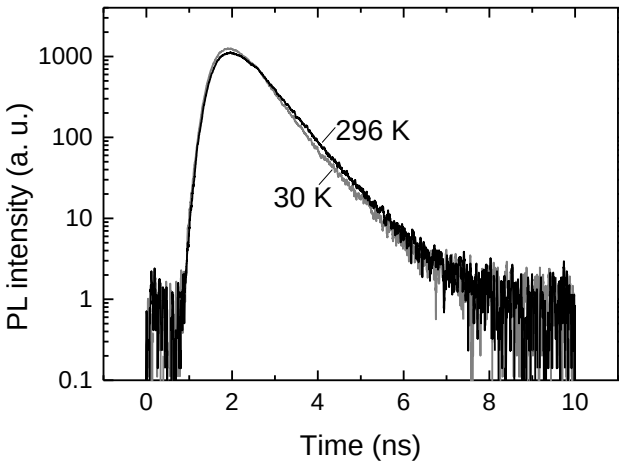

Fig. 3.8. PDHS/SiO_2 fluorescence decay kinetics measured at the maximum of aggregate band at 30 K (374 nm) and 296 K (380 nm).

Fig. 3.9 presents the temperature dependences of the aggregate fluorescence band peak positions and the band widths.

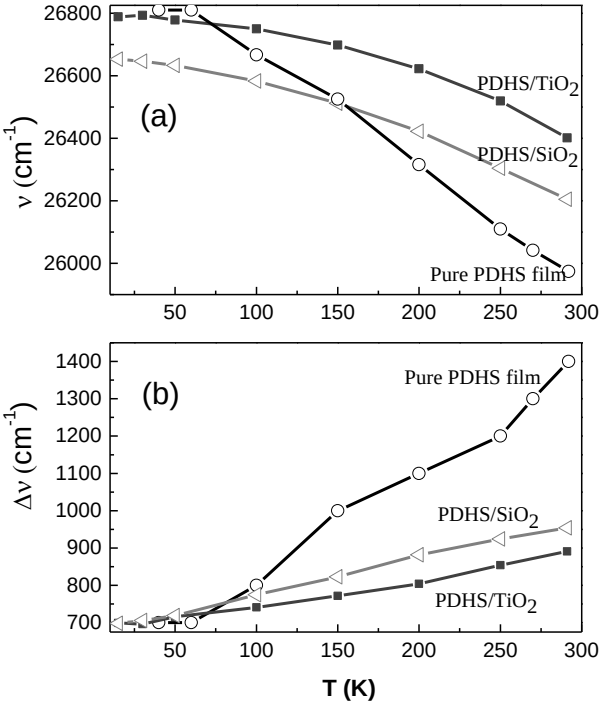

Fig. 3.9. The temperature dependence of the aggregate fluorescence band positions (a) and half-widths (b) of different PDHS samples.

Both these dependences are significantly weaker for the nanocomposite films than for the neat PDHS film. It supports the conclusion that the exciton diffusion is much less efficient in the nanocomposite films. Excitons localize on the low energy sites in the neat film causing the relatively strong bathochromic fluorescence band shift and the band broadening with temperature. It should be also noted, that the fluorescence lifetimes of nanocomposite films are about 1,5-2 times shorter than in SBA-15 matrix. It suggests that the polymer chains in nanocomposite films are less stabilized and isolated from quenching centers.

3.4 Fluorescence relaxation

The FL relaxation kinetics of all composites were measured in the temperature range 30–296 K. The FL kinetics was approximated by a biexponential relaxation function with the deconvolution of an apparatus function. The deconvolution procedure allowed us to determine shorter relaxation times than the excitation pulse duration. In addition to the main relaxation component with a subnanosecond lifetime, the kinetics contains a weak component with the lifetime of several nanoseconds. This component is probably caused by some impurities present in nanocomposites. Therefore, we did not analyze it in detail. Table 3.1 presents the lifetimes and amplitudes of the subnanosecond relaxation component. The FL lifetimes only weakly depend on the sample. Thus, we conclude that different FL intensities of different FL bands are caused by different concentrations of different species present in different samples rather than by their excited state relaxation. The aggregate fluorescence has the longest lifetime. Moreover, the lifetime depends more significantly on the sample and the temperature.

Table 3.1. Fluorescence lifetimes (s) and amplitudes (A) of the subnanosecond decay component.

		Conformation					
		Gauche		Trans		Aggregate	
PDHS composites	T, K	τ, ps	A	τ, ps	A	τ, ps	A
PDHS in SiO_2 gel	30	-	-	170	94	380	98
	296	200	80	-	-	280	98
PDHS in Ph. Cryst.	30	-	-	160	98	300	93
	296	120	97	-	-	420	95
PDHS in SiO_2 nanopores	30	-	-	150	98	470	100
	291	120	94	-	-	550	100
PDHS in TiO_2 nanopores	30	-	-	120	98	330	100
	291	120	97	-	-	390	100

The FL lifetimes were analyzed in more details for PDHS in the photonic crystal. Fig. 3.10 shows the temperature dependence of the FL lifetimes of all FL bands. The trans-conformation lifetime is independent of the temperature, the gauche-conformation lifetime decreases above the trans-gauche transition, while the aggregate lifetime increases surprisingly above the transition temperature. This is in contrast with about a twofold decrease of the aggregate FL lifetime, as observed in the neat polymer film and the solution[71]. We stress that the FL lifetimes of the aggregate states of PDHS confined in nanopores were found basically to be independent on the temperature within the experimental accuracy in the range 30–300K (Table 3.1). This implies the constant FL quantum yield and consequently, the temperature-independent nonradiative

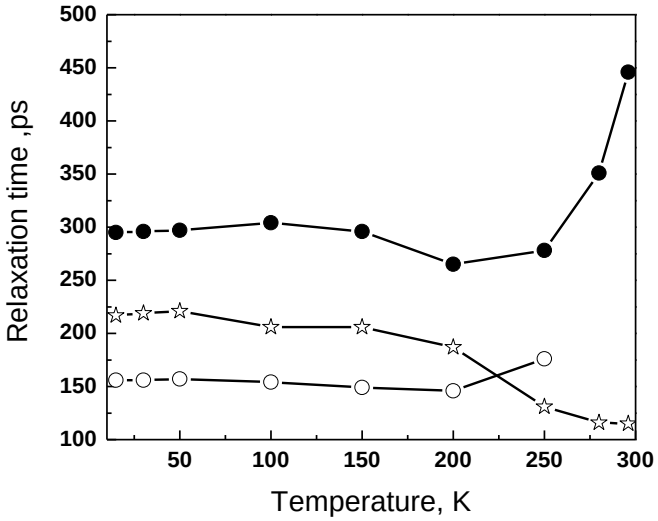

Fig. 3.10. Fluorescence lifetimes of PDHS/Phot.cryst measured for the trans-conformation and aggregates; trans-conformation (open circles), gauche-conformation (open stars), and aggregates (solid circles).

decay. This finding indicates the strong suppression of nonradiative decay channels and the absence of the thermally activated FL quenching of polysilanes embedded in nanopores, which contradicts the results obtained for polysilane films and solutions [71]. The effect is evidently caused by the reduced exciton migration and, thus, by the suppressed nonradiative relaxation due to the strong exciton localization in low-dimensional structures. The same conclusion is evidently valid for other PDHS nanostructures. The weak temperature-enhanced nonradiative relaxation is favorable for nano-sized polysilane-based optoelectronic devices such as OLEDs.

3.5 Concluding remarks

Confomational states of PDHS polymer chains in composite materials strongly depend on the host material. The trans-conformation band is more intense in the spectrum of PDHS in the photonic crystal, while the aggregate

band is more intense in the spectrum of PDHS in porous films. The excited state lifetimes of aggregates for these composites weakly depend on the inorganic matrix and the temperature. This fact indicates the strong suppression of nonradiative decay channels and the absence of the thermally activated FL quenching in nano-sized PDHS. This effect is most probably caused by the reduced exciton migration and, thus, by the suppressed nonradiative relaxation due to the strong exciton localization in a low-dimensional structure. Weak temperature dependences of the PDHS fluorescence intensities, lifetimes, band positions, and bandwidths of nanocomposite films in comparison with those of the neat PDHS film indicate that the exciton diffusion is much less efficient in composite films than in the neat film, and consequently fluorescence quenching by some quenching centers present in polymer is less efficient.

4 Exciton diffusion, annihilation and their role in the charge carrier generation in fluorene based copolymers

Applications of conjugated polymers in some optoelectronic devices, such as in optical amplifiers and lasers [7], or in all-optical switching [74] require high intensity laser illumination necessary to create high exciton density, or significantly modulate optical parameters of the materials. High excitation intensity often causes appearance of nonlinear processes. Exciton-exciton annihilation is probably the most common of them. The annihilation causes a fast nonradiative exciton decay, local material heating, and in some cases generation of charge carriers. All these processes may significantly influence operation of the devices. On the other hand, exciton-exction annihilation may provide useful information about some other processes and properties of the investigated materials like exciton diffusion coefficient which is important parameter in organic solar cells. Carrier photogeneration is one of such processes, very important for application of organic materials in photovoltaic devices and still badly understood. Efficient carrier photogeneration in many conjugated polymers takes place from high excited states [75–77]. At high excitation intensity high excited states may be populated by sequential excitation or by exciton-exciton annihilation. This plays a role even with excitation of low photon energy light and, thus, these processes increase the carrier photogeneration efficiency [76, 78, 79]. The annihilation rate and its kinetics depend on many material parameters and experimental conditions: absorption and fluorescence spectra, material morphology, disorder, temperature, etc.

Here we investigate and compare exciton-exciton annihilation and its role in the charge carrier generation in two fluorene based conjugated polymers F8BT and PSF-BT. Fluorene based conjugated polymers have recently attracted much attention as promising organic materials for photoelectronic applications.

PSF-BT blends (bulk heterojunction) with PCBM were also explored. Bulk heterojunction (BHJ) architecture has remained a state of the art concept for organic solar cells for two decades already [80]. This concept was pushed forward by introducing conjugated polymers as absorbers in organic solar cells [37, 81]. A BHJ is obtained by mixing organic dye or polymer functioning as an electron donor with electron acceptor having significantly lower LUMO level. Due to strong electron accepting properties and solubility in organic solvents, fullerene derivative PCBM is the most common acceptor material. Excitons created by absorption of light in a polymer effectively dissociate into charge pairs at the polymer/PCBM junction. Favorable alignment of LUMO levels drives electron transfer from polymer to PCBM, thus creating electron-hole pairs. Final separation of the charge pairs beyond mutual Coulomb attraction enables high yield of free charge carrier generation necessary for efficient solar cells. Charge generation in blends is by orders of magnitude more efficient [82–84] in comparison with neat materials [85, 86] leading to record efficiencies of solar cells up to about 10% [33, 86–90]. Further improvement of solar cell performance requires optimization of all processes limiting light harvesting, generation and extraction of charge carriers. Until recently, research on optical charge generation has mainly been focused on simple homopolymer donors, polythiophene being the dominant example. The need for materials with more effective charge separation and simultaneously lower band gap to harvest more sunlight stimulates research directed towards more complex materials. Organic compounds composed of molecular fragments with electron donating and accepting properties, where partial intramolecular charge separation takes place in excited state may be advantageous. This intramolecular donor-acceptor (DA) approach [91] has yielded some remarkable device efficiencies [33, 86–90]. By the way, this concept has been applied successfully long time ago in small molecular dyes [92]. Recently, photoconductivity investigations in DA-polymers have become central in a number of studies [93–95]. From these studies it is apparent that there is no consensus about the mechanisms of charge generation,

recombination and transport in DA polymer blends with acceptors such as PCBM. It has led to a revival of "old" questions concerning the details of charge generation in organic materials.

In this work we investigate formation and recombination of charge carriers in donor-acceptor type copolymer spirobifluorene-co-benzothiadiazole (PSF-BT) doped with PCBM.

4.1 Experimental

PSF-BT was obtained from Merck KGaA Darmstadt. It was synthesized as described in ref. [96]. The $PC_{60}BM$ was obtained from Nano-C. F8BT has been obtained from American Dye Source ADS, Canada. For fluorescence measurements, polymer solutions in tetrahydrofurane (THF) were prepared with an optical density of about 0.1 at 375 nm in a 1 cm cuvette. Solutions with an optical density of about 0.3 in a 1 mm cuvette were prepared for the transient absorption investigations. Polymer films were deposited on the indium-tin oxide (ITO) covered glass by spin coating from toluene solution, followed by the deposition of an aluminium top electrode. The polymer film thickness was about 100 nm. Devices were encapsulated under argon atmosphere by sealing a glass lid with epoxy resin.

The samples were prepared by spin-coating polymer/PCBM solutions in chlorobenzene (20 g/L) on ITO coated glass plates. Active layer thickness was 106, 108, 120 nm for blend films with 1 %, 10 % and 30 % PCBM, respectively and 112 nm for neat film. Aluminum electrodes were evaporated on top at a base pressure of 10^{-6} mbar.

The fluorescence spectra and fluorescence decay kinetics were measured with an Edinburgh Instruments fluorescence spectrometer F900. A diode laser EPL-375 emitting 50 ps pulses at 375 nm with a repetition rate of 20 MHz was used for excitation. The average excitation power was about 1 $\mu W/cm^2$. Initial part of the fluorescence decay dynamics was investigated

employing picosecond fluorescence spectrometer based on Hamamatsu streak camera C5680 and femtosecond laser delivering pulses at a rate of 80MHz and at a wavelength of 350 nm.

Femtosecond transient absorption measurements were carried out on a femtosecond spectrometer based on femtosecond Ti:sapphire laser Quantronix *Integra-C*, generating 130 fs duration pulses at 810 nm at a 1 kHz repetition rate. In these experiments samples were optically excited at the 400 nm (for pure F8BT anf PSF-BT investigations) and 500 nm (for PSF-BT blends with PCBM) wavelength and density of about 10 μJ/cm^2 employing output from traveling wave parametric amplifier TOPAS C.

Integral mode photocurrent measurements were performed using electrical pulse generator Tektronix AFG3101 and oscilloscope Agilent DSO5054A. The oscilloscope input load of 1MΩ was connected in serial with 9MΩ load resistance in order to increase time constant of the setup and extend time range of the observations of the integrated photocurrent to milliseconds. We used second harmonic (532 nm) of Nd:YAG picosecond laser (SL300, Expla ltd.) delivering pulses of 150 ps duration at a rate of 4Hz for sample excitation. The flux was similar as in pump-probe experiments of about 10 μJ/cm^2 but in this case excitation wavelength was at the far red tail of the PSF-BT absorption band.

4.2 Spectroscopy of polymers in solution

Firstly, we discuss exciton diffusion and annihilation processes in solutions of both polymers, F8BT and PSF-BT, in THF. Fig. 4.1 shows transient absorption spectra of F8BT in solution.

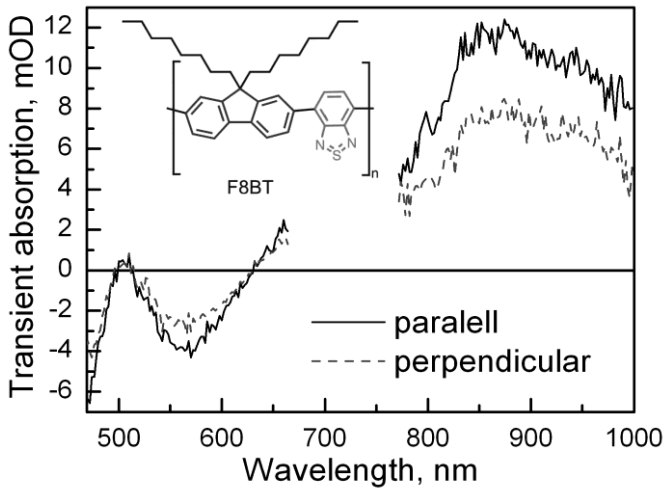

Fig. 4.1. Transient absorption spectra of F8BT polymer in THF solution measured at 25 ps delay time at parallel and perpendicular excitation and probe polarizations.

The spectra are qualitatively similar to those of F8BT films reported in ref. [97] revealing a stimulated emission band in the 500-650 nm region and an excited state absorption at longer wavelengths. Transient absorption kinetics measured at various probe wavelengths (not presented) are identical except of the fast initial decay, which appears only at the long wavelength slope of the fluorescence band. We attribute the fast component to the shift of the stimulated emission band to the long wavelength side taking place during the excited state stabilization. Fig. 4.2 shows the transient absorption kinetics at 650 nm measured at various excitation intensities.

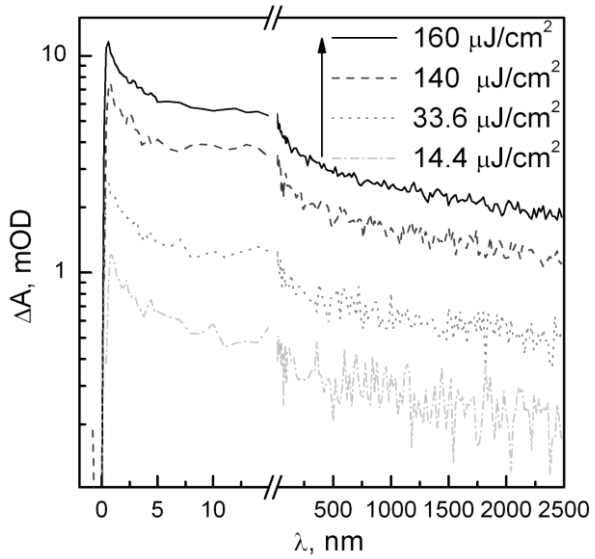

Fig. 4.2. Induced absorption kinetics at 650 nm measured in F8BT solution in THF at varous excitation intensities.

At low excitation intensities the kinetics reveals a relaxation with a time constant of about 3.5 ns in addition to the fast relaxation component. Since this relaxation component is independent of probe wavelength, we attribute it to the excited state relaxation. It is slightly slower compared with the fluorescence decay featuring a time constant of 2.5 ns. The slower induced absorption decay may be an indication of formation of some long-living excited states. However, the experimentally limited time interval of transient absorption investigations does not allow examination of the kinetics in more detail. A weak, of hundreds of ps relaxation component appears at high excitation intensities, which we attribute to the exciton-exciton annihilation. From comparison of the transient absorption intensity with steady state absorption we infer that up to 10 % of conjugated segments are excited at the highest excitation intensity (160 μJ/cm^2). It is plausible that under such conditions excitations on conjugated segments appear close to each other facilitating exciton annihilation by Foerster energy transfer. Similar exciton-exciton annihilation, however on tens of ps time scale has been observed in MeLPPP solution at high excitation intensity [98].

Additional information about exciton diffusion is provided by the transient absorption anisotropy kinetics. The inset in Fig. 4.3 shows the anisotropy decay calculated from the transient absorption kinetics measured at parallel ΔA_{II} and perpendicular $\Delta A_{\perp}$ excitation and probe polarizations as: $P = (\Delta A_{II} - \Delta A_{\perp})/(\Delta A_{II} + 2\Delta A_{\perp})$. The initial anisotropy of slightly more than 0.2 is about two times lower than the maximal value for disordered systems. The anisotropy decay is non-exponential, it may be approximately described by the 500 ps and 1 ns time constants. The fluorescence anisotropy decay kinetics is also presented in the insert in Fig. 4.3.

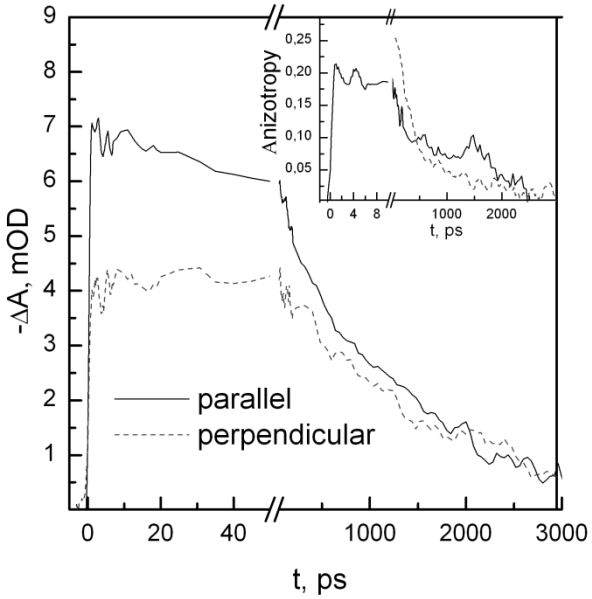

Fig. 4.3. Transient absorption kinetics at 550 nm measured at parallel and perpendicular excitation and probe light polarizations in F8BT solution in THF. The insert shows the absorption anisotropy decay calculated from the transient absorption kinetics (solid line) and the fluorescence anisotropy decay (dashed line).

Lower time-resolution of the fluorescence measurements does not allow us to confirm the data from transient absorption at early times, nevertheless, the initial fluorescence anisotropy is only slightly higher than that of the transient absorption. The low initial transient absorption anisotropy value is evidently not caused by exciton reorientation. A more likely reason is

a slightly different orientations of the ground state and excited state absorption transition dipole moments. At longer times both, the anisotropy decay kinetics and the fluorescence anisotropy kinetics are identical within the experimental accuracy, which supports the conclusion that the induced absorption is related to the excited state absorption of fluorescent states. The anisotropy decay reflects the exciton diffusion rate [98–100], however, more information about the polymer chain configuration is necessary in order to characterize the exciton diffusion process in more details.

The transient absorption spectra of the PSF-BT solution in THF show (see Fig. 4.4) only an induced absorption (no stimulated emission).

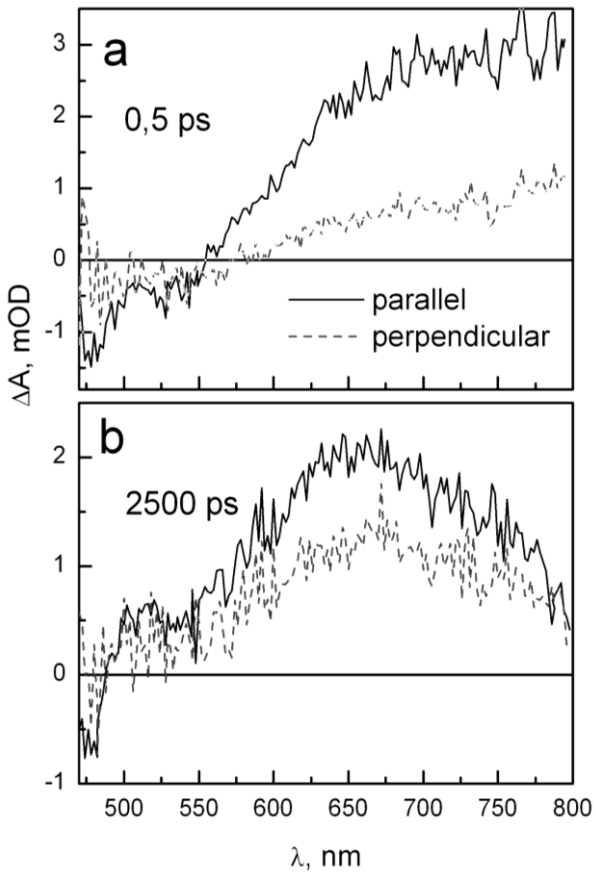

Fig. 4.4. Transient absorption spectra of the PFS-BT solution in THF at 0.5 ps and 2500 ps delay times measured for parallel and perpendicular excitation and probe polarizations.

They are similar to the transient absorption spectra in films of PSF-BT [78]. The transient absorption, its kinetics and the absence of the stimulated emission in films was explained as a consequence of the rapid formation of weakly emissive internal CT states, by electron transfer from the alkoxy-substituted fluorene side group to the benzothiadiazole subunit of the main chain. Fluorescence of of PSF-BT solutions in THF decays nonexponentialy with the time constants of 491 ps (21 %) and 2.34 ns (79 %) and exhibits a very low fluorescence yield of about 0.02 [101]. A relatively long fluorescence lifetime and the low yield indicate that weakly fluorescent excited states are formed in a polymer solution, as well as in neat films [101]. It is conceivable that the polar solvent THF stabilizes the ICT in PSF-BT.

The transient absorption kinetics presented in Fig. 5 reveals a fast process during initial 10 ps. It is interpreted as formation of the weakly fluorescent CT state. The initial neutral exciton state, strongly absorbing at 800 nm, transforms into the ICT state, strongly absorbing at 650 nm within a few ps. There is no dependence of the transient absorption decays in PSF-BT solution in THF on the excitation intensity observed (not presented) and, thus, no signatures of exciton-exciton annihilation. It indicates that exciton-exciton annihilation in PSF-BT is even less efficient than in F8BT.

The anisotropy relaxation in PSF-BT solution is more complex. Transient absorption spectra measured at different excitation and probe polarizations (Fig. 4.4) show more than two times stronger induced absorption at parallel excitation and probe polarizations, which is close to the maximal anisotropy value of 0.3. At 2.5 ns, the anisotropy in the red spectral (650 nm) region remains high ($\Delta A \sim 0.01$), while it decays almost to zero in the long wavelengths region (800 nm). The decay is slightly faster than the fluorescence anisotropy kinetics (not presented), which decays with a time constant of about 4 ns. This supports the assignment of the near IR transient absorption to absorption of the radiative excited state. The anisotropy of the induced absorption at 650 nm (see Fig. 4.5) reduces only slightly during 2.5 ns.

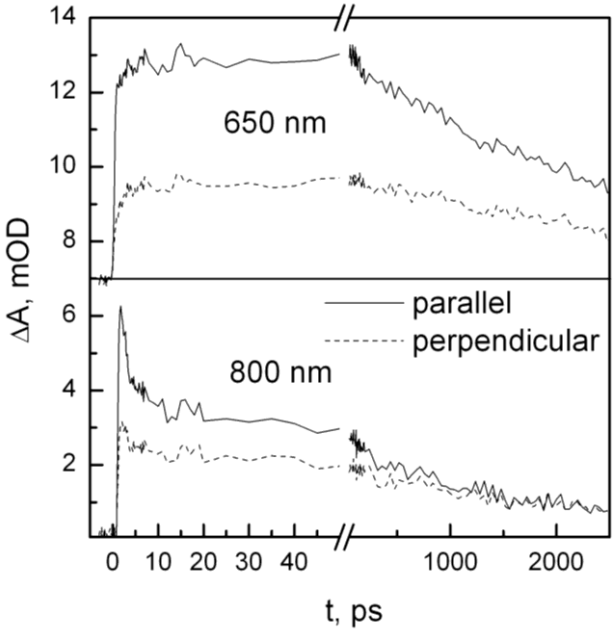

Fig. 4.5. Transient absorption kinetics of the PFS-BT solution in THF at 650 nm and 800 nm for parallel and perpendicular excitation and probe polarizations.

It indicates that the created ICT states are immobile. This is a natural conclusion, because the ICT states can not move by Forster energy transfer and they are also expected to be strongly self trapped because of large dipole moments.

4.3 Spectroscopy of neat polymer films

The transient absorption kinetics of the F8BT film at 550 nm and 680 nm measured under different excitation intensities are shown in Fig. 4.6. According to the assignment performed by Stevens et al. [97], the 680 nm wavelength corresponds to the induced absorption band peaking at about 820 nm and is assigned to excitons. A fast decay, which is weak at low excitation fluence, gains intensity at higher pump fluences. We ascribe this fast relaxation

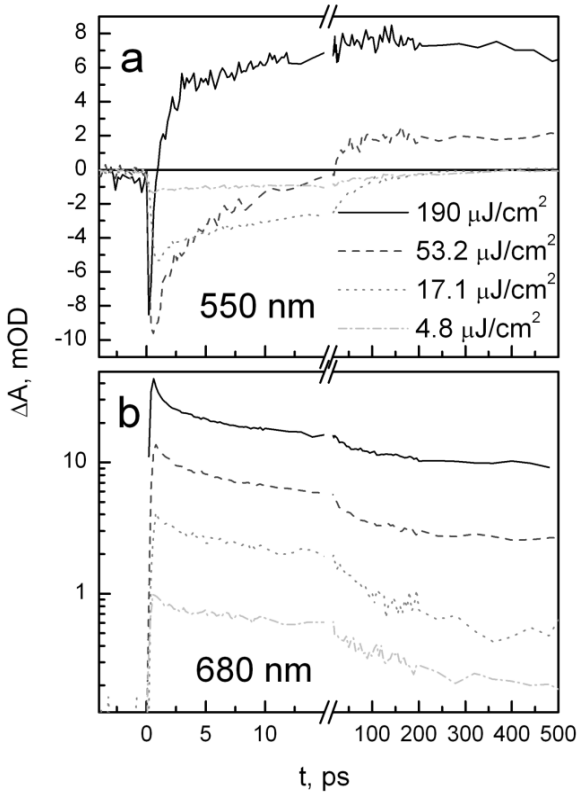

Fig. 4.6. Transient absorption kinetics of the F8BT film at 550 nm and 680 nm measured at various excitation intensities.

component to exciton-exciton annihilation. The exciton decay on a hundreds of ps time scale is evidently also affected by annihilation. Additional support for this statement is the nonexponetial and faster decay of transient absorption than that of fluorescence, which was measured at very low excitation intensity. The decay time of fluorescence is about 900 ps [102]. We calculated the density of excitons based on the excitation fluence, accounting for sample thickness and absorbance. The density is about 1.6×10^{19} cm^{-3} and 3×10^{17} cm^{-3} for the highest and lowest excitation intensities, respectively. These values correspond to an average distance between excitons of about 3.7 nm and 14 nm. An independent measure of the distance between excitons can be obtained by comparison of the induced absorption with the ground state absorption. We estimate two times higher exciton densities and, thus, slightly shorter average distances between excitons. About half of the excitons annihilate within 5 ps at the highest

excitation intensity (Fig. 4.6). The annihilation onset starts already at the minimal used excitation intensity. It indicates an average exciton diffusion length on the order of 10-15 nm, which is a typical value for conjugated polymers and about two times the length of a conjugated segment. The initial value of the transient absorption signal is proportional to the excitation intensity indicating that no significant exciton-exciton annihilation takes place during the excitation pulse action.

In a F8BT film stimulated emission by excitons is observed at 550 nm, however, polarons also absorb at this wavelength. Thus, competition between these two processes occurs and determines the transient absorption dynamics, which strongly depends on the excitation fluence. The stimulated emission decays during several hundreds of ps at the lowest excitation intensity in agreement with the fluorescence decay kinetics. By increasing the excitation intensity the decay rate increases and the stimulated emission band turns into induced absorption on a tens of ps time scale, or even within several ps at the highest excitation intensities. Long-lived polaron pairs are created which strongly absorb at 550 nm.

Enhanced generation of polaron pairs at high excitation intensities has been observed in various organic materials and attributed to easy dissociative high energy excited states populated by exciton-exciton annihilation or by sequential excitation [97]. Based on the modelled polaron absorption intensity dependences on the excitation fluence Stevens et al. argue exciton-exciton annihilation is responsible for the polaron generation in F8BT. Our estimations are also in favour of exciton-exciton annihilaition being responsible for polaron formation. Sequential excitation generally needs higher excitation intensities, because a single polymer segment needs to be excited two times. While in the case of exciton annihilation it is sufficient to create two excitations within the annihilation or diffusion radius, which is on the order of 10 nm in conjugated polymers. According to our estimation, about 2 % of conjugated segments are excited at 53 $\mu J/cm^2$ excitation intensity. Assuming, the excited state absorption cross section at the excitation wavelength is equal to that of the

ground state absorption, we obtain a probability of sequential excitation of a particular conjugated segment equals to about 0.04 %, only. In contrast in Fig. 6a we observe a high polaron absorption, which is only less than 5 times lower than the initial negative signal due to the stimulated emission.

Fig. 4.7 shows the transient absorption kinetics of a PSF-BT film at 550 nm and 680 nm measured with increasing excitation intensity.

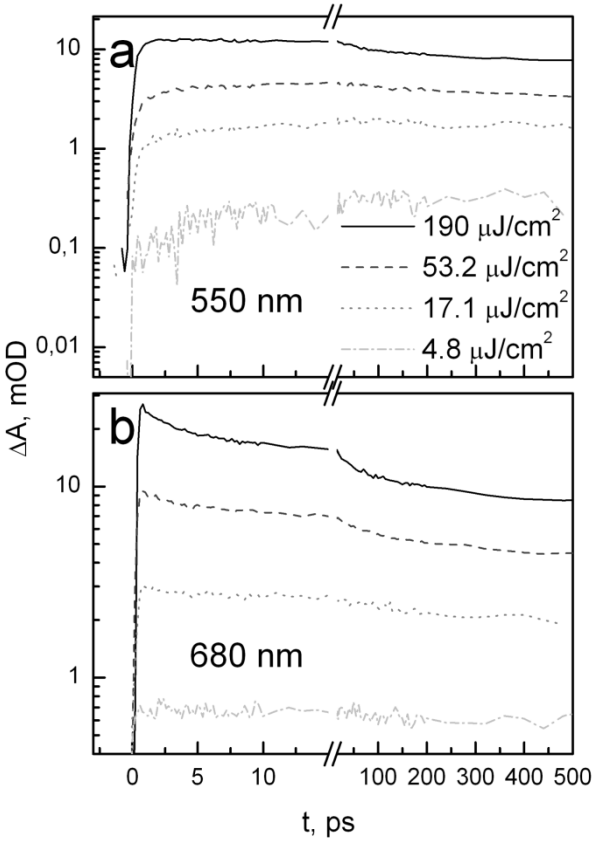

Fig. 4.7. Transient absorption kinetics of the PSF-BT film at 550 nm and 680 nm measured at various excitation intensities.

In contrast to F8BT and as in PSF-BT solution no stimulated emission is observed. An induced absorption is observed at both probe wavelengths, however, its kinetics is very different. The induced absorption in PSF-BT at 680 nm has been assigned to be dominated by excitons, as well as for the F8BT films, while absorption at 550 nm has been assigned to the ICT states with electron localised on benzothiadiazole and the hole localized on the

spiroconjugated fluorene side group [96–104]. At low excitation intensity the transient absorption at 680 nm shows only minor relaxation on a subnanosecond time scale. A fast relaxation component related to exciton-exciton annihilation starts to appear only at 53 $\mu J/cm^2$, when the exciton concentration reaches about 4×10^{18} cm^{-3}, thus the annihilation efficiency is evidently significantly lower than in case of F8BT.

PSF-BT films show no stimulated emission at 550 nm even at the lowest excitation intensity. As was demonstrated in ref. [102] the competition between the stimulated emission and the induced absorption depends on the excitation wavelength. The stimulated emission at short delay times has been observed only with the sample excitation to the long wavelength edge of the absorption band, when little excess energy is provided to excite polymer segments, which facilitates formation of ICT states. In the present investigation with excitation at 400 nm, an induced absorption appears very rapidly during the excitation pulse action, and additionally grows on a tens of ps time scale. Both, the very rapid and gradually growing induced absorption parts depend approximately linearly on the excitation intensity. These observations lead to conclusion that the induced absorption increases approximately twice on a tens of ps time scale independently of the excitation intensity, and only the growths dynamics depends on the excitation intensity. Thus, extra energy provided to the excited polymer segments during exciton-exciton annihilation speeds up formation of the ICT state, however, does not change the total ICT state yield at long times.

Transient absorption dynamics on a subnanosecond time scale becomes identical at both probe wavelengths. It evidently reflects recombination of the ICT state. Almost no recombination takes place during 500 ps at low excitation intensity. The recombination rate increases at high excitation intensities. It indicates that annihilation of ICT excitons or, interchangeably, nongeminate recombination of electron-hole pairs becomes important at high their densities. In accord with the model of exciton-exciton annihilation it does not create free charge carriers but tightly bound electron-hole pairs, ICT excitons in PSF-BT

film. In order to determine the annihilation role in free charge carrier generation we have measured the open circuit photovoltage and time-integrated photoluminescence intensity as functions of the excitation intensity. The investigation results are presented in Fig. 4.8.

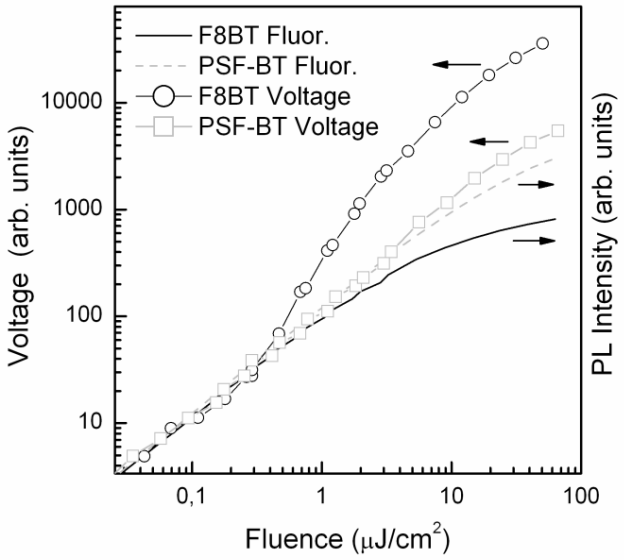

Fig. 4.8. Photoluminescence intensity and photovoltage dependences on the excitation fluence in F8BT and PSF-BT films.

The fluorescence intensity of the F8BT film starts to deviate from the linear excitation intensity dependence at about 1 μJ/cm^2 excitation fluence. Thus, in agreement with the presence of the fast relaxation component in the transient absorption kinetics (Fig. 4.6b), exciton-exciton annihilation in F8BT can not be disregarded even at the lowest excitation intensities used in the transient absorption investigations. The nonlinear growth of the photocurrent starts approximately at the same excitation fluence supporting our conclusion relating the carrier generation with exciton-exciton annihilation.

Saturation of the PSF-BT fluorescence is much less significant (Fig. 4.8). The saturation starts at approximately 10 times higher intensity than in F8BT films. Thus exciton-exciton annihilation in PSF-BT films is much less efficient. This is a logical conclusion. Exciton-exciton annihilation is

determined by Forster energy transfer between excited molecules. The transfer rate is determined by dipole moments of the excited state absorption transition and the stimulated emission transition. The stimulated emission dipole moment of PSF-BT rapidly decreases when it relaxes to the ICT state, thus causing slow energy transfer. In PSF-BT film, the generated photovoltage increases linearly with the excitation intensity up to 10 $\mu J/cm^2$. We do not see any indications of the enhanced charge carrier generation efficiency by exciton-exciton annihilation. This confirms the conclusion that exciton-exciton annihilation just speeds up formation of ICT states, but does not facilitate formation of free charge carriers.

4.4 Spectroscopy of polymer blends

4.4.1 Fluorescence

Fluorescence of neat PSF-BT films we analyzed in detail in ref. [102] . We found that the fluorescence decays non-exponentially due to the formation of localized intramolecular CT excitons with hole located on the spiroconjugated FSG. Formation of the CT exciton is accompanied by the conformational relaxation and a continuous decrease of the transition dipole moment to the ground state. Exciton migration manifests itself as a dynamic bathochromic shift of the fluorescence band, which indicates gradual occupation of lower energy sites within the density of states. Here, we also present fluorescence spectrum and decay kinetics of the neat polymer film in Fig.s 4.9 and 4.10 for their comparison with fluorescence properties of doped films.

Intensity, spectral shape and decay dynamics of PSF-BT fluorescence substantially change upon addition of PCBM (Fig. 4.9, 4.10). The fluorescence band shifts hypsochromically by increasing the PCBM fraction (by about 30 nm at 30 % of PCBM) and a new fluorescence band appears in the long wavelength region. Intensity of the intrinsic PSF-BT fluorescence at 565 nm decreases by a factor of two in blend with 1% PCBM compared with neat

films. Thus, still large fraction of excitons decay by the same mechanism as in neat films. Upon adding more PCBM (10 and 30 %) intensity of the PS-FBT fluorescence band further decreases, yielding only about 1% and 0,4% of the neat film fluorescence, respectively.

The new band peaks at about 725 nm and we assign it to the fluorescence of PCBM. The peak at about 725 nm coincides with the PCBM fluorescence peak reported in ref. [105, 106] and, in addition, the measured lifetime of 1.3 ns of the fluorescence decay at 725 nm (see Fig. 4.10 insert) coincides with the fluorescence lifetime of neat PCBM films [106, 107]. Thus, it is plausible to assign the band at 725 nm to fluorescence of PCBM, which is excited directly or by excitation energy transfer from photoexcited polymer. On the other hand, the new band extends to almost 600 nm and this is far too short wavelength for the PCBM fluorescence. Fluorescence of PCBM spans from about 700 nm to infrared region [105–107]. Thus, the blue part of the fluorescence is probably a combination with CT fluorescence.

Decay dynamics of the PSF-BT fluorescence at 560 nm reveals gradual increase of the fluorescence decay rate with increase of the PCBM concentration (Fig.4.10). Fluorescence of blend with 1% PCBM decays faster compared to neat film, but the slow relaxation component typical for PSF-BT [102] is still observed after several nanoseconds. Fluorescence quenching by PCBM is substantially stronger and faster in 10% and 30% blends. The initial fluorescence decay becomes limited by the time resolution of the setup of about 3 ps in case of 30% blend. For numerical characterization, we have fitted the fluorescence decay by bi-exponential function. Results are summarized in Table 4.1. The quenching rates are similar to those obtained for other polymer/electron-acceptor blends [108–110].

The fluorescence quenching dynamics explains the hypsochromic band shift discussed above. As was shown in ref. [102], fluorescence band of PSF-BT experiences a strong dynamic band shift to the long wavelength region. The fluorescence maximum shifts from about 530 nm (0 ns) to 560 nm (30 ns) (ref [102]). Quenching of the excited states appears therefore as fluorescence

time-gating; fluorescence is quenched before excited states reach the "red-shifted" low energy state. Indeed, fluorescence spectrum at 30% PCBM concentration is very similar to the initial fluorescence spectrum reported in ref. [102].

Attribution of the long wavelength fluorescence band to PCBM also implies that the quenching of the PSF-BT fluorescence may be caused by energy transfer to PCBM. On the other hand, photoconductivity of the blends, which will be discussed below, indicates that electron transfer between PSF-BT and PCBM also takes place and apparently causes additional PSF-BT fluorescence quenching. With the similar donor F8BT, without a spiroconjugated FSG, it was found that energy transfer to PCBM dominates over electron transfer. It was argued that similar energies of the HOMO levels of F8BT and PCBM prevent electron transfer [107]. HOMO level of the PSF-BT polymer backbone (HOMO-4) has similar energy to that of F8BT, however PSF-BT has an additional HOMO level at higher energy related to the spiroconjugated FSG [101]. The presence of this level apparently enables electron transfer to PCBM. Therefore both PSF-BT fluorescence quenching mechanisms are likely to be active to some extent.

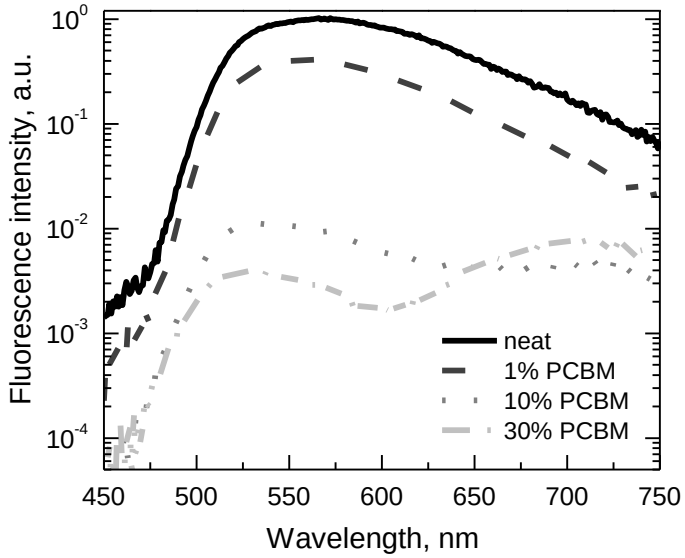

Fig. 4.9. Fluorescence spectra of neat PSFBT film and blends containing 1%, 10% and 30% of PCBM.

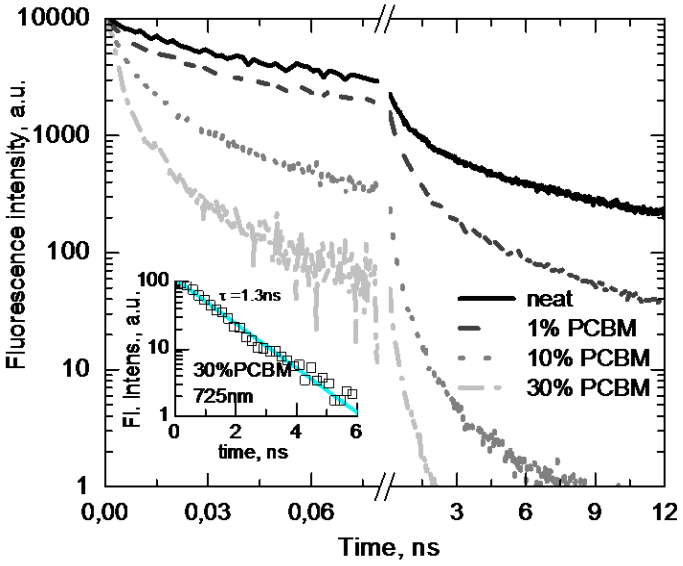

Fig. 4.10. Fluorescence decay kinetics at 560 nm of neat PSFBT film and blends containing 1%, 10% and 30% of PCBM as indicated. Initial part (before the break) obtained employing streak camera. Data on nanosecond scale were measured with lower temporal resolution (Edinburgh Instruments spectrometer F900). Insert displays the fluorescence decay kinetic in 30% blend at the peak position of new band at 725 nm and monoexponential fit with time constant of 1.3 ns.

Table 4.1. Biexponential fit parameters of fluorescence kinetics obtained by streak camera at 565 nm wavelength.

PCBM conc., %	A_1, %	τ_1, ps	A_2, %	τ_2, ps
0	45	16	55	135
1	46	7	54	75
10	73	5	27	34
30	91	3.2	9	26

4.4.2 Transient absorption

Transient absorption investigations have been performed to get deeper insight into the early time kinetics of excitation and electron transfer. Fig. 4.11 shows the transient absorption spectra of the neat PSF-BT film and blends with 1% and 30% PCBM obtained under excitation at 500 nm. The insert in Fig. 4.11 shows transient absorption kinetics at 450 nm corresponding to the ground state bleaching of PSF-BT. Apparent is the reduction of the transient absorption amplitude in PS-FBT/PCBM blends and fastening of its decay rate in comparison with the neat PSF-BT film. Peculiarities of the transient absorption spectra of neat PS-FBT films were discussed in detail in ref. [102]. Shortly, absorption bleaching is observed at around 450 nm and a broad induced absorption band appears in the visible and near infrared regions assigned to the absorption of intramolecular PSF-BT CT excitons formed when hole localizes on FSG and electron remains on the polymer backbone. Stimulated emission between 500 nm and 550 nm is present in neat PS-FBT films at early times before formation of the intramolecular CT excitons.

Transient absorption spectra of PSF-BT/PCBM blends (Fig. 4.11) have slightly different shapes in comparison with the neat polymer - the induced absorption below 400 nm and stimulated emission (550 nm) decrease stronger than the long wavelength induced absorption (above 580 nm). It should be noted that the spectra were normalized taking into account slightly different sample absorbance at excitation wavelength. Therefore the reduced transient absorption at zero time in blends should be related to the ultrafast exciton decay, faster than the time resolution of our setup (< 150 fs). Since this decay component is faster than the fluorescence quenching kinetics by several orders of magnitude, these two decay components can not be attributed to the same process. It is unlikely that energy transfer can be so fast to be responsible for the ultrafast decay. This is because PCBM absorption in the PSF-BT fluorescence region is very weak, consequently spectral overlap between PCBM absorption and PSF-BT emission is very weak, which, according to the

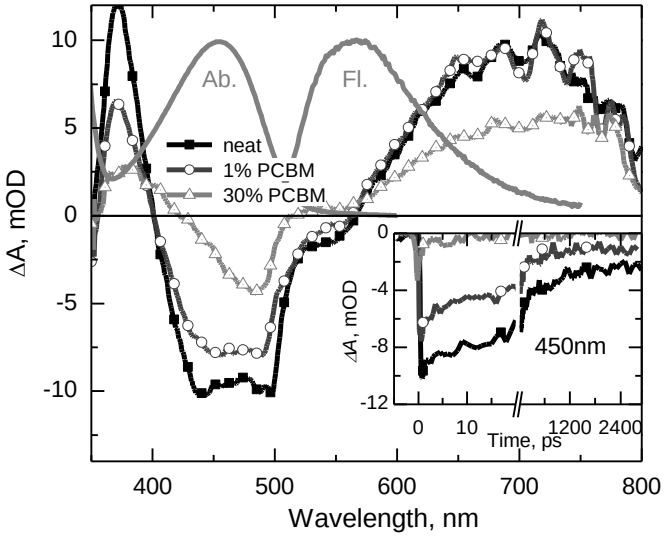

Fig. 4.11. Transient absorption spectra at 0 ps of PSFBT films with various PCBM concentrations. Insert shows transient absorption kinetics of the films at 450nm.

Förster theory, should result in slow energy transfer. Therefore ultrafast relaxation should be more likely attributed to the charge transfer, which in blends of other polymers with PCBM also occurs on a fs time scale [93, 111–113]. Unfortunately, the differential absorption spectrum of the excited PCBM [114] is surprisingly similar to that of PSF-BT, hence giving no possibility to clearly identify the energy or charge transfer processes. To disentangle these processes we have to rely on photoconductivity measurements as detailed below.

4.4.3 Initial carrier drift dynamics

Temporal evolutions on a ps time scale of the relative electric field strength within the bulk of neat PSF-BT films and in blends with 1% and 30% of PCBM obtained by TREFISH are shown in Fig. 4.12. Initial drop of the field strength evolving during the first picosecond after photoexcitation has the largest value in the neat film and becomes smaller with higher PCBM

concentration. This initial drop is attributed to the displacement current caused by the polarization of the photogenerated excitons by electric field [115]. This contribution is proportional to the sample absorbance and electric field strength, therefore $\Delta E/E$ is approximately independent of the applied field. In the neat film the field gradually continues to decay because of the charge carrier generation and drift, and the decay rate increases with applied voltage. At later times, the field kinetics strongly depends on the applied voltage and on the PCBM concentration.

The electric field kinetics is drastically different in blends. The initial field drop attributed to the displacement current slightly decreases with the increase in PCBM concentration, and the field decay on a tens of ps time scale becomes weaker. The most drastic difference becomes apparent on a few ns time scale: the electric field in the neat film continues to decay, while in the blends we observe recovery of the electric field, which is most pronounced at low applied voltage in the film with 30 % PCBM concentration. Thus, PCBM inhibits the photocurrent on a ps time scale, and what is more surprisingly, even causes the field recovery.

Fig. 4.13 shows temporal evolutions of the carrier drift distances averaged over electrons and holes calculated from the electric field kinetics by using eq. 2.3, evaluating the charge carrier density from the integrated extracted charge at long times (see Fig. 4.14), as discussed below. It should be noted,

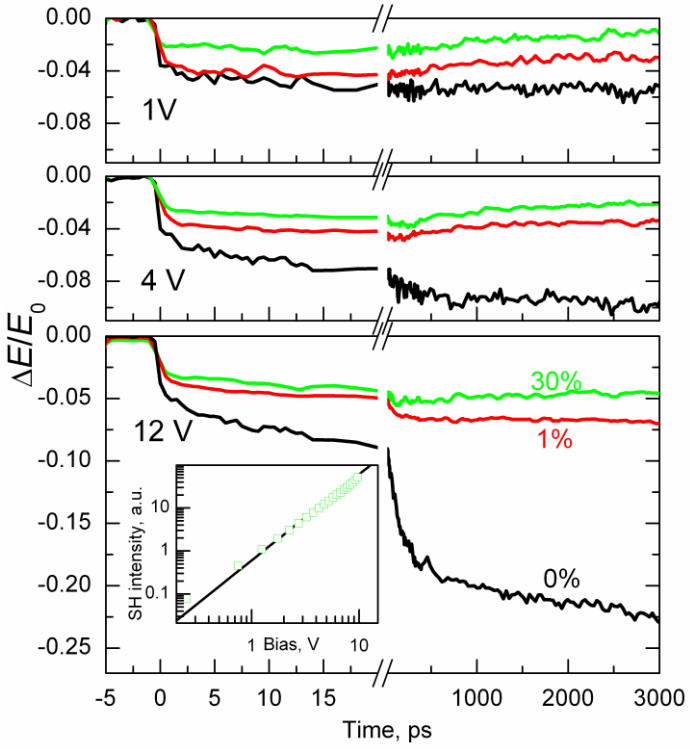

Fig. 4.12. Relative decrease of electric field after photoexcitation in neat PSF-BT film (black curve), 1% blend with PCBM (red curve) and 30% blend with PCBM (green curve) at different voltages of applied bias. Insert shows second harmonic intensity versus applied bias for the neat film (points – experimental data; line – square law fit).

that the initial charge displacement related to the excitons is probably overestimated because of higher density of excitons in comparison with charge carriers. As we can see, the drift distance of charge carriers in neat film during initial 3 ns is shorter than 0.1 nm at 1 V of applied bias, while at 12 V we observe drift by about 6 nm on a subnanosecond time scale and additional drift by about 2 nm at 3 ns. Charge drift in blends is evident until 5-10 ps, while at longer times we observe even negative drift showing that the charge densities partly move back against electric field towards their original positions.

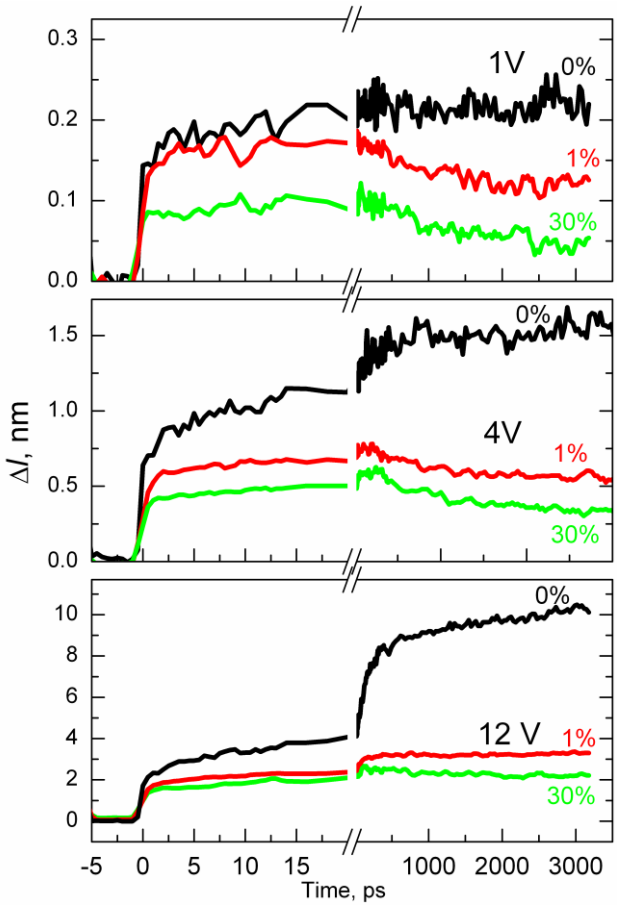

Fig. 4.13. Time dependences of the charge carrier drift distances averaged over electrons and holes in neat film (black curve), blend with 1% PCBM (red curve) and blend with 30% PCBM (green curve) at different applied bias voltages.

4.4.4 Photoconductivity

The charge carrier drift dynamics on a longer time scale ranging from nanoseconds to milliseconds has been investigated by the integral-mode photocurrent measurements. In this experiment voltage dynamics on high resistance external load was recorded giving information about decay of electric field inside the investigated film due to the drift of photogenerated charge carriers, thus the voltage drop on the sample is proportional to the integral photocurrent. Results obtained for the neat film and blends with 1 % and 30 % PCBM at bias voltages of 1 V and 8 V are displayed in Fig. 4.14.

Excitation conditions of all samples were identical. Obviously, photocurrent dynamics is substantially affected by PCBM and there are several remarkable features in these results elucidating the transport phenomenon in the investigated samples. Firstly, consider the case of the bias voltage of 1 V. In the time range from 10 ns to approximately 1 μs, the voltage dynamics on the 1 % blend resembles that on the neat film, only the total voltage decrease and consequently the integral photocurrent in the 1 % blend is about two times smaller. Finally, the integral photocurrent in the 1 % blend exceeds that in the neat film at about 100 μs. The integral photocurrent in the neat film and in the 1 % blend saturates at about 2 ms indicating complete extraction of mobile carriers. Contrary, the voltage decrease on the film of the blend with 30 % PCBM is substantially weaker. The voltage kinetics on the 30 % blend film slows down and a complete plateau is not reached even at 10 ms. There is no strong difference between the total integral photocurrent in the three samples. Thus, surprisingly PCBM only weakly influences efficiency of the charge carrier generation.

The bias voltage strongly impacts the photocurrent dynamics. In contrast to the case of 1 V of bias voltage the photocurrent kinetics at 8 V is very similar for both blends. The initial voltage decrease revealed by TREFISH but not resolved by electrical measurements is several times higher for the neat film than for the blends, however the total integral photocurrent in the neat film is about two times smaller. The final plateau is reached within 10 μs, *i.e.* more than 100 times faster than at 1 V bias. Insert in Fig. 6 shows the amount of the total integral photocurrent as a function of applied bias. It indicates that the electric field assistance is necessary for free charge carrier generation and transport. Evidently only a small fraction of excitations form free charge carriers without electric field.

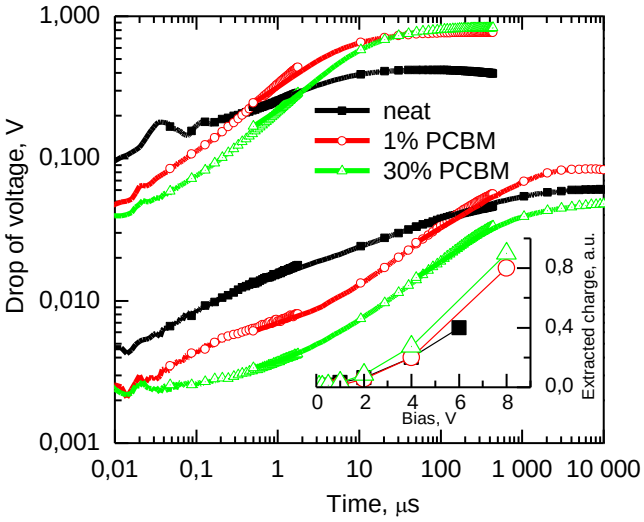

Fig. 4.14. Dynamics of the voltage decrease on films with different PCBM concentrations corresponding to the amount of extracted charge at bias voltages of 1 V and 8 V. Insert shows amount of extracted charge from different films as a function of bias voltage.

4.4.5 Discussion

The current dynamics in neat PSF-BT film at 1 V (Fig. 4.14) reveals two time domains of the carrier motion. The fast carrier drift terminates during about 1 to 10 μs. About half of charge carriers are extracted during this time. The slower drift period lasts up to 1 ms. We attribute the two drift periods to electron and hole transport. As was mentioned, PSFBT is a predominantly electron transporting material because holes are localized on FSG [101]. The electron mobility is of the order of 10^{-3}cm^2/Vs as measured in 3.6 μm thick samples, while the hole mobility is by three orders of magnitude lower [50]. Electron and hole extraction times of several μs and several hundreds of μs respectively revealed by the current kinetics presented in Fig. 4.14 are in good agreement with those mobility values.

The carrier kinetics in films doped with 1% PCBM show similar behavior, but the fraction of the rapidly (during about 1 μs) extracted charge is only 10% or less. We take it as indication that only a small fraction of electrons

(~20%) drift with the same high mobility as in neat film, while mobility of the majority of electrons significantly drops down, their mobility becoming comparable to that of holes. The straightforward interpretation is that this fraction of electrons is trapped by PCBM molecules. The rapidly moving electrons disappear completely in the film with 30 % PCBM. This is surprising, since PBCM at this concentration forms clusters enabling percolation and electrons are expected to have relatively high mobility of about 0.1 to 10^{-4} cm^2/Vs[42]. Therefore, the slow electron extraction form the 30% blend leads to the conclusion that the mobility is *not* the main limiting factor of carrier extraction. Slow carrier extraction in blends is apparently determined by slow generation of mobile charge carriers. Our TREFISH investigations support this assumption, clearly showing that no, or only very few mobile charge carriers are generated in blends on a ps time scale at low applied voltages. It suggests that the charge carriers remain bound in long-lived charge pair states, which dissociate to mobile charge carriers on a μs time scale.

Fig. 4.15 explains the mechanism of the long-lived charge pair state formation. The HOMO orbital of PSF-BT is located on FSG, while LUMO orbital is delocalized within polymer backbone [101]. HOMO-LUMO optical transition has negligible oscillator strength because of very weak HOMO and LUMO overlap. Therefore HOMO-4, which is also delocalized on a polymer backbone, is responsible for the PSFBT absorption. Thus, optical excitation creates excitons, which are delocalized over the polymer backbone. According to the energy scheme presented in Fig. 4.15, electron transfer from excited polymer backbone to PCBM and hole transfer to FSG are energetically favorable processes and create the charge pair state with electron located at PCBM and hole on FSG. Electron transfer to PCBM most likely occurs at locations where polymer backbone and PCBM are in close contact. Such geometry suggests that FSG attached to the backbone should be facing to the opposite direction, thus more remote from PCBM. Therefore, the created charge pair state is expected to have large separation distance and consequently long lifetime reaching microseconds. Interestingly, such a double charge

transfer recreates the ground state of the polymer backbone. Consequently, it recreates the polymer absorption, which was observed as reduced absorption bleaching of blends (see Fig. 4.11).

The key question remains why electrons and holes in PSF-BT/PCBM blend remain in a bound charge pair states, while in blends of other polymers with PCBM the charge pairs effectively dissociate into free charge carriers. Hole localization on FSG is apparently the main distinctive feature of the PSF-BT polymer. Although, charge pair state dissociation in polymer blends is still not completely understood process, however high hole mobility and their delocalization enabling to overcome the Coulomb attraction is evidently one of the major factors determining efficient dissociation of charge pair states [116]. Thus, hole localization in PSF-BT disabling this mechanism is evidently responsible for the inefficient charge pair state dissociation.

Even a low concentration of PCBM additives significantly changes the carrier generation and motion. This is in stark contrast with e.g. common for photovoltaic applications polymer P3HT where 1% of PCBM additives did not change the carrier mobility on a ps-ns time scale (results not presented), while their influence on fluorescence decay was quite similar to that described above for PSF-BT. This is evidently because holes are more mobile in P3HT and dominate in the ultrafast photocurrent phase, therefore electron trapping by PCBM is of minor importance. It should be also noted that the influence of PCBM additives on carrier generation and motion in PSF-BT polymer is related to two processes: exciton quenching, and trapping of generated electrons. Both of them reduce the number of mobile charge carriers, therefore influence of low PCBM fraction on carrier generation and motion is stronger than on polymer fluorescence or transient absorption affected only by exciton quenching.

As follows from eq. 1 (see experimental section) the electric field dynamics on a ps-ns time scale is determined by the interplay of two processes: exciton generation and decay, and drift of free charge carriers. Exciton generation causes instantaneous drop of the electric field and its recovery when

excitons decay [115], while carrier drift causes monotonic field decrease. Electron drift dominates over exciton decay in neat PSF-BT films. While slow drift of both electrons and holes is insufficient to compensate electric field recovery related to exciton decay in doped films at low applied voltages causing unusual electric field kinetics.

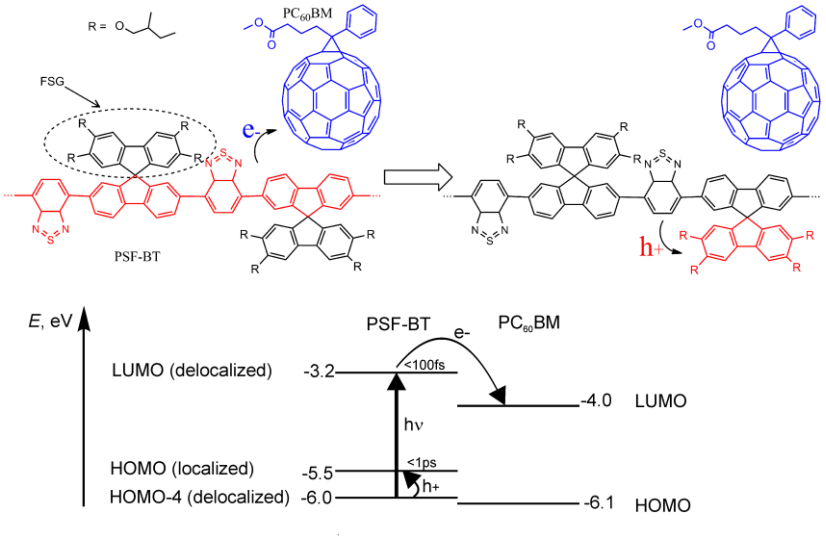

Fig. 4.15. Charge transfer scheme of the formation of long-lived charge pair state in PSF-BT/PCBM blend. Electron transfer from excited polymer creates CT state with hole (red) on polymer backbone and electron (blue) on PCBM (on the left side), subsequent hole transfer to FSG creates CT state with hole localized on FSG and recreates ground state of the polymer backbone (on the right side). Alignment of energy levels of PSF-BT and PCBM is shown below.

4.5 Concluding remarks

Exciton-exciton annihilation takes place in neat films of both investigated polymers, however, it starts at about 10 times higher intensity and is less efficient in PSF-BT films compared with F8BT films. Exciton-exciton annihilation facilitates charge carrier generation in F8BT films, but no influence on the carrier generation was observed in PSF-BT films. Exciton annihilation in PSF-BT films only speeds up formation of the ICT state.

Investigations revealed unexpected influence of PCBM on the carrier generation and motion. PCBM additives quench the polymer fluorescence mainly by relatively slow energy transfer. On the other hand, PCBM additives slightly increase the carrier generation efficiency, however electron extraction time slows down by two orders of magnitude in comparison with neat polymer. We attribute this behavior to the ultrafast electron trapping by PCBM and creation of tightly bound electron-hole pairs, which dissociate on microsecond time scale under the assistance of applied electric field.

Investigation results demonstrate complexity of the charge carrier generation and motion processes in blends of polar molecules or donor-acceptor copolymers with fullerene derivatives.

5 Charge Transfer States in Merocyanine Neat Films and Its Blends with PCBM

The growing need for energy stimulates scientific research aiming to develop efficient, low-cost energy sources, one of them may be photovoltaic devices. Organic semiconductors have emerged as a new class of materials, which hold promise for the development of low-cost and large-area solar cells. The bulk heterojunction (blend) concept [80] has turned out to be the most promising approach to highly efficient organic solar cells since it features an extended interface between the phases of the electron donor and the electron acceptor compounds and leads to enhanced generation of free charge carriers [37, 81]. A broad variety of organic conjugated polymers [2] and small molecules can be used as electron donors, [27] while fullerene derivatives are the most common electron acceptors. Small molecules may be deposited under high vacuum conditions by thermal evaporation. On the other hand, soluble materials like polymers can be spin-coated from solution. Many semiconducting polymers have been successfully applied in solution processed solar cells [86, 87].

Polymer blends have been widely investigated and charge generation and transport are comparatively well understood [93, 117]. Understanding of photophysical properties and charge generation in blends of small molecules is less thorough [118, 119]. It is conceivable that solar cells of small organic molecules have a higher potential to meet challenges of commercialization due to the ease of synthesis, purification and processing as demonstrated by 12 % in tandem solar cells [33]. Besides this tremendous improvement over the last ten years, little is known about relevant photophysical processes in small molecule materials and their blends compared with polymers, thus more detailed research is necessary to unravel unused potential of these materials. It is very likely that some technological improvement of vacuum deposition or solution processing may increase the efficiency of small-molecule based solar cells dramatically.

Recently, a number of low-molecular-weight dyes have been introduced as new absorbers and electron-donating compounds in blend solar cells, among them squaraines, [47, 120] thiophenes, [119] donor-acceptor thiadiazoles [93] and merocyanines [9, 48] leading to efficient devices. It is promising in terms of application that merocyanine molecules can be either thermally evaporated in vacuum or processed from solution.

Different fabrication technologies give more freedom for optimization of the film morphology, which is crucial for the efficiency of the cells. Phase segregation, formation of domain structure and domain sizes were found to be very important film morphology parameters, which strongly influence the free charge carrier generation and recombination. Investigation of polymer based solar cells revealed that high content of fullerene derivatives (of 50% or more) is essential to achieve high efficiency [106, 121, 122]. It was explained by either higher dielectric permittivity of PCBM ($\varepsilon_r = 4\pm1$) [123–125], which at high concentration increases relative permittivity of the blend and reduces electron-hole binding energies [107], or by longer separation distances of generated charge pairs in larger domains formed at higher PCBM concentration [106].

Understanding of the role of morphology in the solar cell performance is impossible without clear understanding of the carrier generation and recombination processes. A large number of papers are devoted to this problem, however still no consensus is achieved on the mechanism of how charge carriers overcome mutual Coulomb attraction during splitting of interfacial charge transfer states into free charge carriers.

The main goal of investigations in this chapter is to understand the generation and dynamics of excitons, charge transfer excitons, and charge carriers in merocyanine neat films and blends with fullerene derivatives.

5.1 Sample preparation and experimental survey

The syntheses of merocianine MD376 has been described in ref. [126]. For investigations of MD376 properties in solutions, it was desolved in toluene, chlorobenzene (CB) or dichloromethane (DCM) at concentrations between 10^{-3} and 10^{-6} mol/L.

The deposition of merocyanine layers from solutions on glass substrates was performed by spin coating from MD376 solution in chlorbenzene. It was solved with a concentration of 15 mg/ml and spin coated to obtain film thicknesses of ca. 55 nm. For blend films a MD376 solution was mixed with PCBM solution in various ratios using the same solvent and identical concentrations.

Streak camera Hamamatsu C5680 with synchroscan unit M5676 was used for the measurement of fluorescence dynamics with ps time resolution. For the excitation, a femtosecond Yb:KGW oscillator (Pharos, Light Conversion Ltd.) was employed. The oscillator produced 80 fs 1030 nm light pulses at 76 MHz repetition rate, which were frequency tripled to 343 nm (HIRO harmonics generator, Light Conversion Ltd.), attenuated, and focused into ~ 100 μm spot on the sample resulting in about 1 mW/mm^2 average excitation power. The maximum time resolution of the whole system was about 3 ps.

For temperature dependent photoluminescence spectra the samples were kept in a customized Cryostat (CryoVac) under Nitrogen atmosphere and were excited at 566 nm using the beam of an InnoLas Spitlight300 Nd:YAG Laser with ca. 4 ns pulse width and 20 Hz repetition rate to operate an OPO (GWU versaScan). PL spectra were recorded with a PI-MAX2 CCD camera from Roper Scientific after passing an Acton 2300i spectrograph with appropriate gratings.

Transient absorption investigations have been performed by means of conventional broadband femtosecond absorption pump-probe spectroscopy. The spectrometer was based on an amplified femtosecond Ti:sapphire laser

(Quantronix *Integra-C*) generating pulses at 805 nm of approx. 130 fs duration at 1 kHz repetition rate. Pulses of optic parametric generator *TOPAS C* at 500 nm wavelength were used for the excitation of the sample. White light continuum for probing was generated in a 2 mm thick sapphire plate. The excitation beam was focused into a spot of about 500 μm diameter, while the diameter of the probe spot was about 300 μm. The differential absorption (ΔA) is defined as the negative logarithm of the ratio of transmitted light with and without optical excitation (pump), respectively. Thus, positive signals correspond to induced (excited state) absorption and negative signal are due to absorption bleaching and/or stimulated emission.

Optical density of the blend films at the excitation wavelength was below 0.25, therefore excitation intensity was almost homogeneous over the sample thickness. The photon flux was of about 5 μJ/cm^2 (~10^{13} ph/cm^2) per pulse.

The syntheses of merocyanine MD376 has been described in ref. [126]. The samples had solar cell architecture (fig. 5.1).

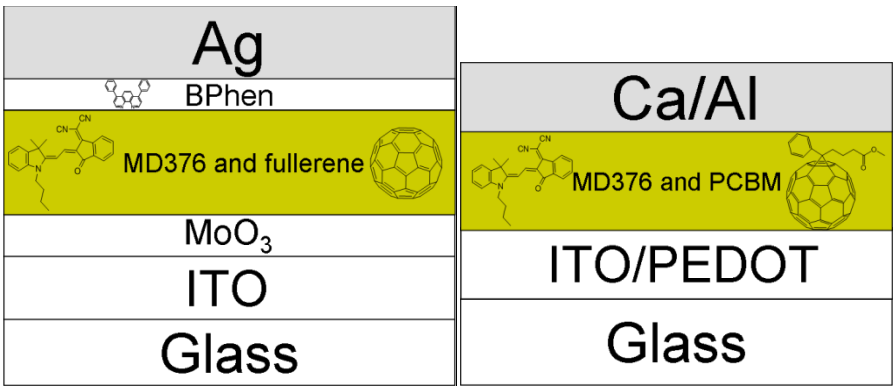

Fig. 5.1. Organics solar cells based on merocyanine MD376/fullerene derivatives structure. Vacuum and solution processes OCS are shown in this figure.

Vacuum deposited sample structure is shown in fig. 5.1a. The OSC active layer of MD376/fullerene blend (~50 nm) is between two electrodes transparent ITO (anode) and Ag (cathode). MoO_3 layer of 20 nm thickness increases the efficiency of holes extraction. BPhen organic molecules layer of 6 nm thickness with high band gap are used in order to prevent exciton quenching by Ag electrode.

Solution processed sample structure is shown in fig. 5.1b. The OSC active layer of MD376/PCBM blend (~50 nm) is between two electrodes transparent ITO/PEDOT (anode) and Al/Ca (cathode). There PEDOT increases the efficiency of holes extraction.

We will use definitions *vac1:1, vac9:1, sol1:1* and *sol9:1* for vacuum and solution processes films with 1:1 and 9:1 MD376:fullerene weight ratios respectively.

The fluorescence spectra and fluorescence decay kinetics were measured with an Edinburgh Instruments fluorescence spectrometer F900. A diode lasers (EPL-375 and EPL-470) emitting 50 ps pulses at 375 and 470 nm with a repetition rate of 20 MHz were used for excitation. The average excitation power was about 150 $\mu W/mm^2$. The fluorescence spectra were corrected for the instrument sensitivity. The time resolution of the setup was about 100 ps if deconvolution with the instrument response function was applied. The electric field-induced fluorescence quenching was investigated by using the same equipment and applying a DC voltage to the sample during the measurements. Fluorescence kinetics was measured at the maximum of noncorrected for device sensitivity fluorescence band at 750 nm.

5.1 Excited states dynamics in solutions

Absorption spectra of merocyanine MD376 in solutions ($c=4 \cdot 10^{-6}$ mol/L, $\varepsilon=66400\ M^{-1}cm^{-1}$ (at 576 nm) are presented in Fig. 5.2. The absorption spectra of solutions in weakly polar solvent toluene ($\mu = 0.3D$, ET_{30} ~ 33.9 kJ/mol) show two clearly expressed absorption bands. The main absorption band (575 nm) corresponding to the $S_0 \rightarrow S_1$ transition is accompanied by a vibronic satellite roughly 142 meV higher in energy, typical of a C-N stretching mode. On the short wavelength side an additional absorption band (~ 475 nm) is observed. It is shifted by about 0.5 eV relative to the main transition, therefore it can not be related to a vibrational satellite. We attribute this transition to an electronic state above S_1. The energetic

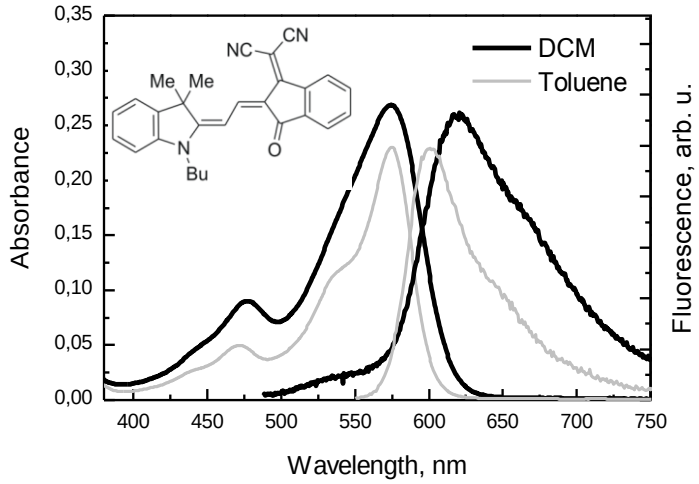

Fig. 5.2. Absorption (thick lines) and fluorescence (thin lines) spectra of MD376 in toluene (red) and DCM (black).

position of the absorption transition does not change if the more polar solvent dichloromethane (DCM, $\mu = 1.1D$, $ET_{30} \sim 40.7$ kJ/mol) is used. This seems a little surprising because MD376 molecules have large ground state dipole moment of 6.2 D. [127] However, the absorption band shows only some increased inhomogeneous broadening instead. All together it is conceivable that we observe absorption of monomeric MD376 in solution, otherwise the absorption would split into two transitions as observed for more polar merocyanines with changing solvent polarity. [92, 128]

Fig. 5.2 also shows fluorescence spectra of MD376 in toluene and DCM solutions at a concentration of 10^{-5} mol/L. In toluene the fluorescence band is red-shifted to the long wavelength side by about 100 meV relative to the absorption, which is a typical Stokes-shift for large organic molecules indicating that fluorescence originates from the same electronic transition as the lowest energy absorption band. It should be noted that fluorescence spectra of solutions are much more sensitive to solvent polarity: the fluorescence band shifts much more (160 meV) to the long wavelength side, becomes much broader and the intensity decreases in more polar solvent DCM. Altogether, this hints to an emitting state having more CT character. The MD376

fluorescence decays exponentially with about 300 ps time constant in toluene solution and with 600 ps time constant in DCM (not shown).

Transient absorption spectra of MD376 solution in DCM measured at various delay times are presented in Fig. 5.3.

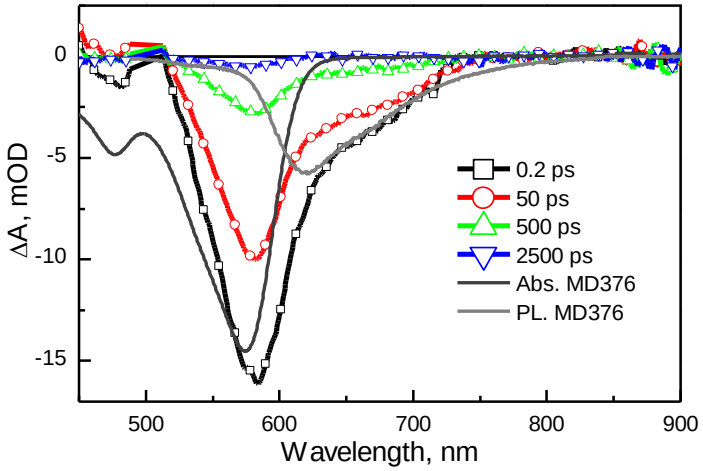

Fig. 5.3. Transient absorption spectra of MD376 in DCM at various delay times. The steady state absorption (black line) and PL spectrum (grey line) are shown for comparison.

The spectra show a negative band around 580 nm (0.2 ps), which closely resembles the sum of the absorption and fluorescence bands, thus it is caused by absorption bleaching and stimulated emission. The negative signal in the short wavelength absorption band region (ca. 500 nm, 0.2 ps) is weak, and even weak induced absorption appears at about 475 nm at longer delays (50 ps). Thus, excited state absorption apparently compensates absorption bleaching in this spectral region (450-520 nm). The transient absorption decays exponentially with about 600 ps time constant (not presented), coinciding with the fluorescence decay time and shows no evident spectral evolution. Consequently, it reveals *no dynamics* other than excited state decay, which indicates that no major changes of electronic or conformational structure of molecules take place in the excited state within picosecond to nanosecond timescales. On the other hand, relatively low contribution of stimulated emission hints at some conformational changes reducing transition dipole

moment, which take place faster than the time resolution of our setup (~130 fs).

5.2 Exciton dynamics in neat films

Absorption and fluorescence spectra. Freshly prepared neat MD376 films, have a main absorption band split into two bands (*A1* and *A2* in Fig. 5.4) of almost the same strength separated by about 160 meV.

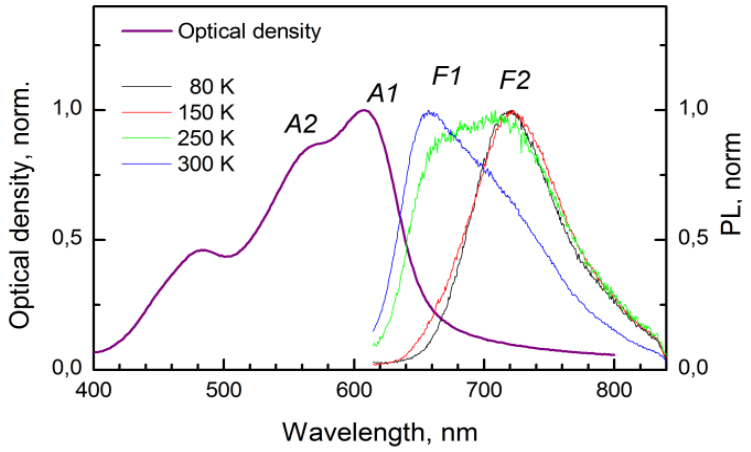

Fig. 5.4. Absorption spectrum and fluorescence spectra measured at indicated temperatures of neat MD376 film processed from chlorobenzene (CB) solution.

The first absorption band is located at 610 nm compared with 574 nm in solutions, i.e. red-shifted by 140 meV. The positions and relative intensities of both bands slightly depend on sample preparation. First of all, it should be noted, that the ratio between integrated intensities of the higher energy and the lower energy bands remains approximately the same in solutions and in films. It indicates that no new absorption bands appear in films, just a long wavelength band is split into two bands. The simplest interpretation of the absorption band splitting would be an assumption that the absorption band shifts to the long wavelength side by about 140 meV in comparison with solutions and the vibronic satellite gains intensity. Although, we cannot

completely rule out such a possibility, it is not very likely because position of the long wavelength absorption band is insensitive to the solvent polarity, therefore environment influence can hardly be so strong in solid state. Moreover the band splitting slightly varies in different samples, which is inconsistent with the vibrational origin. The two bands may be also attributed to different molecular species present in the films, for example, to aggregate or microcrystalline structures surrounded by amorphous material as it has been suggested for some conjugated polymers [129]. This is also unlikely because the two bands have very similar relative intensities in differently prepared samples, which would be surprising that relative concentrations of amorphous and aggregate structures would not be sensitive to sample preparation. We suggest that the absorption band splitting is caused by excitonic coupling as a result of formation of interacting dimers, aggregates, or microcrystallites. According to the excitonic theory [130], the absorption transition splits into two transitions if the aggregate structure is composed of two inequivalent molecules in the unit cell, i.e. molecules with different orientations of their transition dipole moments. The relative intensities of both bands depend on the mutual orientation of nonequivalent molecules, while the amount of splitting depends on the interaction energy. Therefore, relative band intensities and their positions may slightly vary depending on the molecular arrangement in aggregates. The arrangement of MD376 molecules in single crystals supports our assignment [92, 127]. Below we show that this attribution is also consistent with the transient absorption results.

On the other hand, the films are not completely ordered or crystalline, at least fraction of the material is expected to be amorphous. The absorption of amorphous material is apparently hidden under the high intensity bands of the aggregates. It should be noted that neat MD376 films are prone to crystallization; clearly visible polycrystalline structure appears in the films during a period of several weeks. It depends largely on solvent used: solvents of lower vapor pressure produce stable films, whereas solvents of higher vapor pressure tend to form films prone to crystallization. Aged crystallized films

have flattened spectra and slightly different peak positions. Band flattening is a natural consequence of formation of large crystallites nontransparent to light of any wavelength within absorption band region [131].

Fluorescence spectra of the MD376 films (Fig. 5.4) are composed of two main bands peaking at approximately 720 and 650 nm (1.72 and 1.9 eV), however their intensities, positions and widths vary significantly depending on the film preparation conditions, aging and particularly on temperature. The high energy fluorescence band (*F1)* at about 650 nm gains intensity upon aging of the sample, but disappears at low temperatures. Judging by typical Stokes shift, this band originates from the dominating aggregated species responsible for the lowest energy absorption band at 600-620 nm. The long wavelength fluorescence band (*F2*) at about 720 nm has very large Stokes shift, therefore it should be attributed to some minor structural species with low energy electronic states or to formation of new electronic states in the excited state inactive in absorption.

Zviterionic character of MD376 molecules suggests formation of low energy intermolecular charge transfer states upon some optimal arrangement of different fragments of neighboring molecules. Thus, these states are most likely responsible for the low energy fluorescence band. Hereafter, we label them as $CT_{M\text{-}M}$. Other explanations of the low energy fluorescence band such as molecular isomerization or intersystem crossing to triplet states can be ruled out because both fluorescence and transient absorption show no any signs of their formation in solutions. Moreover, triplet states are not consistent with the fast formation of the long wavelength band, as we will discuss below, and also with the fact that intensity of this band is not sensitive to the film exposure to oxygen.

The temperature dependence of relative intensities of the two bands approximately follows the occupation probability of the two states determined by a Boltzmann distribution. It indicates that excitations relax to the low energy excited states at low temperatures, while thermal activation repopulates the high energy excited states.

Fluorescence decay dynamics. Fluorescence dynamics of the neat films was measured in two time domains by means of a streak camera (ps domain) and by a TCSPC spectrometer (ns domain). Fig. 5.5 shows fluorescence kinetics of the neat film measured at the maxima of the two fluorescence bands.

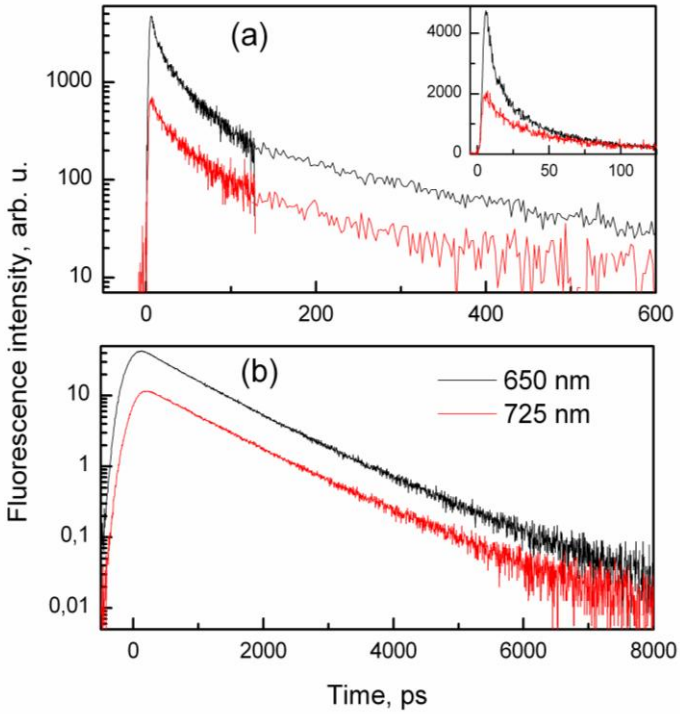

Fig. 5.5. Fluorescence decay kinetics of neat MD376 films at 650 and 725 nm measured by means of streak-camera (a) and TCSPC spectrometer (b). The insert shows the initial part of the kinetics on a linear scale normalized to equal amplitudes of the slow relaxation component.

Fluorescence intensity on a ns time scale investigated by a TCSPC spectrometer decays with about 550 ps time constant at both wavelengths at room temperature, and with about 3800 ps time constant at 725 nm at 80K (not presented). The fluorescence decay measured with a streak camera reveals an additional nonexponential fast decay. Fitting of the early time fluorescence decay with biexponential function gives additional relaxation components with decay time constants of 7 ps and 60 ps at 650 nm, and of 20 ps and 200 ps at 725 nm.

The fast decay component at 725 nm has lower relative contribution than at 650 nm and should be attributed to the tail of the short wavelength fluorescence band still present at 725 nm. The fluorescence intensity of *F1* band at 650 nm decays approximately 100 times during this fast relaxation phase, which lasts for about 200-300 ps until fluorescence reaches the slow, independent of detection wavelength decay phase. It indicates that population of the S_1 state decreases about 100 times, when excitations relax to $CT_{M\text{-}M}$ states. Assuming that only the high energy states are initially optically excited and total density of excitations decays much slower than excitations relax to the low energy states, we obtain that about 1% of excitations remain on the high energy states after the thermalization process, while remaining 99% relax to the low energy $CT_{M\text{-}M}$ states. On the other hand, after thermalization, relative populations of high (n_1) and low (n_2) energy states should be determined by a Boltzmann distribution: $n_1/n_2 = (\rho_1/\rho_2)\exp(-\Delta E/kT)$, where ρ_1/ρ_2 determines relative densities of high and low energy states and ΔE is the energy difference between the two states of about 0.2 eV. This energy difference gives that occupation probabilities of the two states must differ by about 3000 times ($\exp(-\Delta E/kT) = 1/3000$). Taking into account that the fluorescence intensity drops down about 100 times, we obtain relative densities of states $\rho_1/\rho_2 = 30$. Thus, this estimation gives that the density of the low energy $CT_{M\text{-}M}$ states is about 3% of the total density of molecules. This estimation is in a reasonable agreement with the tens of ps exciton trapping time. As we will show below, 10% of PCBM causes several times faster fluorescence quenching. However, apparently the density of the $CT_{M\text{-}M}$ states strongly depends on the sample preparation conditions and aging causing significant variation of the fluorescence spectra, thus this estimation shall be considered only as a rough estimate.

Fig. 5.6 shows the energy scheme for neat MD376 films based on the above presented experimental data.

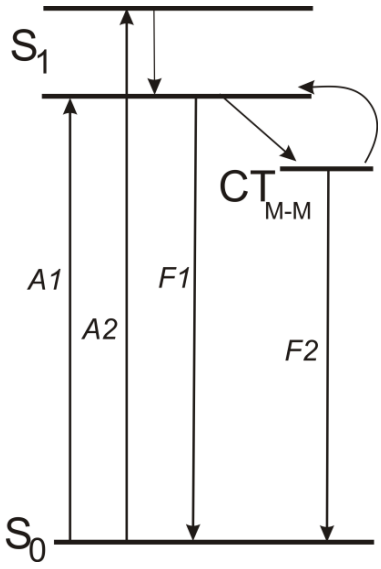

Fig. 5.6. Energy level scheme of neat MD376 films. S_1 shows two excitonically splited excited singlet states responsible for A1 and A2 absorption bands and CT_{M-M} shows the intermolecular charge transfer state. Singlet excitons relax to the CT_{M-M} , however subsequently the lower energy singlet state is thermally repopulated.

Transient absorption of neat MD376 films. Several samples of neat MD376 films prepared from MD376 solutions in different solvents have been investigated. Despite strong variation of absorption and particularly fluorescence spectra of different films, the transient absorption spectra were quite similar. Fig. 5.7 shows the transient absorption spectra at various delay times for the film processed from chlorbenzene solution obtained under excitation intensity of 60 $\mu J/cm^2$ per pulse.

At zero delay time, the transient absorption spectrum reveals bleaching of the absorption spectrum (500 - 650 nm) partly compensated by the excited state absorption. The negative signal at $\lambda > 650$ nm is attributable to the stimulated emission since steady state absorption and consequently absorption bleaching are almost absent in this spectral region.

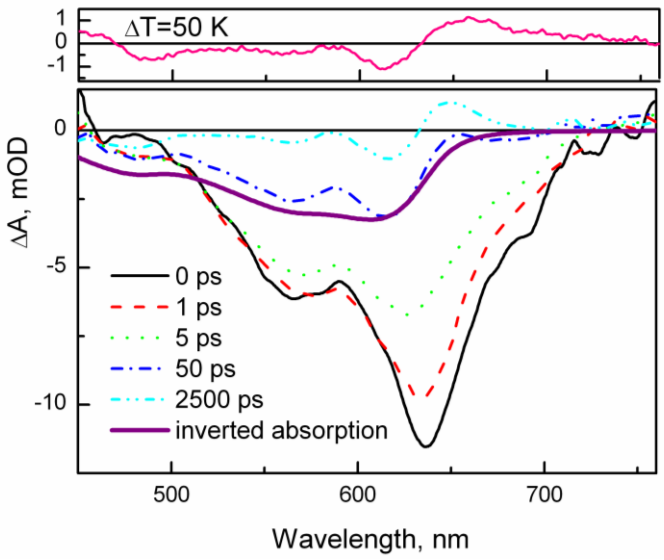

Fig. 5.7. Transient absorption spectra of a neat MD376 film at various delay times. The solid purple line shows inverted absorption spectrum of the film. The spectrum on top shows the absorbance changes induced by the sample heating by 50 K.

Evolution of the transient absorption of films is more complex in comparison with solutions. The intensity of the long wavelength part (> 630 nm) of the negative band significantly decays within 50 ps, while the short wavelength part (~ 570 nm) of the absorption bleaching band decays much slower remaining almost constant up to 5 ps. Fig. 5.8 shows the transient absorption kinetics at various wavelength probing the different energies, i.e. 550 nm, 580 nm, 640 nm and 700 nm measured at low excitation intensity of 24 μJ/cm^2 when nonlinear relaxation processes play no essential role (see below).

The kinetics at 640 nm is much faster than at other wavelengths during initial 50 ps supporting its attribution to the stimulated emission related to the *F1* fluorescence band, which shows identical relaxation kinetics. Transient absorption relaxation becomes identical at all wavelengths when excitation trapping to $CT_{M\text{-}M}$ states terminates at about 50 ps.

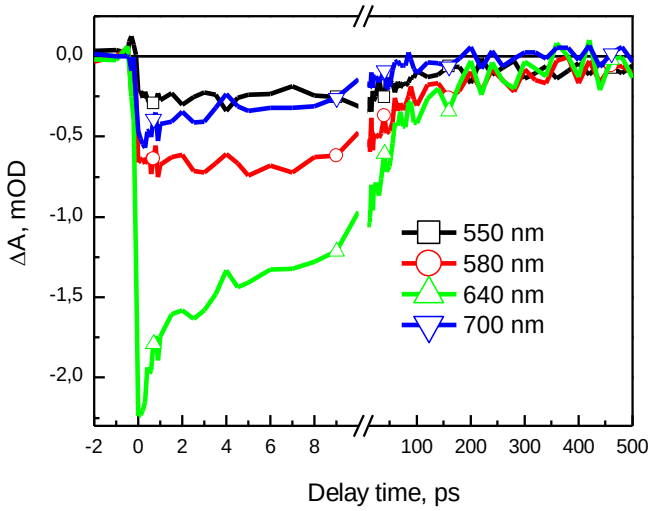

Fig. 5.8. Transient absorption kinetics at various probe wavelengths for the neat MD376 film, measure at 24 μ J/cm^2 per pulse excitation intensity.

The transient absorption decay also reveals a subpicocecond relaxation process, which was not observed in fluorescence experiments due to the limited time resolution of about 3 ps of the streak-camera. Once the stimulated emission decays, the transient absorption spectrum is almost identical to the inverted absorption spectrum (Fig. 5.6 thick line). It shows that the majority of the molecules remain in the excited state, while only loosing the stimulated emission property, in agreement with relaxation to the weakly fluorescent low energy state as discussed above. Surprisingly, absorption bleaching experiences no changes during this process. It unambiguously shows that the low energy sites, dominantly occupied after the relaxation process, have an absorption spectrum identical or very similar to that of major molecular species, which were initially excited. The only difference is that the low energy species show no stimulated emission and their fluorescence spectrum is shifted to the long wavelength side (Fig. 5.4). These properties are consistent with the charge transfer (CT) character of the low energy states where electron transfer between differently charged fragments of neighboring molecules takes place in the excited state. Such CT states are very common in molecular solids composed of polar molecules. CT states usually have small oscillator strength,

thus the absence of the stimulated emission is a natural consequence of the CT state formation. The CT_{M-M} states are most probably formed between MD376 molecule pairs having some particular mutual arrangement, supported by the single crystal structure [127]. These molecular pairs may be excited directly, however, more likely they are dominantly excited during exciton migration determining tens of picoseconds relaxation component of the *F1* fluorescence band. Even a small difference in the CT_{M-M} state energy caused by some variations of arrangement of molecular pairs may cause significant differences in relative populations of Frenkel and CT_{M-M} exciton states. Morphology differences may also cause differences in CT_{M-M} state oscillator strength. Thus, these factors evidently cause strong sensitivity of the fluorescence spectra to the sample morphology.

The shape of the transient absorption spectrum changes dramatically at 2500 ps delay time: a new induced absorption band appears at the long wavelength absorption band slope (630 - 670 nm). We assign this spectrum to the absorbance changes induced by the local heating of the film following optical excitation. In order to support this assignment we have measured the changes of the steady state absorption spectrum upon sample heating. The sample was heated to 80° C and cooled down to room temperature several times. The spectrum experienced almost reversible changes, which in the 500-700 nm region were very similar to the transient absorption spectrum measured at 2500 ps (see Fig. 5.7). The values of the thermally and optically induced absorbance changes were also in a good agreement with the local heating values estimated assuming typical heat capacity of organic solids of 0.5 $cal \cdot g^{-1}K^{-1}$. It should be noted that the local heating contribution does not disappear by reducing the excitation intensity; its intensity decreases approximately proportionally to the transient absorption intensity at zero delay time. This is due to the fact that almost all absorbed excitation energy is converted to the thermal energy within about 1 ns after excitation, while thermal energy transfer to the glass substrate is much slower.

The transient absorption relaxation at all probe wavelengths becomes progressively faster with increasing excitation intensity. Fig. 5.9 shows kinetics at 630 nm where the fast relaxation component is almost absent at low intensity.

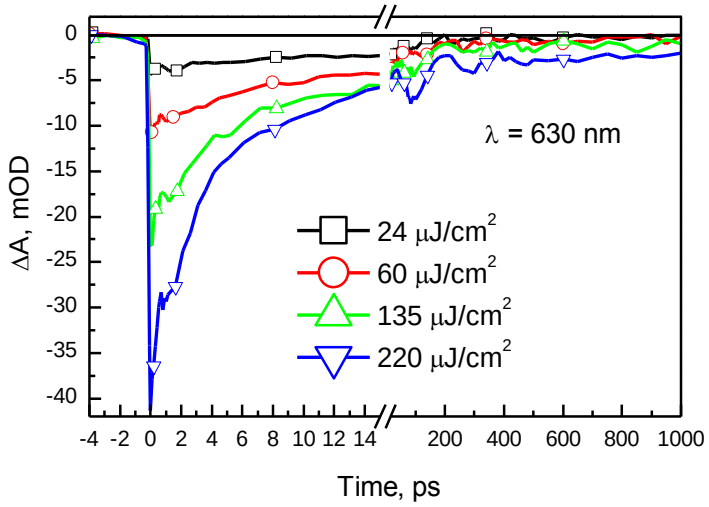

Fig. 5.9. Transient absorption kinetics at 630 nm for the neat MD376 film measured at various excitation intensities. Oscillations observed on a long time scale at high excitation intensities are due to the generation of acoustic waves.

It indicates that exciton-exciton annihilation, common in molecular solids, shortens the excited state lifetime at high excitation intensities. It is interesting to note that, oscillating features become clearly observable at high excitation intensities for times > 100 ps. The oscillations are particularly strong at the long wavelength slope of the absorption band, and may be unambiguously attributed to acoustic oscillations induced by local heating, which were observed in thin films of other organic materials [132]. Strong oscillations in MD376 films indicate that the long wavelength absorption band is very sensitive to the density of the material. In agreement with the excitonic splitting, the long wavelength absorption band shifts towards the long wavelength side when intermolecular interactions increase due to decreasing intermolecular distances.

We have also investigated dependence of the transient absorption on excitation wavelength (not shown). No clear difference of spectra and their evolution was observed under excitation of the films at 500, 550, and 610 nm, corresponding to different absorption peaks. It supports the assumption that all three absorption bands belong to the same molecular species.

5.3 Ultrafast processes in blends

5.3.1 Exciton dynamics

Absorption spectra of blends correspond to the sum of MD376 and PCBM absorption spectra (see Fig. 5.10).

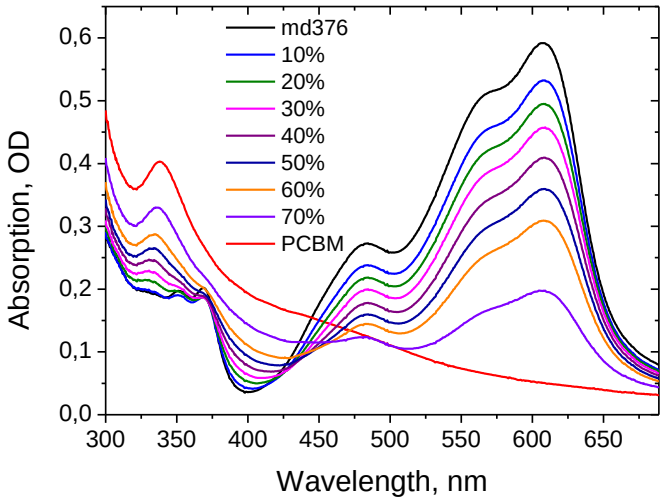

Fig. 5.10. Absorption spectra of MD376:PCBM blend films with different concentrations of PCBM.

Absorbance of the films at long wavelength, where PCBM absorption is weak, is approximately proportional to the concentration of MD376, while PCBM absorption dominates in the short wavelength region. We do not observe any new bands, which could be related to formation of MD376/PCBM complexes.

Addition of PCBM causes strong quenching of the MD376 fluorescence and appearance of a new low energy fluorescence band *F3* with maximum at

about 740 nm (see Fig. 5.11), which is only slightly red-shifted and broader than *F2* band (see Fig. 5.4).

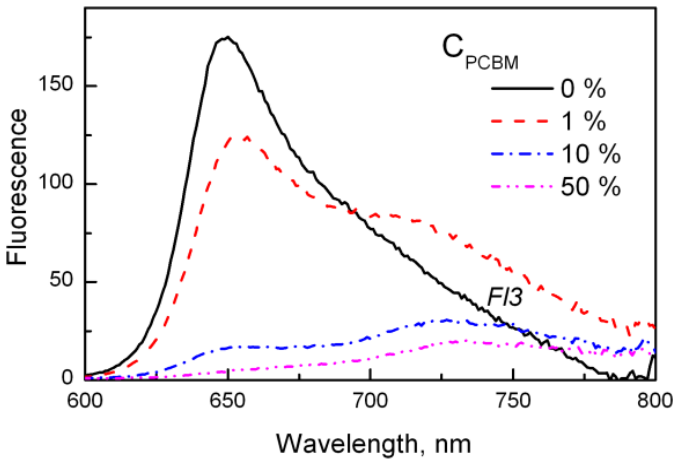

Fig. 5.11. Fluorescence spectra of MD376:PCBM blend films with different PCBM concentrations.

Even 1% of PCBM quenches the *F1* fluorescence band by about 30%. MD376 fluorescence intensity drastically drops down at higher PCBM concentrations, and interestingly, intensity of the *F3* fluorescence band drops down as well.

Fluorescence decay kinetics at 650 and 725 nm for blend films are presented in Fig. 5.12. Fluorescence of MD376 at 650 nm in the blend with 10% PCBM dominantly decays within about 20 ps. At 50 % PCBM concentration, the decay at 650 nm is limited by the resolution time of the streak-camera (~ 3 ps). Kinetics on a ns time scale shows that the *F1* band was not completely quenched on a ps time scale but has also a slowly relaxing component, which was not observed with streak camera because of lower sensitivity. Decay kinetics at 725 nm has an identical fast decay component,

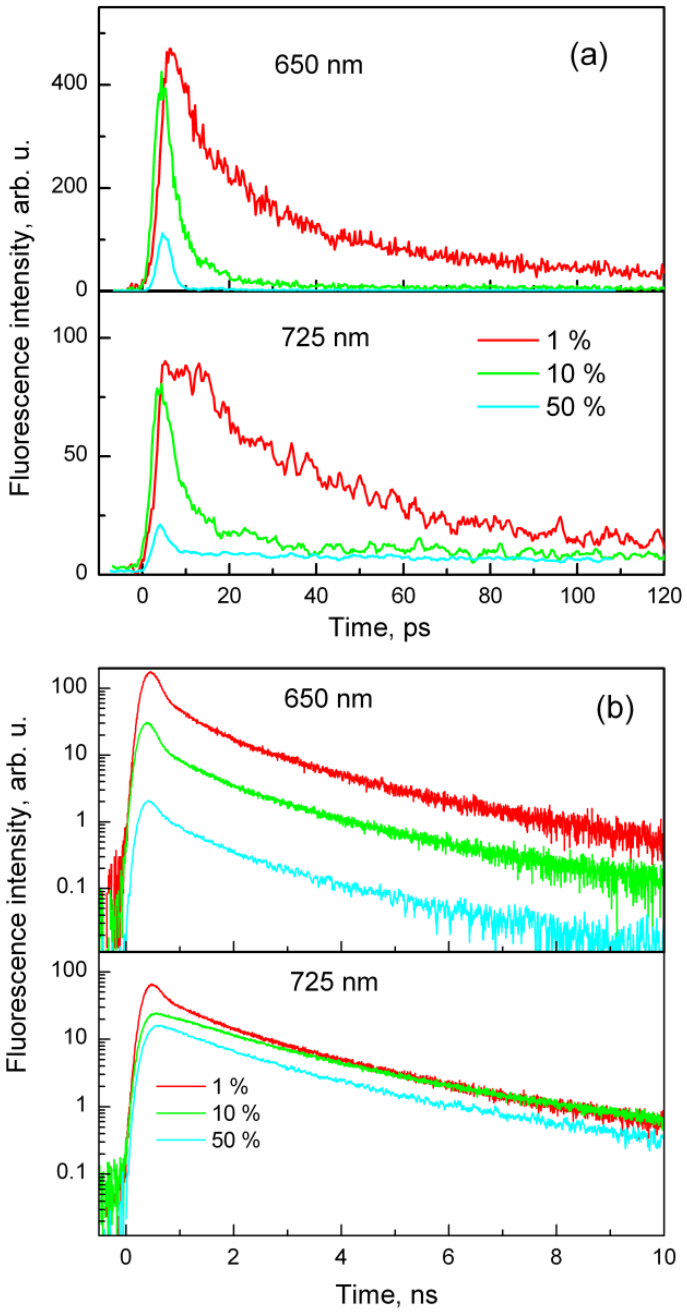

Fig. 5.12. Fluorescence decay kinetics in MD376:PCBM blend films with different PCBM concentrations measured at 650 and 725 nm by means of streak-camera (a) and TCSPC spectrometer (b).

which, should be also attributed to the MD376 fluorescence band tail. Fluorescence at 725 nm has also a slow relaxation component, which is stronger than at 650 nm and therefore was also observed with streak camera. Fluorescence at both detection wavelengths decays almost identically on a ns

time scale, weakly depends on PCBM concentration and may be characterized by about 1 ns (46%) and 3 ns (54%) decay time constants. These decay times are much longer than fluorescence decay time in neat film of about 550 ps, thus confirm attribution of the slowly relaxing fluorescence component to a new *F3* band formed in blends.

Conventionally, quenching of the inherent material (i.e. MD376) fluorescence by acceptors such as PCBM is due to three main processes: a) energy transfer from donor to the acceptor, b) electron transfer from the donor to the acceptor, and c) to formation of complexes between donor and acceptor and energy transfer to these complexes. Consequently, the new fluorescence band *F3* may be attributed to fluorescence of new states, probably of CT origin, formed between MD376 and PCBM. This has been observed many times for conjugated polymer/PCBM blends [106, 107, 133]. Fluorescence of PCBM can be ruled out, since PCBM fluorescence peaks at about 1.7 eV with a rather narrow half width and decays with time constants of about 0.7 ns (58%) and 1.4 ns (42%) [134]. The *F3* band of MD376/PCBM blend peaks at slightly lower energy, is much broader, and decays about two times slower. Moreover our recent investigations revealed that *F3* band is very efficiently quenched by electric field and the quenching efficiency closely correlates with photocurrent [135]. Therefore we attribute *F3* to CT_{M-F} states formed between MD376 and PCBM. A ten-fold decrease of the *F1* fluorescence band intensity in the film with 10% PCBM concentration shows that quenching of MD376 fluorescence in the film takes place with about 90% efficiency. Thus, only a minor increase of the CT_{M-F} state formation is expected at higher concentrations. At high PCBM concentrations other factors are likely to reduce CT_{M-F} fluorescence intensity. One of them is free charge carrier generation, competing with formation of fluorescing CT_{M-F} states or causing their quenching [106, 133, 136]. The carrier generation/collection efficiency is higher at high PCBM concentration when PCBM clusters are formed as was demonstrated for polymer:PCBM blends [106, 114, 136–138]. On the other hand, an identical slow relaxation component observed at 650 nm and 725 nm

detection wavelength is most likely due to thermal repopulation of S_1 states of MD376 in analogy with repopulation of these states from CT_{M-M} states in neat MD376 films. It causes not complete quenching of the *F1* fluorescence band and shows that a small energy difference between S_1 and CT_{M-F} states is not sufficient to completely prevent electron back transfer from PCBM to MD376.

Fig. 5.13 shows transient absorption spectra of solution processed blends with 10 % and 50% PCBM concentrations.

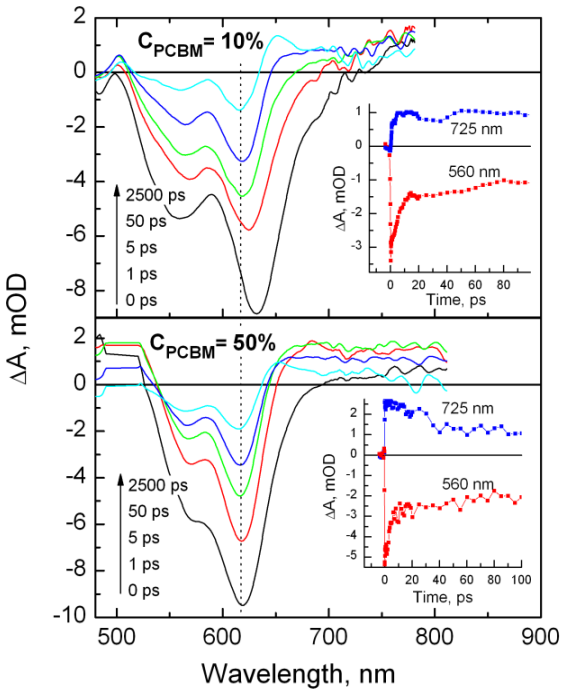

Fig. 5.13. Transient absorption spectra of MD376/PCBM blend films with 10:1 and 1:1 concentration ratios at various delay times. Inserts show transient absorption kinetics at 560 nm and 725 nm corresponding to absorption bleaching of MD376 dyes and absorption of CT_{M-F} states respectively.

The initial spectrum of the 10% PCBM film is identical to that obtained in neat films. This similarity is quite predictable, because PCBM weakly absorbs at the excitation wavelength, thus most of MD376 molecules are excited directly. Subsequent evolution of the transient absorption spectrum is also qualitatively similar to that of neat films, however the stimulated emission decays significantly faster, in agreement with the fluorescence decay, and a

new induced absorption band appears in the 650-750 nm region (compare Fig. 5.7). This band should be attributed to the CT_{M-F} states observed in fluorescence spectra. Similar near IR absorption has been observed in P3HT/PCBM blends and attributed to the Coulombically bound charge transfer states or to free charge carriers [114, 139]. Decay of the stimulated emission gives an estimate of the CT_{M-F} state formation rate of several ps.

Transient absorption spectra of the film with 50% PCBM (see Fig. 5.13) show no stimulated emission even at zero delay time: the maximum of the absorption bleaching band coincides with the long wavelength steady state absorption band and the negative signal in the fluorescence band region is absent. It indicates that quenching of the MD376 excited states and formation of CT_{M-F} states or free charge carriers is very fast at high PCBM concentration, faster than the resolution time of our setup of about 130 fs. Similar ultrafast energy transfer and charge carrier generation has been observed in conjugated-polymer/PCBM films [114, 139]. The long wavelength induced absorption (650-750 nm) attributed to the CT_{M-F} states is initially about two times stronger in film with 50% PCBM than in film with 10% PCBM, however, it partly decays during tens of ps (see insert in Fig. 5.13). On the other hand, the absorption bleaching decays very similarly in both films. We conclude that in films with 50% PCBM a fraction of molecular species absorbing in the 700 nm region are converted to nonabsorbing species during tens of ps. Combining this property with the quenching of the CT_{M-F} fluorescence at high PCBM concentration we attribute the induced absorption to the CT_{M-F} states, which are partly quenched by the free charge carrier generation in the films with high PCBM concentration. This attribution is based on the assumption that free charge carriers do not absorb in the visible spectral region. Indeed, PCBM anion radicals do not absorb in the visible spectral region [140]. MD376 radical cations prepared by chemical oxidation have a wide absorption band in the near IR region (see Fig. 5.14), however, the intensity of this band is about 30 times lower than intensity of the visible absorption band of neutral

molecules, therefore its intensity in the transient absorption spectra should be very low.

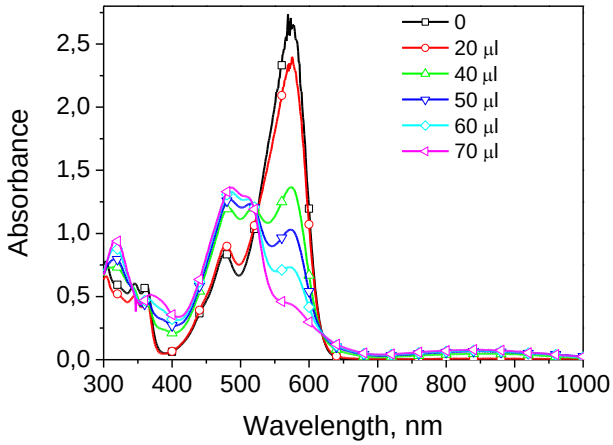

Fig. 5.14. Absorption spectra of MD376 cations in DCM obtained by chemical oxidation using indicated volumes of saturated $FeCl_3$ solution. The concentration of the MD376 solution is ~$4 \cdot 10^{-4}$ mol/L in a 0.1 cm cuvette.

Based on the investigation results we propose the energy state model presented in Fig. 5.15 for MD376:PCBM blends.

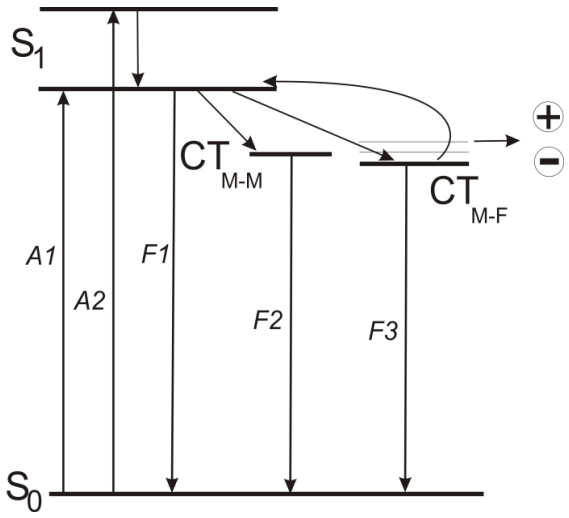

Fig. 5.15. Excited state relaxation scheme in neat MD376 film blend with PCBM. Optically created S_1 excitations form intermolecular CT_{M-M} or interphase CT_{M-F} states during several ps, however thermal reactivation causes a weak population of S_1 state during entire lifetime of CT_{M-F} state. Generation of separated charge carriers from unrelaxed CT_{M-F} state at high PCBM concentrations causes reduction of CT_{M-F} and S_1 state population.

The main finding is the formation of a charge transfer state CT_{M-F} below the CT_{M-M}, already present in pure MD376 films. Because of similar energies and, thus, similar fluorescence spectra we cannot clearly distinguish between CT_{M-M} and CT_{M-F} states in blends. However, there are some indications, that formation of CT_{M-F} states dominate, at least in blends with high PCBM concentration: much faster quenching of the *F1* fluorescence band and of the related stimulated emission in blends show that formation of CT_{M-F} states is much faster than formation of CT_{M-M} states in pure MD379, several times longer fluorescence relaxation time in blends indicates that it is determined by CT_{M-F} states absent in pure material. The prevalent role of CT_{M-F} states for the photophysics of blends is evidently mainly caused by a higher density of CT_{M-F} states rather than by their lower energy. Thus, most likely CT_{M-M} states do not play important role in charge carrier generation in MD376:PCBM blends and consequently in solar cells fabricated from these blends.

5.3.2 Fluorescence quenching

Time-integrated fluorescence spectra of MD376 blends with 50% and 10% fullerene prepared by vacuum deposition and by spin casting from solutions are presented in Fig. 5.16.

The fluorescence band at about 650 nm is attributed to MD376, while the strong band at long wavelengths is attributed to the CT excitons formed at MD376/fullerene interface. Similar CT exciton emission has been reported for a number of polymer:fullerene blends [39, 106, 107, 141, 142]. The shape and

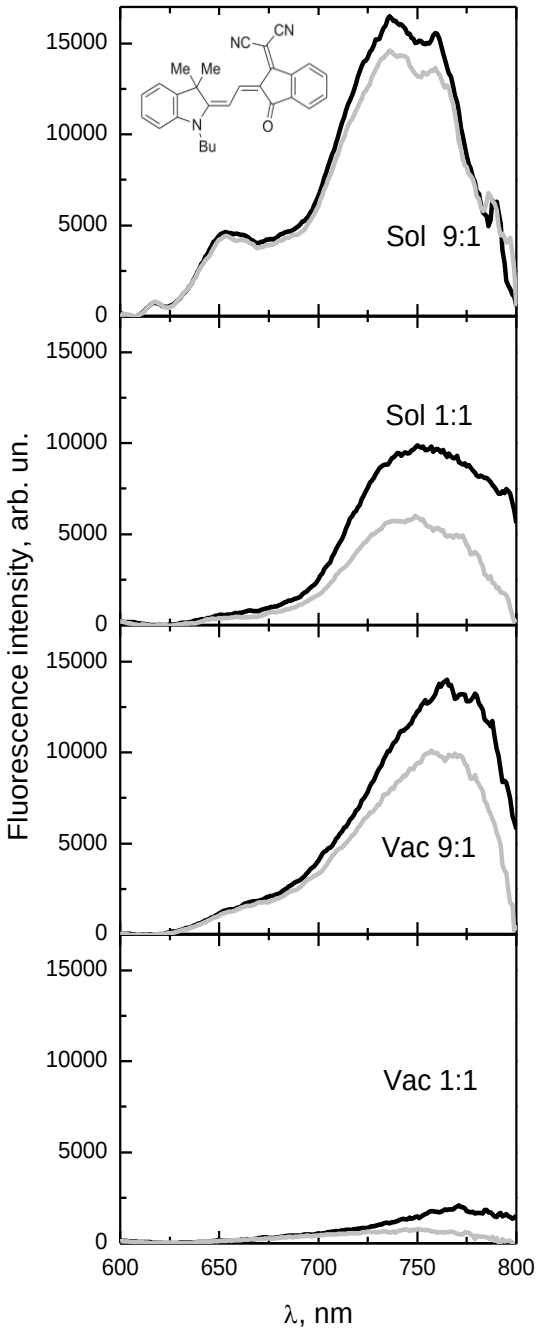

Fig. 5.16. Fluorescence spectra of various samples at 0 V (black) and 2V (gray) of applied voltages excited at 470 nm. The spectra are corrected for the spectrometer sensitivity and sample absorbance at excitation wavelength.

position of the CT fluorescence band vary slightly depending on the fullerene concentration and on the film fabrication method. The fullerene additives quench the intrinsic merocyanine fluorescence band at 650 nm. The quenching is stronger for vacuum deposited films and its efficiency increases with

fullerene concentration. The quenching efficiency apparently depends on mean dimensions of pure MD376 domains, which are smaller in the samples with higher PCBM content, and probably are also smaller in vacuum deposited films because of more homogeneous fullerene distribution. Interestingly, intensity of the CT fluorescence band also decreases by increasing fullerene concentration from 10% to 50%. We attributed this decrease to formation of additional CT exciton decay channel related to their dissociation into separated charge carriers at high fullerene concentration [143]. Similar CT fluorescence decrease at high PCBM concentration was also observed for the polymer:PCBM blend and was also attributed to the formation of separated charge carriers which eventually recombine nonradiatively [106].

The CT fluorescence of *sol9:1* and *sol1:1* films decays nonexponentialy and almost identically (see inserts in Fig. 5.17). However, the decay of the *vac9:1* film fluorescence is slightly faster, and is particularly fast for *vac1:1* film. Identical decay kinetics for *sol9:1* and *sol1:1* films lead to conclusion that radiative and nonradiative relaxation rates of CT excitons are independent of the PCBM concentration; it is very unlikely that variation of the radiative relaxation rates could be perfectly compensated by opposite variation of the nonradiative relaxation. Therefore different initial intensities should be attributed to different CT exciton concentrations. On the other hand, identical initial fluoresce intensities of the *sol9:1* and *vac9:1* films suggest that initial CT exciton concentrations and radiative relaxation rates in these films are also identical. Therefore, the weaker by about 20% integrated fluorescence of the *vac9:1* film and its faster decay should be attributed to faster nonradiative relaxation. Consequently, very low initial intensity of CT fluorescence and its fast decay in *vac1:1* film are apparently caused by low initial CT exciton concentration and by its fast nonradiative decay. These considerations lead to the conclusion that the radiative decay rates of the CT excitons are identical in all the samples and thus, CT fluorescence intensity faithfully represents the concentration of CT excitons.

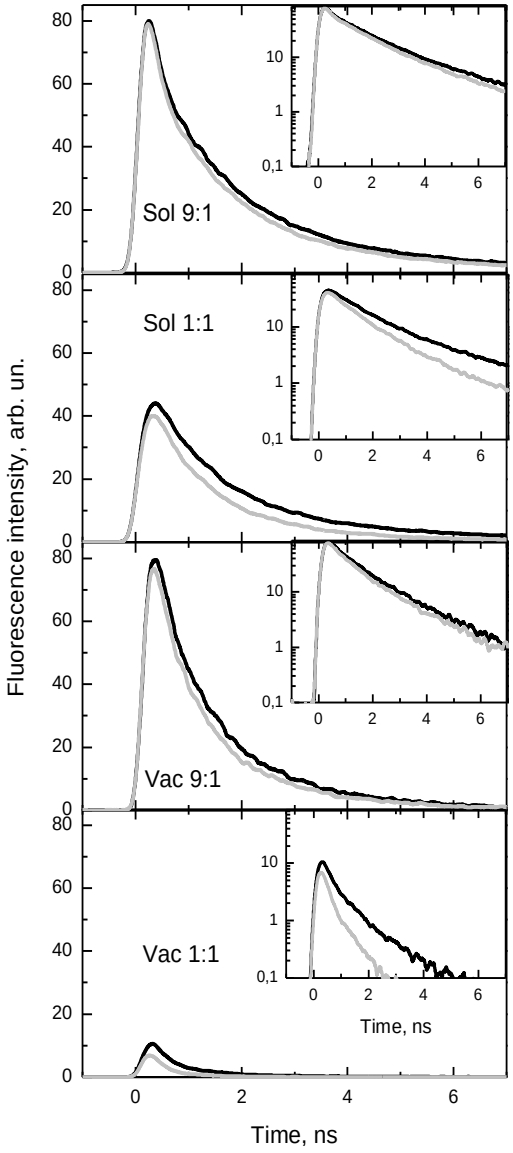

Fig. 5.17. Fluorescence decay kinetics of different blend films at 750 nm measured without electric field (black) and at 2V of applied voltage (grey).

Electric field strongly quenches the CT fluorescence, while quenching of the intrinsic MD376 fluorescence band at 650 nm is absent or much weaker (Fig. 1). This is consistent with the different origin of the two fluorescence bands. The field-induced fluorescence quenching of organic materials usually comes from dissociation of excitons into charge pairs [144], therefore quenching of Frenkel excitons having large binding energies of about (0.4-1) eV is significant only at field strengths of about 10^6 V/cm or higher [50, 145]. Moreover, Frenkel excitons, as discussed above, have short lifetime in blends,

therefore their field-induced quenching must be extremely fast to compete with the exciton splitting at MD376/fullerene interfaces. Binding energies of the CT excitons are several times as low, of about 0.2-03 eV [146], therefore they are easier to separate by electric field.

As it is clearly seen in Fig. 5.17, applied field has different influence on the fluorescence decay dynamics for different samples. It should be also noted that, the initial fluorescence intensity only weakly depends on the applied electric field. Deconvolution of the apparatus functions (not presented) supports the assumption that even for *vac1:1* film this field influence comes mainly from the reduced fluorescence lifetime rather than from reduced initial amplitude. It indicates that efficiency of the CT exciton formation is independent or only weakly dependant on the electric field. We can formally describe the CT exciton concentration (N_{CT}) dynamics under applied field as:

$$\frac{dN_{CT}}{dt} = -N_{CT}k\ (t) - N_{CT}q(V,t)\,, \qquad 5.1$$

where *k(t)* and *q(V,t)* are the intrinsic decay and fluorescence quenching rates respectively. Assuming that CT fluorescence intensity is proportional to N_{CT}, we can estimate the field-induced CT exciton quenching rates from the fluorescence decay kinetics as [101]:

$$q(t,V) = \frac{1}{F_0}\frac{dF_0}{dt} - \frac{1}{F_V}\frac{dF_V}{dt}\,, \qquad 5.2$$

where $F_0(t)$ and $F_V(t)$ are time dependent fluorescence intensities without and with the electric field, respectively. The evaluated CT exciton quenching rates are presented in Fig. 5.18.

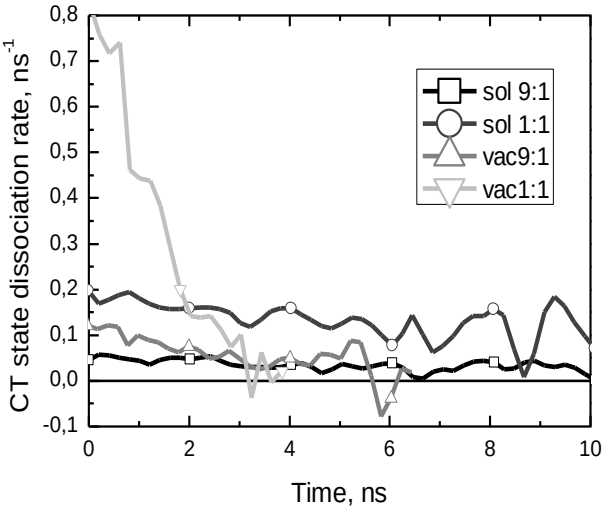

Fig. 5.18. Electric field-induced time-dependent CT exciton quenching rates in various samples at 2 V of applied voltage.

The highest initial quenching rate was obtained for the *vac1:1* film. However, it rapidly decreases, simultaneously with the decay of the fluorescence intensity approaching that of the *vac9:1* film at longer (>3ns) times. This behaviour tells us about the inhomogeneity of the CT excitons; rapidly relaxing CT excitons are easily quenched, while quenching of the long-living CT excitons is much less efficient. The long-lived and inefficiently quenched CT excitons are most probably those created at small fullerene domains, which dominate in *vac9:1* film and are also present in *vac1:1* film. These excitons start to dominate in *vac1:1* film at long times when rapidly relaxing excitons already decay, and cause similar low quenching rates both for *vac1:1* and for *vac9:1* films. Fluorescence quenching in solution processed films shows qualitatively similar dependence on the PCBM concentration, but no clear time dependence. Thus, comparison of the CT fluorescence intensities, their relaxation and quenching rates in different samples allows us to conclude that CT excitons in blends decay in two phases: ultrafast phase, much faster than the time resolution of our measurements, causing decrease of the initial fluorescence intensity and their decay on a ns time scale. Electric field causes

shortening of the ns lifetimes, while its influence on the ultrafast decay phase is absent or weak.

5.3.3 Charge carrier transport

We combine ultrafast TREFISH and conventional time-resolved photocurrent measurements to get information on carrier motion from their generation until extraction from the samples. Fig. 5.19a. shows the electric field kinetics in the investigated blends calculated from the time-resolved EFISH data (initial 3 ns) as described in the experimental section, and from the voltage kinetics measured by the oscilloscope at longer times.

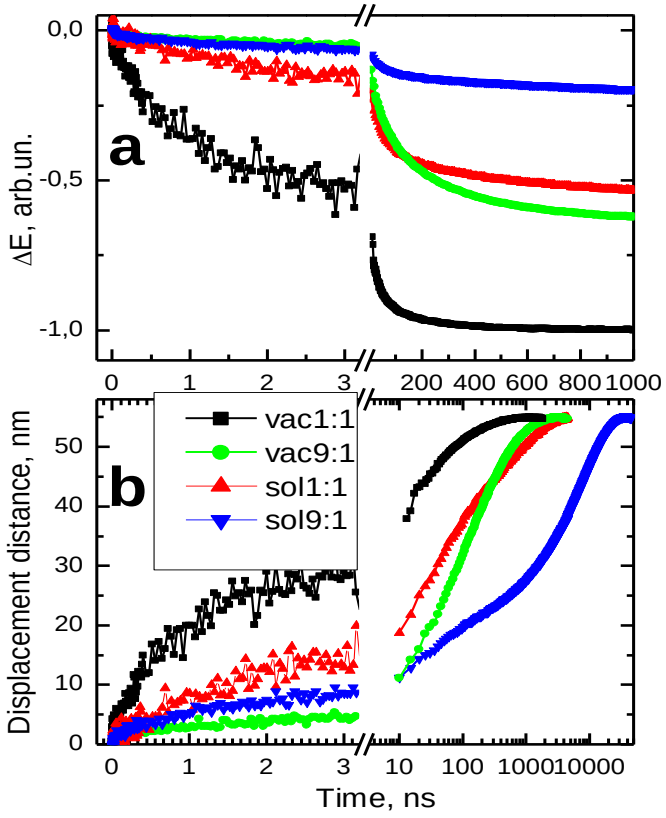

Fig. 5.19. **a)** Electric field kinetics at 2 V applied voltage in the investigated blends calculated from the time resolved EFISH data and from voltage kinetics measured by oscilloscope. **b)** Carrier displacement kinetics at 2 V applied voltage (note log scale after break).

The kinetics obtained for the *vac1:1* film shows the fast electric field decrease on the time domain of initial 3 ns. Approximately half of the total field decrease takes place during this time, while the remaining field decay is much slower, taking place on tens and hundreds of ns time scale. The electric field kinetics in *vac9:1* film is significantly different. It shows only a minor field decrease measured with TREFISH method, while the dominating field decrease takes place on tens and hundreds of ns time scale reaching saturation at about 10 μs. The total field decrease is by about 30% smaller in *vac9:1* film than in *vac1:1* film. The field kinetics in *sol1:1* film is qualitatively similar to that obtained for the *vac1:1* film, but the field decrease during initial 3 ns is several times smaller, the second decrease phase lasts much longer, and the total field decrease is smaller by about 40%. The filed kinetics in *sol9:1* film is almost identical to that in *vac9:1* film during initial 3 ns, while the total field decrease is slightly smaller.

Different electric field kinetics obtained in different samples should be related to different electron and hole motion and extraction dynamics. Electron mobilities are expected to be very different in samples with different fullerene content. The electron mobility is expected be low in samples with 10% fullerene concentration, which is below or close to the percolation threshold, being, e.g. at about 18%. for spherical particles. Electron mobility in microcrystalline PCBM powder or films was reported to be up to 0.1 $cm^2 V^{-1} s^{-1}$ [147, 148]. Since we observe fast electric field decrease in samples with high fullerene concentration and much slower in samples with low concentration, we attribute the fast decrease phase to the electron motion in percolating fullerene domains. Field decrease by about 50% of the total decrease value during the initial 3 ns in *vac1:1* and its clear saturation suggest that all electrons are extracted from this sample during 3 ns, while hole extraction is consequently much slower, lasting for hundreds of ns. Electron motion in other samples is much slower, and only fraction of them are extracted during 3 ns. Slow electron extraction from samples with 10% fullerene is a natural consequence of low electron mobility due to weak percolation of PCBM

domains. Slower electron motion in the solution processed film *sol1:1* is most probably related to lower carrier mobility in PCBM in comparison with fullerene [149]. This is plausible because attached side groups in PCBM molecules disrupt the optimal packing of fullerene buckyballs and slow down electron transport. Different morphology of solution processed and vacuum deposited films may be another reason for different carrier mobility. Slow carrier generation, as will be discussed below, is an additional factor limiting carrier extraction from some of the samples during initial several ns.

The hole mobility is expected to be less sensitive to the fullerene content because merocyanine concentration is sufficiently high in all the samples to reach its percolation threshold. Thus, the hole motion is expected to be similar in all samples. Indeed, on a 10-150 ns time domain, electric field dynamics is similar for all the samples (see fig. 5.19a). Thus, the field kinetics on the tens of ns time scale we attribute to the hole extraction. This phase terminates carrier extraction from *vac1:1* film. Carrier extraction from *sol1:1* film has about ten times slower component in addition. Most probably this extraction phase is caused by the trapped carriers. Apparently, solution processing produces deep carrier traps. However it is difficult to discriminate, which, electrons or holes are trapped.

The final carrier extraction phase is particularly slow for the *sol9:1* film. We do not see any reasons why hole extraction from *sol9:1* film may be much slower than form other samples, therefore we attribute the slow phase to the slow electron extraction via nonpercolating fullerene domains. Fig. 5.20 shows the voltage kinetics measured with oscilloscope at different applied voltages for *sol9:1* film.

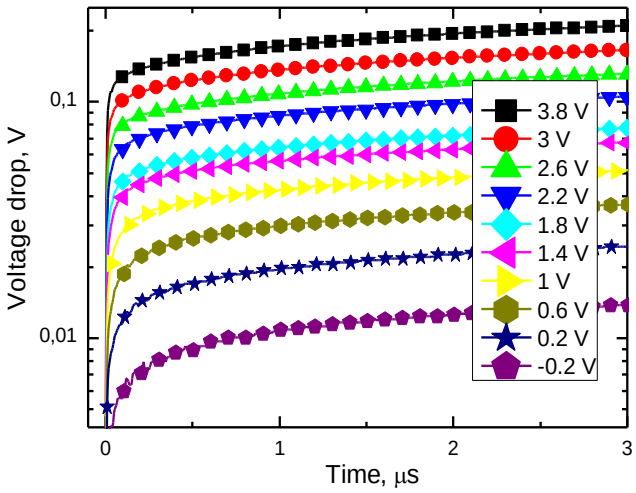

Fig. 5.20. Excitation induced voltage kinetics in *sol9:1* film at various applied voltages.

The initial extraction phase is faster at higher applied voltages because of faster carrier motion, while the shape of the slow extraction component, is surprisingly insensitive to the applied voltage. Such behaviour is incompatible with carrier motion governed by their mobility. Evidently the mobility concept is not applicable to this extraction phase. More likely it is governed by the carrier de-traping. In samples where percolative passage for electrons is absent, electrons must be transferred from fullerene to MD376 in order to be extracted, i.e. electrons must be thermally activated from fullerene LUMO orbital to LUMO of MD376, which is by about 250 meV higher in energy [48]. This large energy difference makes the process very slow and electric field influence on its rate appears to be insignificant. It causes the observed their slow extraction from *sol9:1* film. Surprisingly the electron extraction from the *vac9:1* film is much faster than from *sol9:1* film. The difference is most probably related to the different morphology of the two films due to their different deposition methods. As it was also concluded from the fluorescence properties, vacuum deposited film probably contains smaller fullerene domains, but with smaller distances between them enabling electron tunnelling between the domains.

Fig. 5.21 summarizes the carrier extraction results showing the total electric field drop at long times, and also the electric field drop at 3 ns obtained from TREFISH measurements.

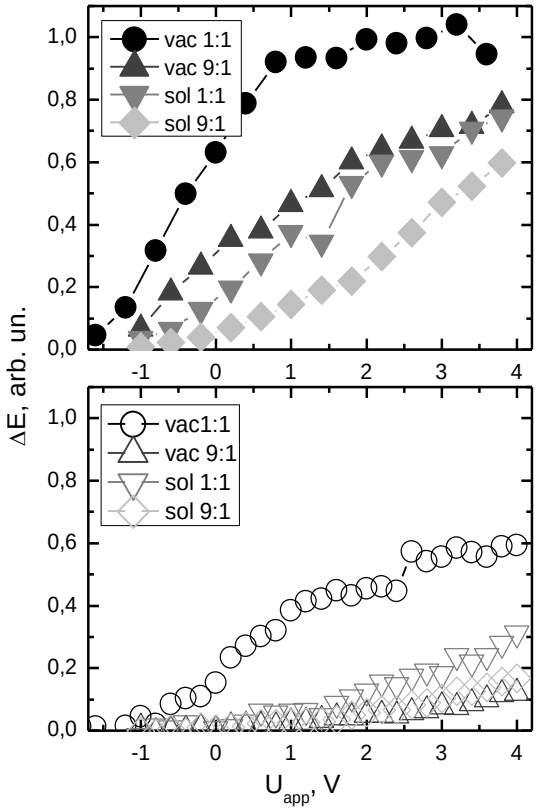

Fig. 5.21. Dependences of the total electric field drop (a) and of the electric field drop at 3 ns in different samples as functions of applied voltage.

The positive voltage drop values obtained at negative voltages are due to the work function difference between Al and ITO electrodes of about 0.8 V creating electric field even without any applied voltage. The total field drop clearly saturates at about 1V of applied voltage in *vac1:1* film. It may be interpreted as an indication that all created charge carriers are extracted from the sample at voltages higher than 1V. The saturation is less expressed for the *sol1:1* and *vac9:1* films, while for the *sol9:1* film we observe voltage drop strongly increasing at high voltages. Total carrier extraction from these samples is evidently not yet achieved at 4V. The voltage drop at 3 ns attributed to the electron extraction also shows tendency of saturation for *vac1:1* film;

majority of electrons are extracted from this sample during 3 ns. In contrast, only small fractions of electrons are extracted during 3 ns from other samples.

It should be noted that the total extracted charge from all the samples increased linearly with excitation intensity up to intensities exceeding those used in the presented investigations several times. It indicates that the excitation intensities in our investigations were below the threshold values of the second order recombination processes, i.e. nongeminate carrier recombination was insignificant. Therefore the variation of the taotal extracted charge values shall be mainly attributed to the limited efficiency of the charge carrier generation and their geminate recombination.

5.3.4 Charge carrier mobility

Fig. 5.19b shows kinetics of the charge carrier displacement distance (l_{dis}) calculated from the voltage kinetics, i.e separation distance along the electric field direction between electron and hole of geminate pair. This distance was obtained by normalizing kinetics of the extracted charge to the total extracted charge and taking into account that average total drift distance of charge carrier equals to the half of the film thickness. It was also assumed that the charge carrier generation is, in the conditions of homogeneous all over the sample thickness.

Separated in time electron and hole extraction phases give us a possibility to calculate the electron mobilities from the voltage kinetics presented in Fig. 5.19b assuming that only electrons contribute to the photocurrent during the initial 3 ns. The carrier mobility calculation procedure was described elsewhere [50]. Briefly the mobility was calculated as: $\mu(t) = \frac{1}{F}\frac{dl_{dis}}{dt}$. The calculation procedure also accounted for the carrier density decrease in time because of their extraction from the sample. The obtained mobility kinetics are presented in Fig. 5.22.

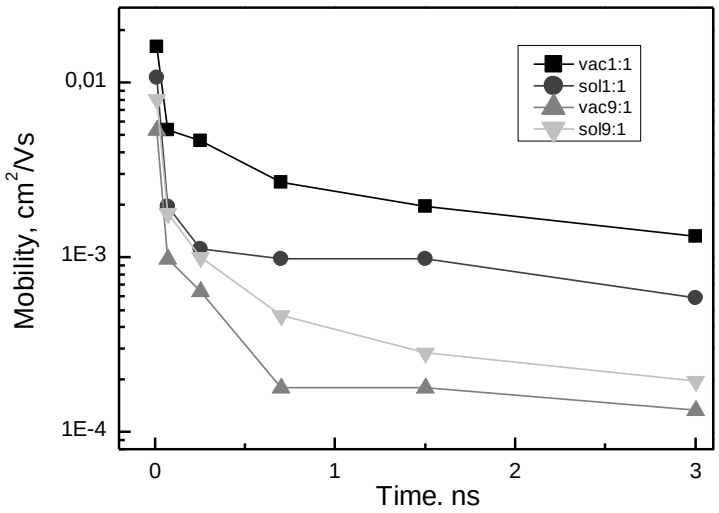

Fig. 5.22. Time dependences of the electron mobilities in different samples obtained from the electric field kinetics by neglecting hole motion and assuming instantaneous carrier generation.

The mobility values are averaged over all the electrons, which were eventually extracted from the sample. The obtained initial mobility on tens of ps time scale in the films with 50% fullerene is several times as low as that obtained in pure PCBM film [148] and drops down about ten-fold during several ns remaining about twice higher for the vac1:1 film than for the sol1:1 film in agreement with the Mackenzie *et* al [149]. predictions. Electron mobilities in films with 10% fullerene are up to 10 times as low. However, it should be noted, that obtained mobility values for these films are less reliable. The, initial mobility values may be reduced if charge carriers are generated not instantaneously. On the other hand, the electron mobility may be overestimated because of neglecting the hole mobility. Nevertheless this evaluation gives us the upper limit of the electron mobility on a ns time scale in these films, which is of about 10^{-4} cm^2/Vs.

Evaluation of the hole mobility dynamics is more problematic because of the carrier trapping and also because of the electron contribution to the photocurrent on a ns - μs time scale. From the kinetics of the displacement distance on the tens of ns time scale (Fig. 5.19b) we obtain the hole mobility value of about 10^{-4} cm^2/Vs, which is almost equal for all the samples. This

value is by at least an order of magnitude higher than the macroscopic hole mobility in MD376 determined in OFET of 10^{-5} cm^2/Vs and in its blend with wt75% of PCBM of $9x10^{-7}$ cm^2/Vs [48]. This is quite natural, because carrier mobilites in polymers and other molecular materials decrease in time by several orders of magnitude [50, 52, 115, 121, 148] before reaching stationary macroscopic mobility values. Indeed, we also observe very slow trapped carrier extraction from some of the samples, which apparently determine the macroscopic mobility.

5.3.5 Charge carrier generation

We will combine fluorescence quenching and carrier transport results to discuss the charge carrier generation mechanism and properties. We will use definition of charge pair (CP) state for charge pairs with larger separation distances but still within mutual Coulomb attraction potential, and the term separated charge carriers (*SCC*) for the electrons and holes which escaped mutual Coulomb attraction. *CT* fluorescence intensity and its quenching by electric field give us information about the formation of *CT* states and their relaxation and splitting into charge pairs. As we have already discussed, we identify two processes reducing the CT exciton concentration: a) fast CT exciton splitting and/or direct generation of CP states by Frenkel exciton dissociation, reducing the initial fluorescence intensity, and b) CT exciton splitting during their entire lifetime.

The highest fluorescence intensity and very low charge extraction from sol9:1 film at zero applied voltage indicates that both carrier generation phases are very inefficient in this film at zero applied voltage. Therefore we will use it as an etalon of the fluorescence intensity when carrier generation is negligible, thus all excitons produce CT states, which all decay without splitting into charge carriers.

In the case of insignificant nongeminate carrier recombination, the total extracted charge gives us the information about the number of created *SCC*.

We estimate the free carrier generation yield by similar procedure as suggested in ref. [123, 124]. Saturation of the total extracted charge from *vac1:1* film observed above 1- 2 V of applied voltage (Fig. 5.21) allows us to conclude that about 1V bias is sufficient to split all the CP states before their geminate recombination. Moreover, very weak CT fluorescence of this film (see Fig. 5.16) indicates that only a small fraction of CT excitons decay to the ground state; majority of them produce CP and eventually SCC states. Thus, we conclude that the internal charge carrier generation and extraction efficiencies are close to 100% in this sample above 1V of applied voltage, which is in agreement with high operation efficiency of solar cells fabricated on the basis of vacuum processed blends with high fullerene content [48]. Therefore we will use the *vac1:1* film as an etalon of 100% CT state dissociation.

Charge carrier generation efficiencies in other samples are much lower at low applied voltages, however as Fig. 5.21 shows, they strongly increase by increasing applied voltage. It indicates that stronger electric fields are necessary in these samples for the *SCC* generation. Table 5.1 summarizes fluorescence and charge carrier extraction results.

Table 5.1. Normalised values of the initial fluorescence intensity F_0 , time-integrated fluorescence $\int F$, and total extracted charge Q.

		0V			2V		
	F_0	$\int F$	Q,	$\int F+Q$	$\int F$	Q	$\int F+Q$
sol9:1	1	0.95	0.05	*1*	0.82	0.25	*1.07*
sol1:1	0.55	0.57	0.15	*0.72*	0.35	0.50	*0.85*
vac9:1	1.01	0.78	0.30	*1.09*	0.51	0.62	*1.13*
vac1:1	0.14	0.12	0.65	*0.77*	0.05	1	1.05

Here the fluorescence data are normalized to the fluorescence intensity of sol9:1 film at zero applied voltage used as an etalon of fluorescence intensity when carrier generation is neglidgible, and the extracted charge values are normalized to the extracted charge from vac1:1 film at 2V applied

voltage used as etalon of 100% carrier generation. Therefore, normalized initial CT fluorescence intensity F_0 corresponds to the initial CT exciton yield and the integrated fluorescence intensity $\int F$ corresponds to the fraction of created excited states relaxing to the ground state via emissive CT states. The total extracted charge Q corresponds to the charge carrier yield. According to this definition 1-F_0 value corresponds to the fraction of ultrafast created CP states and the difference between F_0 and $\int F$ values corresponds to the fraction of CP states generated during the entire CT exciton lifetime.

$\int F+Q$ should be equal to one if all the created excitations relax to the ground state via emissive CT states or produce charge carriers. Taking measurement errors into account, this condition is fulfilled for the samples with 10% fullerene, while significantly lower $\int F+Q$ values obtained for the samples with 50% fullerene, at least at zero applied voltage. It indicates that some additional nonemissive relaxation channel appears at high fullerene concentration. Significant difference between F_0 and $\int F$ values shows that a large fraction of charge pairs in these samples are generated by the ultrafast mechanism, therefore it is reasonable to relate the nonemissive relaxation channel to the ultrafast CP generation. Since ultrafast CP state generation requires no electric field assistance, it is reasonable to assume that created electron-hole pair orientations are random with respect to the electric field direction. Therefore, at later times the electric field drags a fraction of charge carriers back to their initial positions forcing geminate recreation of CT excitons. In contrast, in case of slow field-induced carrier separation, dominating in samples with 10% fullerene content, charge carriers are separated only along electric field and their motion back and recreation of CT excitons is very improbable. Therefore, geminate CP state recombination and recreation of CT excitons is substantial only in samples with 50% fullerene content. It is reasonable to relate the nonemissive relaxation channel with the CT exciton recreation. Due to weak electron–hole coupling in CP state, rapid electron spin mixing may take place [82, 150]. According to the spin statistics 75% of recombining CP states creates triplet CT states and only 25% recreate

singlet excitons. Therefore, majority of geminately recombining CP states recreate triplet CT excitons, which relax nonradiatively.

Charge carrier drift dynamics (Fig. 5.19) supports the presented charge carrier generation mechanism. Charge carriers in *sol9:1* and *vac9:1* films are generated relatively slowly during the initial several ns, therefore only few generated *CP* states with mobile charge carriers are present at short times. Therefore the drift distance normalized to the total number of extracted charge carriers is initially very small. On the other hand, majority of the charge pairs in these samples are generated during the initial 1-2 ns, therefore, generation kinetics could hardly influence the drift dynamics on a time scale of tens of nanoseconds. Consequently our previous conclusion on relatively slow electron and hole motions remains valid.

The two mechanisms of CP state generation partly explain different dependences of the total extracted photocurrent on the applied voltage. Majority of excitons create CP states in *vac1:1* film without electric field assistance and even weak electric field is sufficient to separate them into free carriers, which are eventually extracted from the samples. In contrast, strong electric field is necessary for the charge carrier generation and extraction from *sol9:1* film where dissociation of CT excitons requires assistance of strong electric field. The *sol1:1 vac9:1* films represent intermediate cases.

Fig. 5.23 summarizes the discussion above, presenting charge carrier generation scheme, and Table 5.2 presents efficiencies of the discussed processes determined from the fluorescence and charge extraction data.

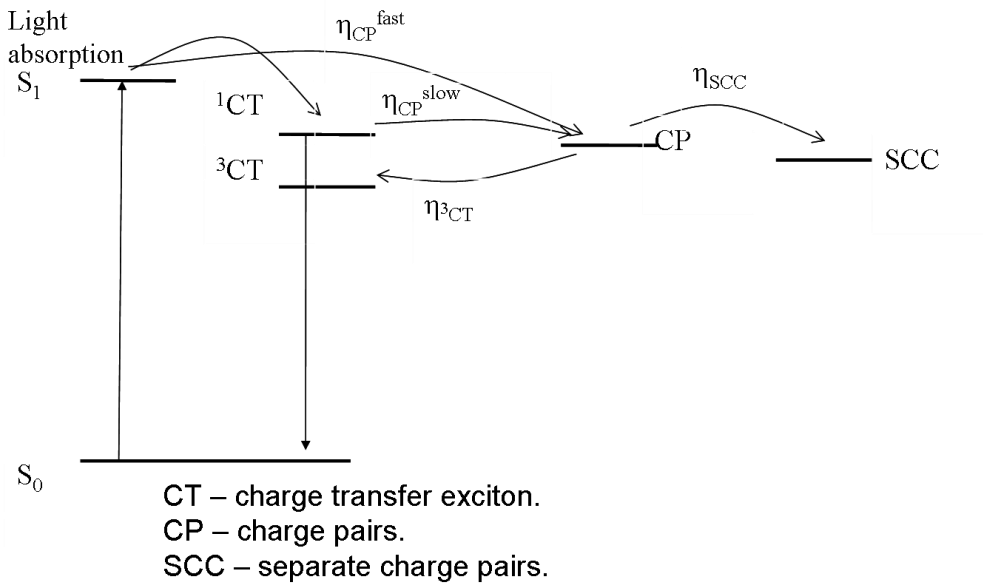

Fig. 5.23. Schematic representation of relaxational processes in blends under applied field, which, together with entropy, reduces CP and SCC state energies. Arrow labels denote efficiencies of various processes. Electron back transfer from CP to ^{1}CT state is not shown, assuming that it just reduces the η_{CP}^{slow}.

Table 5.2. Efficiencies of various relaxational processes shown in scheme 1 at 0V and 2V of applied voltages evaluated from initial and integrated fluorescence intensities and from extracted charge values.

	0V				2V			
	η_{CP}^{fast}	η_{CP}^{slow}	η_{SCC}	$\eta 3_{CT}$	η_{CP}^{fast}	η_{CP}^{slow}	η_{SCC}	$\eta 3_{CT}$
sol9:1	0	0.05	0.05	*0*	0	0.18	*0.25*	*-0.07*
sol1:1	0.45	-0.02	0.15	*0.30*	0.45	0.20	*0.50*	*0.15*
vac9:1	0	0.22	0.30	*-0.08*	0	0.51	*0.62*	*-0.13*
vac1:1	0.86	0.02	0.65	*0.23*	0.86	0.09	1	-0.05

Because of the simplified model and measurement errors the presented scheme should be only interpreted as qualitative, the exact efficiencies of various processes may differ from the estimated values significantly; however, it reveals the main processes and their dependences on the device structure. Briefly, charge pair generation in films with 50% fullerene takes place

dominantly by the ultrafast, field independent generation mechanism and a fraction of generated CP states recombine creating triplet CT excitons. CP state generation in films with 10% fullerene takes place by the field-induced CT exciton splitting during their entire lifetime with insignificant geminate recombination. Now we will shortly discuss the mechanisms of different carrier generation processes and how they are related to the material structure.

Ultrafast charge pair generation. As was discussed, this process occurs much faster than within 50 ps and is independent or only weakly depends on the electric field strength. The mechanism of the ultrafast carrier generation, has been widely discussed during recent years and is considered as basic process determining operation of organic solar cells. Several concepts have been suggested to explain fast and efficient carrier separation against mutual Coulomb attraction. Dissociation of hot interfacial CT excitons was suggested to produce charge pairs during several hundreds of femtoseconds [93, 109, 114, 117, 151–153] . Our results show that the ultrafast CP state generation is efficient only in the case of high fullerene concentration. Most probably, this is related to the fullerene domain size as was also suggested for fluorine copolymer:PCBM blend [106]. Electrons, which possess high mobility should be able to diffuse and to be localized within sufficiently large distances before they relax to the bottom of the density of states. According to the estimation made in ref. [154], common action of Coulomb attraction and entropy forms energy barrier at about 5 nm distance. Thus the ultrafast initial separation should be comparable to this distance to prevent rapid recombination. Therefore, sufficiently large fullerene domains are essential for the ultrafast charge carrier separation. Fullerene molecules most probably do not form sufficiently large domains in films with only 10% concentration and the hole mobility inside merocyanine, which, according to our evaluation, is much lower than that of electrons and is not sufficient to enable carrier separation. We have recently demonstrated that entropy driven [155] fast initial carrier diffusion drags charge carriers apart by several nm during the initial several ps in P3HT/PCBM blends [154], while carrier drift at electric fields of the order

of 10^5 V/cm plays only minor role during this time. According to this model, the efficiency of this process is expected to be very high in *vac1:1* film because of high electron mobility. Based on the Einstein relation $Dq = \mu k_B T$, we obtain the initial diffusion coefficient of electrons in *vac1:1* film of about 4×10^6 cm^2/s. It gives about 5 nm average diffusion length of electrons during initial 100 ps, sufficient to reach energy barrier.

Different efficiencies of the ultrafast separation phase in vacuum and in solution processed films with 50% fulerene concentration is less clear. It may be due to different material segregation, or due to different properties of fullerene and PCBM clusters. Several times lower electron mobility in PCBM than in fullerene (see Fig. 5.22) is the most straightforward explanation. On the other hand, merocyanine morphology, which is probably also different in vacuum and solution processed films hardly plays important role, because, as was discussed, hole motion is less important for the fast carrier separation.

Relatively small CT exciton binding energy of about 0.2 eV is another important factor determining efficiency of the ultrafast CT exciton dissociation. Before relaxation to low energy states inside DOS, charge carriers have sufficient energy to overcome Coulomb attraction, what they can do even without initial carrier delocalization or initial creation of the long distance charge transfer states. Thus, our data show that the ultrafast carrier generation phase, which is particularly efficient in *vac1:1* film, may be described by the Onsager-Broun model with initial separation distance determined by the fast diffusion of nonthermalised electrons inside fullerene domains. According to this model, ensemble of charge pair states with different electron-hole separation distances, including the nearest neighbour emissive CT excitons, is created during several ps. The created ensemble is dynamic; electron-hole distances constantly change driven by thermal energy. As time progresses charge carriers separate to larger distances or gradually geminately recombine via CT excitons. Therefore the CT exciton kinetics depends on its relaxation rate as well as separation of charge pairs to longer distances and their geminate recombination.

Charge pair generation during the entire CT exciton lifetime. This carrier separation phase driven by thermal energy and by electric field is related to the dissociation of relaxed *CT* excitons. It causes slow appearance of free charge carriers, which we observe as slowly increasing carrier displacement distance on a 3 ns time scale. Although, this process is less efficient in films with 10% fullerene concentration, it is responsible for the photoconductivity of these films since the ultrafast separation phase in these films is absent. CT exciton dissociation even at zero applied voltage indicates that its binding energy is relatively low, so that the energy barrier may be overcome when it is reduced by electric field. Assuming dielectric susceptibility of blends $\varepsilon = 3$ and using point charge approximation we obtain that electric field of about 2.5×10^5 V/cm reduces the energy barrier along electric field direction by about 0.2 eV and shifts it closer to the countercharge. Efficient fluorescence quenching shows that the reduced energy barrier becomes comparable to the thermal energy. Thus, the estimated CT exciton binding of about 0.2-0.3 eV is comparable with the CT exciton binding energies estimated for polymer:PCBM blends of about 0.2 eV [146].

Moreover, shorter fluorescence lifetime of CT excitons and larger photocurrent at zero applied voltage in *vac9:1* film in comparison to *sol9:1* film imply that that the CT exciton splitting in *vac9:1* film takes place at build-in electric field of about 1.6×10^5 V/cm or probably even at zero field. Very short fluorescence lifetime in *vac1:1* film unambiguously shows that such CT exciton dissociation does take place and is very efficient in *vac1:1* film. Hole diffusion inside merocyanine is apparently responsible for the relaxed CT exciton dissociation in the films with 10% fullerene, since electrons confined in small fullerene clusters cannot escape from Coulomb attraction. However, electron motion inside fullerene clusters may be also important, as it increases the *e-h* distance and makes it easier for the holes to escape from Colulomb attraction. It explains more efficient relaxed CT exciton dissociation in *vac9:1* films in comparison with the *sol9:1* films, where electron mobility is lower. Relaxed CT exciton dissociation is much more efficient in films with 50%

fullerene, where both, electrons and holes, are mobile, and evidently, high electron mobility makes this process very efficient in *vac1:1* film.

5.4 Concluding remarks

Formation of low energy intermolecular charge transfer states CT_{M-M} was found in neat MD376 films and charge transfer CT_{M-F} states between MD376 and PCBM molecules in blends.

Charge transfer state CT_{M-F} dominates over CT_{M-M} in MD376 blends with PCBM because of higher their density and probably lower energy.

The investigations revealed two types of photogenerated charged species: emissive relaxed *CT* states and charge pairs with larger *e-h* separation distances. The charge pairs are generated by two processes: a) ultrafast field independent generation and b) dissociation of CT relaxed during their entire lifetime.

Electron mobility within fullerene domains was found to be much higher than the hole mobility in merocyanines in films containing 50% fullerene. Fast diffusion of nonrelaxed electrons inside fullerene domains determines fast charge pair generation phase and therefore this process is efficient only in blends with high fullerene concentration where the domains are sufficiently large. Higher electron mobility in fullerene domains than in PCBM domains is most likely responsible for more efficient charge pair generation in vacuum deposited blends

General conclusions

1. Fluorescence lifetimes of PDHS polymer nanocomposites meanly depend on temperature and inorganic matrix. PDHS incorporation into organic matrixes improves fluorescence properties and can be useful for light emitting devices production.

2. Internal charge transfer states are formed in PSF-BT films therefore exciton-exciton annihilation in F8BT and PSF-BT polymers are different. Free charge carriers are generated after exciton-exciton annihilation in F8BT, while internal charge transfer states are formed in PSF-BT.

3. The investigations revealed unexpected influence of PCBM additives on charge carrier generation and motion in PSF-BT films. PCBM increases efficiency of the charge carrier photogeneration, but, on the other hand, slows down the charge carrier extraction time.

4. Two types of charge transfer excitons were discovered in merocyanine MD376 neat films and in its blends with fullerene derivatives. Intermolecular charge transfer states were found in neat films, while charge transfer states between MD376 and PCBM dominate in blends.

5. Two types of photogenerated charged species are formed in MD376/fullerene blends: emissive relaxed *CT* states and charge pairs with larger *e-h* separation distances. The charge pairs are generated by two processes: a) ultrafast field independent generation because of nonrelaxed exciton disociation and b) dissociation of relaxed CT states during their entire lifetime. Ultrafast field independent generation was observed in MD376 with high fullerene concentration (50%). Dissociation of relaxed CT states during their entire lifetime dominates in blends with low fullerene concentration (10%), this kind of charge pairs generation

mechanism was observed in in MD376 with high fullerene derivatives concentration, bus had lower influence.

6. Charge pair generation is more efficient in vacuum deposited blends most likely because of higher electron mobility in fullerene domains than in PCBM domains.

References

1. Shinar, J., Shinar, R.: Organic light-emitting devices (OLEDs) and OLED-based chemical and biological sensors: an overview. J. Phys. D. Appl. Phys. 41, 133001 (2008).

2. Li, G., Zhu, R., Yang, Y.: Polymer solar cells. Nat. Photonics. 6, 153–161 (2012).

3. http://www.nobelprize.org/nobel_prizes/chemistry/laureates/2000/.

4. Feron, K., Belcher, W.J., Fell, C.J., Dastoor, P.C.: Organic solar cells: understanding the role of Förster resonance energy transfer. Int. J. Mol. Sci. 13, 17019–47 (2012).

5. Klauk, H.: Organic thin-film transistors. Chem. Soc. Rev. 39, 2643–66 (2010).

6. Cicoira, F., Santato, C.: Organic Light Emitting Field Effect Transistors: Advances and Perspectives. Adv. Funct. Mater. 17, 3421–3434 (2007).

7. Samuel, I.D.W., Turnbull, G. a: Organic semiconductor lasers. Chem. Rev. 107, 1272–95 (2007).

8. Chidichimo, G., Filippelli, L.: Organic Solar Cells: Problems and Perspectives. Int. J. Photoenergy. 2010, 1–11 (2010).

9. Kronenberg, N.M., Steinmann, V., Bürckstümmer, H., Hwang, J., Hertel, D., Würthner, F., Meerholz, K.: Direct comparison of highly efficient solution- and vacuum-processed organic solar cells based on merocyanine dyes. Adv. Mater. 22, 4193–7 (2010).

10. http://www.epitaxy.net/, http://www.epitaxy.net/.

11. http://www.oled-info.com/oled_devices/mobile_phones.

12. Muccini, M.: A bright future for organic field-effect transistors. Nat Mater. 5, 605–613 (2006).

13. Zaumseil, J., Sirringhaus, H.: Electron and Ambipolar Transport in Organic Field-Effect Transistors. Chem. Rev. 107, 1296–1323 (2007).

14. Chénais, S., Forget, S.: Recent advances in solid-state organic lasers. Polym. Int. 61, 390–406 (2012).

15. Mishra, A., Bäuerle, P.: Small molecule organic semiconductors on the move: promises for future solar energy technology. Angew. Chem. Int. Ed. Engl. 51, 2020–67 (2012).

16. Fave, C., Hissler, M., Kárpáti, T., Rault-Berthelot, J., Deborde, V., Toupet, L., Nyulászi, L., Réau, R.: Connecting π-Chromophores by σ-P−P Bonds: New Type of Assemblies Exhibiting σ−π-Conjugation. J. Am. Chem. Soc. 126, 6058–6063 (2004).

17. Ostapenko, N., Kozlova, N., Suto, S., Watanabe, A.: Spectroscopy of nanosized composites consisting of silicon-organic polymers in nanoporous silicas. Low Temp. Phys. 32, 1035 (2006).

18. Ostapenko, N., Telbiz, G., Ilyin, V., Suto, S., Watanabe, A.: Criticality of fluorescence spectra of the nanosized polysilanes oriented in the mesoporous silica. Chem. Phys. Lett. 383, 456–461 (2004).

19. Ostapenko, N., Kotova, N., Lukashenko, V., Telbiz, G., Gerda, V., Suto, S., Watanabe, A.: Size effect in optical spectra of nanostructured polysilanes. J. Lumin. 112, 381–385 (2005).

20. Burroughes, I.H., Bradley, D.C., Brown A.R.: Light-emitting diodes based on conjugated polymer. Nature. 347, 539–541 (1990).

21. Tessler, N.: Lasers Based on Semiconducting Organic Materials. Adv. Mater. 11, 363–370 (1999).

22. Stephen, R. F.: Organic Photonics : Toward A New Generation of Thin Film Photovoltaics and Lasers. OMB, 0704, 1–24 (2011).

23. Riechel, S.: Organic semiconductor lasers with two-dimensional distributed feedback. (2002).

24. Vasdekis, E., Moore, S., Ruseckas, A., Krauss, T.F., Samuel, I.D.W., Turnbull, G. A.: Silicon based organic semiconductor laser. Appl. Phys. Lett. 91, 051124 (2007).

25. Tsiminis, G., Ruseckas, A., Samuel, I.D.W., Turnbull, G. : A two-photon pumped polyfluorene laser. Appl. Phys. Lett. 94, 253304 (2009).

26. Amarasinghe, D., Ruseckas, A., Vasdekis, A. E., Turnbull, G. A., Samuel, I.D.W.: Picosecond gain switching of an organic semiconductor optical amplifier. Appl. Phys. Lett. 92, 083305 (2008).

27. Mishra, A., Bäuerle, P.: Small molecule organic semiconductors on the move: promises for future solar energy technology. Angew. Chem. Int. Ed. Engl. 51, 2020–67 (2012).

28. Becquerel A. E., H.C.R.: Mémoire sur les effets électriques produits sous l'influence des rayons solaires. Seances Acad. Sci. 9, 591–567 (1839).

29. Miles, R.W., Hynes, K.M., Forbes, I.: Photovoltaic solar cells: An overview of state-of-the-art cell development and environmental issues. Prog. Cryst. Growth Charact. Mater. 51, 1–42 (2005).

30. Green, M.A., Emery, K., Hishikawa, Y., Warta, W., Dunlop, E.D.: Solar cell efficiency tables (version 39). Prog. Photovoltaics Res. Appl. 20, 12–20 (2012).

31. Aberle, A.G.: Surface passivation of crystalline silicon solar cells: a review. Prog. Photovoltaics Res. Appl. 8, 473–487 (2000).

32. Rohr S.: Heliatek consolidates its technology leadership by establishing a new world record for organic solar technology with a cell efficiency of 12%. 1–3 (2013).

33. http://www.heliatek.com.

34. Deibel, C., Dyakonov, V.: Polymer – Fullerene Bulk Heterojunction Solar Cells. Rep. Prog. Phys. 73, 096401 1–68 (2010).

35. Tang, C.W.: Multilayer organic photovoltaic elements, (1979).

36. Chen, H., Hou, J., Zhang, S., Liang, Y., Yang, G., Yang, Y.: Polymer solar cells with enhanced open-circuit voltage and efficiency. 3, 649–653 (2009).

37. Yu, G., Gao, J., Hummelen, J.C., Wudl, F., Heeger, A. J.: Polymer Photovoltaic Cells: Enhanced Efficiencies via a Network of Internal Donor-Acceptor Heterojunctions. Science (80-.). 270, 1789–1791 (1995).

38. Janssen, R. a J., Nelson, J.: Factors limiting device efficiency in organic photovoltaics. Adv. Mater. 25, 1847–58 (2013).

39. Pal, S.K., Kesti, T., Maiti, M., Zhang, F., Inganäs, O., Hellström, S., Andersson, M.R., Oswald, F., Langa, F., Osterman, T., Pascher, T., Yartsev, A., Sundström, V.: Geminate charge recombination in polymer/fullerene bulk heterojunction films and implications for solar cell function. J. Am. Chem. Soc. 132, 12440–51 (2010).

40. Watanabe, A., Miyashita, T., Kasuya, A., Takahashi, M., Kawazoe, Y.: Fluorescence spectra of poly(di-n-hexylsilane)/TiO2 nanoparticle hybrid film. Polymer 49, 554–560 (2008).

41. Kazlauskas, K., Dementjev, A., Gulbinas, V., Valkūnas, L., Vitta, P., Žukauskas, A., Ostapenko, N., Suto, S.: Temperature independent exciton relaxation in poly(di-n-hexylsilane) confined in nanoporous silica. Chem. Phys. Lett. 465, 261–264 (2008).

42. Dementjev, A., Gulbinas, V., Valkunas, L., Ostapenko, N., Suto, S., Watanabe, A.: Coexistence of Different Conformer Forms in Nanosize Poly(di-n-hexylsilane). J. Phys. Chem. C. 111, 4717–4721 (2007).

43. Hodgkinson W. R.: Note on some derivatives of fluorene, C13H10. J. Chem. Soc., Trans. 43, 163–172 (1883).

44. Leclerc, M.: Polyfluorenes: Twenty years of progress. J. Polym. Sci. Part A Polym. Chem. 39, 2867–2873 (2001).

45. Williams C.G.: Trans. R. Soc. Edinburgh. 21, 377–401 (1856).

46. Würthner, F., Kaiser, T.E., Saha-Möller, C.R.: J-aggregates: from serendipitous discovery to supramolecular engineering of functional dye materials. Angew. Chem. Int. Ed. Engl. 50, 3376–410 (2011).

47. Steinmann, V., Kronenberg, N.M., Lenze, M.R., Graf, S.M., Hertel, D., Meerholz, K., Bürckstümmer, H., Tulyakova, E. V, Würthner, F.: Simple, Highly Efficient Vacuum-Processed Bulk Heterojunction Solar Cells Based on Merocyanine Dyes. Adv. Energy Mater. 1, 888–893 (2011).

48. Bürckstümmer, H., Kronenberg, N.M., Gsänger, M., Stolte, M., Meerholz, K., Würthner, F.: Tailored merocyanine dyes for solution-processed BHJ solar cells. J. Mater. Chem. 20, 240 (2010).

49. http://www.solarischem.com/Fullerenes.html.

50. Devižis, A., Serbenta, A., Meerholz, K., Hertel, D., Gulbinas, V.: Ultrafast Dynamics of Carrier Mobility in a Conjugated Polymer Probed at Molecular and Microscopic Length Scales. Phys. Rev. Lett. 103, 027404 (2009).

51. Devizis, A., Meerholz, K., Hertel, D., Gulbinas, V.: Ultrafast charge carrier mobility dynamics in poly(spirobifluorene-co-benzothiadiazole): Influence of temperature on initial transport. Phys. Rev. B. 82, 155204 (2010).

52. Devižis, A., Meerholz, K., Hertel, D., Gulbinas, V.: Hierarchical charge carrier motion in conjugated polymers. Chem. Phys. Lett. 498, 302–306 (2010).

53. D.Y. Kim, H.N. Cho, C.Y. Kim, D.Y. Kim, H.N. Cho, C.Y. Kim: Blue light emitting polymers. Proq. Polym. Sci. 25, 1089 – 1139 (2000).

54. M. Shimize, T. Hijama: Organic fluorophores exhibiting highly efficient photoluminescence in the solid state. Chem. Asian J. 5, 1516 – 1531 (2010).

55. Wang M. , Zhaug G.X. , Zhaug D.Q. , Zhu D.B., T.B.Z.T.: Fluorescent bio/chemosensors based on silole and tetraphenylethene luminogens with aggregation-induced emission feature. J. Mater. Chem. 20, 1858 – 1867 (2010).

56. Tomas S.W. , Joly G.D., S.T.M.: Chemical sensors based on amplifying fluorescent conjugate polymers. Chem. Rew. 107, 1336 – 1386 (2007).

57. Adhikari B.: Polymers in sensors application. Prog. Polym. Sci. 29, 699 – 766 (2004).

58. Lin J., Lam J.W.V., T.B.Z.: Aggregation-induced emission of silole molecules and polymers: fundamental and applications. J. Jnorg. Organomet. Polym. 19, 249 – 285 (2009).

59. Ren, Y., Lam, J.W.Y., Dong, Y., Tang, B.Z., Wong, K.S.: Enhanced Emission Efficiency and Excited State Lifetime Due to Restricted Intramolecular Motion in Silole Aggregates. J. Phys. Chem. B 109, 1135–1140 (2005).

60. Gao, B.-R., Wang, H.-Y., Hao, Y.-W., Fu, L.-M., Fang, H.-H., Jiang, Y., Wang, L., Chen, Q.-D., Xia, H., Pan, L.-Y., Ma, Y.-G., Sun, H.-B.: Time-Resolved Fluorescence Study of Aggregation-Induced Emission Enhancement by Restriction of Intramolecular Charge Transfer State. J. Phys. Chem. B. 114, 128–134 (2010).

61. Hong, Y., Lam, J.W.Y., Tang, B.Z.: Aggregation-induced emission: phenomenon, mechanism and applications. Chem. Commun. 29, 4332–4353 (2009).

62. Chen, J., Law, C.C.W., Lam, J.W.Y., Dong, Y., Lo, S.M.F., Williams, I.D., Zhu, D., Tang, B.Z.: Synthesis, Light Emission, Nanoaggregation, and Restricted Intramolecular Rotation of 1,1-Substituted 2,3,4,5-Tetraphenylsiloles. Chem. Mater. 15, 1535–1546 (2003).

63. Chen, J., Xie, Z., Lam, J.W.Y., Law, C.C.W., Tang, B.Z.: Silole-Containing Polyacetylenes. Synthesis, Thermal Stability, Light Emission, Nanodimensional Aggregation, and Restricted Intramolecular Rotation. Macromolecules. 36, 1108–1117 (2003).

64. Yuan, W.Z., Zhao, H., Shen, X.Y., Mahtab, F., Lam, J.W.Y., Sun, J.Z., Tang, B.Z.: Luminogenic Polyacetylenes and Conjugated Polyelectrolytes: Synthesis, Hybridization with Carbon Nanotubes, Aggregation-Induced Emission, Superamplification in Emission Quenching by Explosives, and Fluorescent Assay for Protein Quantitation. Macromolecules. 42, 9400–9411 (2009).

65. Krylova G.V. , Gnatyuk Yu.I. , Smirnova N.P. , Eremenko A.M., G.V.M.: Ag nanoparticles deposited onto silica, titania, and zirconia mesoporous films synthesized by sol–gel template method. J. Sol-Gel Sci. Technol. 50, 216 – 228 (2009).

66. Ostapenko N.I , Kozlova N.V., F.E.K.: Spectral properties of silicon-organic polymer SiO2 porous film nanocomposites films. J. Appl. Spectr. 98, 75 – 80 (2011).

67. Gunko A. M. , Turov V. V., Turov A. V. , Zarko V. I. , Gerda V. I.: Cent. Eur. J. Chem. 5, 420–451 (2007).

68. Kuznetsov A.I., Kameneva O., Bityurin N., Rozes L., Sanchez C.: Laser-induced photopatterning of organic-inorganic TiO2-based hybrid materials with tunable interfacial electron transfer. Phys Chem Chem Phys. 11, 1248–1257 (2009).

69. Miller, R. D., and Michl, J.: Polysilane High Polymers. J. Chem. Rev. 89, 1359–1410 (1989).

70. Bukalov, S.S., Leites, L.A., West, R.: Thermochromism of Poly(di-n-hexylsilane) in Solution Revisited. Macromolecules. 34, 6003–6004 (2001).

71. Shimizu, M., Suto, S., Goto, T., Watanabe, A., Matsuda, M.: Temperature dependence of exciton dynamics in poly(di-n-hexylsilane). Phys. Rev. B. 63, 073403 (2001).

72. Staruch G., Smirnova N.: Laser-induced electron transfer processes in complex pyrene-b-cyclodextrin in titanosilicate systems. Theor. Experim. Chem. 37, 100 – 104 (2001).

73. Kathiravan A., Anbazhagan V., Asha Jhonsi M.: A Study on the fluorescence Quenching of Eosin by certain Organic Dyes. Zeitschrift für Phys. Chemie. 222, 1013–1021 (2008).

74. Clark, J., Lanzani, G.: Organic photonics for communications. Nat. Phot. 4, 438–446 (2010).

75. Barth, S., Bässler, H., Scherf, U., Müllen, K.: Photoconduction in thin films of a ladder-type poly-para-phenylene. Chem. Phys. Lett. 288, 147–154 (1998).

76. Nishihara, Y., Matsuda, A., Fujii, A., Ozaki, M., Frankevich, E.L., Yoshino, K.: Origin of Free Charge Carrier Generation of the Second-order Process Photocurrent in Conjugated Polymer Studied by Two-Correlated-Pulse Technique. Synth. Met. 154, 101–104 (2005).

77. Gadermaier, C., Cerullo, G., Manzoni, C., Scherf, U., List, E.J.W., Lanzani, G.: Double-excitation dynamics in m-LPPP probed with sub-20 fs time resolution. Synth. Met. 139, 605–607 (2003).

78. Zenz, C., Lanzani, G., Cerullo, G., Graupner, W., Leising, G., Scherf, U., DeSilvestri, S.: Femtosecond photo-current excitation cross-correlation on a ladder type polymer. Synth. Met. 116, 27–30 (2001).

79. Müller, J.G., Scherf, U., Lemmer, U.: Two step charge carrier generation in a ladder-type conjugated polymer. Synth. Met. 119, 395–396 (2001).

80. Hiramoto M., Fujiwara H., Yokoyama, M.: p−i−n Like Behavior 671 in Three − Layered Organic Solar Cells Having a Co − Deposited 672 Interlayer of Pigments. J. Appl. Phys. 72, 3781−3787 (1992).

81. Halls, J.J.M., Walsh, C.A., Greenham, N.C., Marseglia, E.A., Friend, R.H., Moratti, S.C., Holmes, A.B.: Efficient photodiodes from interpenetrating polymer networks. Nature. 376, 498–500 (1995).

82. Clarke, T.M., Durrant, J.R.: Charge photogeneration in organic solar cells. Chem. Rev. 110, 6736–6767 (2010).

83. Günes, S., Neugebauer, H., Sariciftci, N.S.: Conjugated Polymer-Based Organic Solar Cells. Chem. Rev. 107, 1324–1338 (2007).

84. Barth, S., Bässler, H.: Intrinsic Photoconduction in PPV-Type Conjugated Polymers. Phys. Rev. Lett. 79, 4445–4448 (1997).

85. Barth S., Bässler H., Rost H.: Extrinsic and Intrinsic DC Photoconductivity in a Conjugated Polymer. Phys. Rev. B. 56, 3844–3851 (1997).

86. Peet, J., Kim, J.Y., Coates, N.E., Ma, W.L., Moses, D., Heeger, A.J., Bazan, G.C.: Efficiency enhancement in low-bandgap polymer solar cells by processing with alkane dithiols. Nat Mater. 6, 497–500 (2007).

87. He, Z., Zhong, C., Huang, X., Wong, W.-Y., Wu, H., Chen, L., Su, S., Cao, Y.: Simultaneous Enhancement of Open-Circuit Voltage, Short-

Circuit Current Density, and Fill Factor in Polymer Solar Cells. Adv. Mater. 23, 4636–4643 (2011).

88. Sun, Y., Welch, G.C., Leong, W.L., Takacs, C.J., Bazan, G.C., Heeger, A.J.: Solution-processed small-molecule solar cells with 6.7% efficiency. Nat Mater. 11, 44–48 (2012).

89. http://www.polyera.com/press-releases/.

90. Dou, L., You, J., Yang, J., Chen, C.-C., He, Y., Murase, S., Moriarty, T., Emery, K., Li, G., Yang, Y.: Tandem polymer solar cells featuring a spectrally matched low-bandgap polymer. Nat Phot. 6, 180–185 (2012).

91. Havinga E. E., Ten H. W.: A New Class of Small Band Gap Organic Polymer Conductors. Polym. Bull. 29, 119–126 (1992).

92. Würthner, F., Meerholz, K.: Systems Chemistry Approach in Organic Photovoltaics. Chem. Eur. J. 16, 9366–9373 (2010).

93. Bakulin, A. A, Rao, A., Pavelyev, V.G., van Loosdrecht, P.H.M., Pshenichnikov, M.S., Niedzialek, D., Cornil, J., Beljonne, D., Friend, R.H.: The role of driving energy and delocalized States for charge separation in organic semiconductors. Science. 335, 1340–1344 (2012).

94. Albrecht, S., Schindler, W., Kurpiers, J., Kniepert, J., Blakesley, J.C., Dumsch, I., Allard, S., Fostiropoulos, K., Scherf, U., Neher, D.: On the Field Dependence of Free Charge Carrier Generation and Recombination in Blends of PCPDTBT/PC70BM: Influence of Solvent Additives. J. Phys. Chem. Lett. 3, 640–645 (2012).

95. Paquin, F., Latini, G., Sakowicz, M., Karsenti, P.-L., Wang, L., Beljonne, D., Stingelin, N., Silva, C.: Charge Separation in Semicrystalline Polymeric Semiconductors by Photoexcitation: Is the Mechanism Intrinsic or Extrinsic? Phys. Rev. Lett. 106, 197401 (2011).

96. Muller, C.D., Falcou, A., Reckefuss, N., Rojahn, M., Wiederhirn, V., Rudati, P., Frohne, H., Nuyken, O., Becker, H., Meerholz, K.: Multi-colour organic light-emitting displays by solution processing. Nature. 421, 829–833 (2003).

97. Stevens, M., Silva, C., Russell, D., Friend, R.: Exciton dissociation mechanisms in the polymeric semiconductors poly(9,9-dioctylfluorene) and poly(9,9-dioctylfluorene-co-benzothiadiazole). Phys. Rev. B. 63, 165213 (2001).

98. Gulbinas, V., Mineviciūte, I., Hertel, D., Wellander, R., Yartsev, A., Sundström, V.: Exciton diffusion and relaxation in methyl-substituted polyparaphenylene polymer films. J. Chem. Phys. 127, 144907 (2007).

99. Gaab, K.M., Bardeen, C.J.: Anomalous Exciton Diffusion in the Conjugated Polymer MEH−PPV Measured Using a Three-Pulse Pump−Dump−Probe Anisotropy Experiment. J. Phys. Chem. A. 108, 10801–10806 (2004).

100. Grage, M.M.-L., Wood, P.W., Ruseckas, A., Pullerits, T., Mitchell, W., Burn, P.L., Samuel, I.D.W., Sundström, V.: Conformational disorder and energy migration in MEH-PPV with partially broken conjugation. J. Chem. Phys. 118, 7644 (2003).

101. Devizis, A., Serbenta, A., Peckus, D., Thiessen, A., Alle, R., Meerholz, K., Hertel, D., Gulbinas, V.: Electric field assisted charge carrier photogeneration in poly(spirobifluorene-co-benzothiadiazole). J. Chem. Phys. 133, 164904 (2010).

102. Devižis, A., Serbenta, A., Meerholz, K., Hertel, D., Gulbinas, V.: Excited state relaxation in poly(spirobifluorene-co-benzothiadiazole) films. J. Chem. Phys. 131, 104902 (2009).

103. King, S.M., Hintschich, S.I., Dai, D., Rothe, C., Monkman, A.P.: Spiroconjugation-Enhanced Intramolecular Charge-Transfer State Formation in a Polyspirobifluorene Homopolymer. J. Phys. Chem. C. 111, 18759–18764 (2007).

104. Hintschich, S.I., Rothe, C., King, S.M., Clark, S.J., Monkman, A.P.: The Complex Excited-state Behavior of a Polyspirobifluorene Derivative: The Role of Spiroconjugation and Mixed Charge Transfer Character on Excited-state Stabilization and Radiative Lifetime. J. Phys. Chem. B. 112, 16300–16306 (2008).

105. Cook, S., Furube, A., Katoh, R., Han, L.: Estimate of singlet diffusion lengths in PCBM films by time-resolved emission studies. Chem. Phys. Lett. 478, 33–36 (2009).

106. Veldman, D., Ipek, O., Meskers, S.C.J., Sweelssen, J., Koetse, M.M., Veenstra, S.C., Kroon, J.M., van Bavel, S.S., Loos, J., Janssen, R. J.: Compositional and electric field dependence of the dissociation of charge transfer excitons in alternating polyfluorene copolymer/fullerene blends. J. Am. Chem. Soc. 130, 7721–7735 (2008).

107. Loi, M.A., Toffanin, S., Muccini, M., Forster, M., Scherf, U., Scharber, M.: Charge Transfer Excitons in Bulk Heterojunctions of a Polyfluorene

Copolymer and a Fullerene Derivative. Adv. Funct. Mater. 17, 2111–2116 (2007).

108. Meng, K., Ding, Q., Wang, S., Gong, Q.: Ultrafast energy transfer in blended polyphenothiazine/polyphenylene vinylene film. Chem. Phys. Lett. 515, 155–158 (2011).

109. Piris, J., Dykstra, T.E., Bakulin, A.A., Loosdrecht, P.H.M. van, Knulst, W., Trinh, M.T., Schins, J.M., Siebbeles, L.D.A.: Photogeneration and Ultrafast Dynamics of Excitons and Charges in P3HT/PCBM Blends. J. Phys. Chem. C. 113, 14500–14506 (2009).

110. Xie, Y., Li, Y., Xiao, L., Qiao, Q., Dhakal, R., Zhang, Z., Gong, Q., Galipeau, D., Yan, X.: Femtosecond Time-Resolved Fluorescence Study of P3HT/PCBM Blend Films. J. Phys. Chem. C. 114, 14590–14600 (2010).

111. Hwang, I.-W., Soci, C., Moses, D., Zhu, Z., Waller, D., Gaudiana, R., Brabec, C.J., Heeger, A.J.: Ultrafast Electron Transfer and Decay Dynamics in a Small Band Gap Bulk Heterojunction Material. Adv. Mater. 19, 2307–2312 (2007).

112. Hwang, I.-W., Moses, D., Heeger, A.J.: Photoinduced Carrier Generation in P3HT/PCBM Bulk Heterojunction Materials. J. Phys. Chem. C. 112, 4350–4354 (2008).

113. Tong, M., Coates, N.E., Moses, D., Heeger, A.J., Beaupré, S., Leclerc, M.: Charge carrier photogeneration and decay dynamics in the poly(2,7-carbazole) copolymer PCDTBT and in bulk heterojunction composites with $PC_{70}BM$. Phys. Rev. B. 81, 125210 (2010).

114. Grancini, G., Polli, D., Fazzi, D., Cabanillas-Gonzalez, J., Cerullo, G., Lanzani, G.: Transient Absorption Imaging of P3HT:PCBM Photovoltaic Blend: Evidence For Interfacial Charge Transfer State. J. Phys. Chem. Lett. 2, 1099–1105 (2011).

115. Devižis, A., Serbenta, A., Hertel, D., Gulbinas, V.: Exciton and Polaron Contributions to Photocurrent in MeLPPP on a Picosecond Time Scale. Mol. Cryst. Liq. Cryst. 496, 16–24 (2008).

116. Deibel, C., Strobel, T., Dyakonov, V.: Origin of the Efficient Polaron-Pair Dissociation in Polymer-Fullerene Blends. Phys. Rev. Lett. 103, 36402 (2009).

117. Vaynzof, Y., Bakulin, A. A., Gélinas, S., Friend, R.H.: Direct Observation of Photoinduced Bound Charge-Pair States at an Organic-Inorganic Semiconductor Interface. Phys. Rev. Lett. 108, 246605 (2012).

118. Fitzner, R., Elschner, C., Weil, M., Uhrich, C., Körner, C., Riede, M., Leo, K., Pfeiffer, M., Reinold, E., Mena-Osteritz, E., Bäuerle, P.: Interrelation between Crystal Packing and Small-Molecule Organic Solar Cell Performance. Adv. Mater. 24, 675–680 (2012).

119. Fitzner, R., Reinold, E., Mishra, A., Mena-Osteritz, E., Ziehlke, H., Körner, C., Leo, K., Riede, M., Weil, M., Tsaryova, O., Weiß, A., Uhrich, C., Pfeiffer, M., Bäuerle, P.: Dicyanovinyl–Substituted Oligothiophenes: Structure-Property Relationships and Application in Vacuum-Processed Small Molecule Organic Solar Cells. Adv. Funct. Mater. 21, 897–910 (2011).

120. Chen, G., Sasabe, H., Wang, Z., Wang, X.-F., Hong, Z., Yang, Y., Kido, J.: Co-Evaporated Bulk Heterojunction Solar Cells with >6.0% Efficiency. Adv. Mater. 24, 2768–2773 (2012).

121. Jespersen, K.G., Zhang, F., Gadisa, A., Sundström, V., Yartsev, A., Inganäs, O.: Charge formation and transport in bulk-heterojunction solar cells based on alternating polyfluorene copolymers blended with fullerenes. Org. Electron. 7, 235–242 (2006).

122. Andersson, L.M., Zhang, F., Inganäs, O.: Stoichiometry, mobility, and performance in bulk heterojunction solar cells. Appl. Phys. Lett. 91, 71108 (2007).

123. Mihailetchi, V.D., van Duren, J.K.J., Blom, P.W.M., Hummelen, J.C., Janssen, R.A.J., Kroon, J.M., Rispens, M.T., Verhees, W.J.H., Wienk, M.M.: Electron Transport in a Methanofullerene. Adv. Funct. Mater. 13, 43–46 (2003).

124. Mihailetchi, V., Koster, L., Hummelen, J., Blom, P.: Photocurrent Generation in Polymer-Fullerene Bulk Heterojunctions. Phys. Rev. Lett. 93, 216601 (2004).

125. De Haas, M.P., Warman, J.M., Anthopoulos, T.D., de Leeuw, D.M.: The Mobility and Decay Kinetics of Charge Carriers in Pulse-Ionized Microcrystalline PCBM Powder. Adv. Funct. Mater. 16, 2274–2280 (2006).

126. Kronenberg, N.M., Deppisch, M., Wurthner, F., Lademann, H.W.A., Deing, K., Meerholz, K.: Bulk heterojunction organic solar cells based on merocyanine colorants. Chem. Commun. 6489–6491 (2008).

127. Ojala, A., Petersen, A., Fuchs, A., Lovrincic, R., Pölking, C., Trollmann, J., Hwang, J., Lennartz, C., Reichelt, H., Höffken, H.W., Pucci, A., Erk, P., Kirchartz, T., Würthner, F.: Merocyanine/C60 Planar Heterojunction

Solar Cells: Effect of Dye Orientation on Exciton Dissociation and Solar Cell Performance. Adv. Funct. Mater. 22, 86–96 (2012).

128. Würthner, F., Archetti, G., Schmidt, R., Kuball, H. G.: Solvent Effect on Color, Band Shape, and Charge-Density Distribution for Merocyanine Dyes Close to the Cyanine Limit. Angew. Chemie Int. Ed. 47, 4529–4532 (2008).

129. Spano, F.: Modeling Disorder in Polymer Aggregates: The 773 Optical Spectroscopy of Regioregular Poly(3-hexylthiophene) Thin 774 Films. J. Chem. Phys. 122, 1−15 (2005).

130. Pope M., S.C.E.: Electronic Processes in Organic Crystals and Polymers. Oxford University Press: New York (1999).

131. Weiser G, B.J.: Polariton induced transparency at low light level: polymer chains dispersed in a monomer single crystal. Phys Rev Lett. 99, 1–5 (2007).

132. Gulbinas V., Chachisvilis M., Valkunas L., S. V.: Excited State Dynamics of Phthalocyanine Films. J. Phys. Chem. 100, 2213−2219 (1996).

133. Morana, M., Azimi, H., Dennler, G., Egelhaaf, H.-J., Scharber, M., Forberich, K., Hauch, J., Gaudiana, R., Waller, D., Zhu, Z., Hingerl, K., van Bavel, S.S., Loos, J., Brabec, C.J.: Nanomorphology and Charge Generation in Bulk Heterojunctions Based on Low-Bandgap Dithiophene Polymers with Different Bridging Atoms. Adv. Funct. Mater. 20, 1180–1188 (2010).

134. Cook, S., Ohkita, H., Kim, Y., Benson-Smith, J.J., Bradley, D.D.C., Durrant, J.R.: A photophysical study of PCBM thin films. Chem. Phys. Lett. 445, 276–280 (2007).

135. Peckus D., Devižis A., Hertel D., Meerholz K., Gulbinas V.,: Charge Carrier Generation in Merocianine:fullerene Blends Investigated by the Fluorescence Quenching and Ultrafast Time Resolved Photocurrent. To be Publ.

136. Yang, X., van Duren, J.K.J., Janssen, R.A.J., Michels, M.A.J., Loos, J.: Morphology and Thermal Stability of the Active Layer in Poly(p-phenylenevinylene)/Methanofullerene Plastic Photovoltaic Devices. Macromolecules. 37, 2151–2158 (2004).

137. Lee, J.K., Ma, W.L., Brabec, C.J., Yuen, J., Moon, J.S., Kim, J.Y., Lee, K., Bazan, G.C., Heeger, A.J.: Processing additives for improved

efficiency from bulk heterojunction solar cells. J. Am. Chem. Soc. 130, 3619–23 (2008).

138. Kim, Y., Choulis, S.A., Nelson, J., Bradley, D.D.C., Cook, S., Durrant, J.R.: Device annealing effect in organic solar cells with blends of regioregular poly(3-hexylthiophene) and soluble fullerene. Appl. Phys. Lett. 86, 63502 (2005).

139. Guo, J., Ohkita, H., Benten, H., Ito, S.: Charge Generation and Recombination Dynamics in Poly (3-hexylthiophene)/ Fullerene Blend Films with Different Regioregularities and Morphologies. J. Am.Chem. Soc. 132, 6154–6164 (2010).

140. Guldi DM, P.M.: Excited-state properties of C(60) fullerene derivatives. Acc Chem Res. 33, 695–703 (2000).

141. Hallermann, M., Kriegel, I., Da Como, E., Berger, J.M., von Hauff, E., Feldmann, J.: Charge Transfer Excitons in Polymer/Fullerene Blends: The Role of Morphology and Polymer Chain Conformation. Adv. Funct. Mater. 19, 3662–3668 (2009).

142. Vandewal, K., Tvingstedt, K., Gadisa, A., Inganäs, O., Manca, J. V: On the origin of the open-circuit voltage of polymer-fullerene solar cells. Nat. Mater. 8, 904–909 (2009).

143. Peckus, D., Devižis, A., Graf, S., Hertel, D., Meerholz, K., Gulbinas, V.: Charge Transfer States in Merocyanine Neat Films and Its Blends. J. Phys. Chem. C. 117, 6039–6048 (2013).

144. Devizis, A., Serbenta, A., Peckus, D., Thiessen, A., Alle, R., Meerholz, K., Hertel, D., Gulbinas, V.: Electric field assisted charge carrier photogeneration in poly(spirobifluorene-co-benzothiadiazole). J. Chem. Phys. 133, 164904 (2010).

145. Deussen, M., Scheidler, M., Bässler, H.: Electric field-induced photoluminescence quenching in thin-film light-emitting diodes based on poly(phenyl-p-phenylene vinylene). Synth. Met. 73, 123–129 (1995).

146. Kern, J., Schwab, S., Deibel, C., Dyakonov, V.: Binding energy of singlet excitons and charge transfer complexes in MDMO-PPV:PCBM solar cells. Phys. status solidi - Rapid Res. Lett. 5, 364–366 (2011).

147. Savenije, T., Kroeze, J., Wienk, M., Kroon, J., Warman, J.: Mobility and decay kinetics of charge carriers in photoexcited PCBM/PPV blends. Phys. Rev. B. 69, 155205 (2004).

148. Cabanillas-Gonzalez, J., Virgili, T., Gambetta, a., Lanzani, G., Anthopoulos, T., de Leeuw, D.: Subpicosecond photoinduced Stark spectroscopy in fullerene-based devices. Phys. Rev. B. 75, 045207 (2007).

149. Mackenzie, R.C.I., Frost, J.M., Nelson, J.: A numerical study of mobility in thin films of fullerene derivatives. J. Chem. Phys. 132, 064904 (2010).

150. Clarke, T.M., Ballantyne, A.M., Nelson, J., Bradley, D.D.C., Durrant, J.R.: Free Energy Control of Charge Photogeneration in Polythiophene/Fullerene Solar Cells: The Influence of Thermal Annealing on P3HT/PCBM Blends. Adv. Funct. Mater. 18, 4029–4035 (2008).

151. Grancini, G., Maiuri, M., Fazzi, D., Petrozza, a, Egelhaaf, H.-J., Brida, D., Cerullo, G., Lanzani, G.: Hot exciton dissociation in polymer solar cells. Nat. Mater. 12, 29–33 (2012).

152. Zhu, X., Yang, Q., Muntwiler, M., Charge-, F.: Charge-Transfer Excitons at Organic. Acc. Chem. Res. 42, 1779–1787 (2009).

153. Jailaubekov, A.E., Willard, A.P., Tritsch, J.R., Chan, W.-L., Sai, N., Gearba, R., Kaake, L.G., Williams, K.J., Leung, K., Rossky, P.J., Zhu, X.-Y.: Hot charge-transfer excitons set the time limit for charge separation at donor/acceptor interfaces in organic photovoltaics. Nat. Mater. 12, 66–73 (2013).

154. Vithanage, D.A., Devižis, A., Abramavičius, V., Infahsaeng, Y., Abramavičius, D., MacKenzie, R.C.I., Keivanidis, P.E., Yartsev, A., Hertel, D., Nelson, J., Sundström, V., Gulbinas, V.: Visualizing charge separation in bulk heterojunction organic solar cells. Nat Commun. 4, (2013).

155. Gregg, B.A.: Entropy of Charge Separation in Organic Photovoltaic Cells: The Benefit of Higher Dimensionality. J. Phys. Chem. Lett. 2, 3013–3015 (2011).